11-13-2014

A LOW-POWER COMPACT NUCLEAR QUADRUPOLE RESONANCE (NQR) BASED EXPLOSIVE DETECTION SYSTEM

Xinwang Zhang
University of Nebraska-Lincoln, xzhang2@huskers.unl.edu

A LOW-POWER COMPACT NUCLEAR QUADRUPOLE RESONANCE (NQR) BASED EXPLOSIVE DETECTION SYSTEM

by

Xinwang Zhang

A DISSERTATION

Presented to the Faculty of

The Graduate College at the University of Nebraska

In Partial Fulfilment of Requirements

For the Degree of Doctor of Philosophy

Major: Electrical Engineering

Under the Supervision of Professor Sina Balkır

Lincoln, Nebraska

September, 2014

A LOW-POWER COMPACT NUCLEAR QUADRUPOLE RESONANCE (NQR) BASED EXPLOSIVE DETECTION SYSTEM

Xinwang Zhang, Ph.D.

University of Nebraska, 2014

Adviser: Sina Balkır

Abandoned landmines and terrorist bomb attacks are severe issues threatening our society. These issues necessitate the development of prompt and accurate explosive detection systems. The detection mechanisms commonly-used nowadays usually search for explosive containers, which suffer numerous false alarms caused by external detection circumstance changes. Alternatively, explosive substances inside the bombs and landmines can be detected by means of biology, chemistry and physics techniques. Nuclear Quadrupole Resonance (NQR) detection technology has proven to be a highly effective solution for detecting explosives unambiguously.

In this work, a portable NQR-based explosive detection system that employs state-of-the-art semiconductor technologies is presented. This system consists of a transmitter section, an NQR probe, an RFI probe, a receiver section and auxiliary modules. In the transmitter section, a novel Class-D power amplifier (PA) with fast-start fast-stop functions is proposed. The receiver section consists of low-noise amplifiers (LNAs), an adaptive filter for RFI mitigation, and an advanced DSP platform for NQR signal processing. The LNA is based on an infinite input impedance power matching scheme, which improves the noise factor and simplifies the circuit structure. A Continuous Time Least Mean Square (CTLMS) adaptive filter is employed to mitigate RFI in the analog domain, and a new weight-updating circuit with DC offset cancellation is included in this adaptive filter. Between the transmitter and the receiver sections, a power multiplexing scheme is designed in order to use a single NQR

probe for both transmitting and receiving. A PIN diode based RF switch provides high isolation during transmitting and low signal attenuation during receiving.

A customized mixed-signal integrated circuit (IC) is fabricated in 0.18 μm RF CMOS process, which contains the LNAs, adaptive filter and micro controller unit (MCU). The MCU performs the logic control of the whole system. The proposed NQR-based explosive detection system is implemented at board level with the prototype system successfully established. Detection of chemical samples, hexamethylenetetramine (HMT) and Urea, are performed on the prototype system. Test results show the effectiveness of the proposed solution as well as the compact size and low power consumption of the system.

ACKNOWLEDGMENTS

This dissertation could not have been achieved without the help from many people throughout my academic life in Lincoln. First of all, I want to express my deepest appreciation to my advisor, Professor Sina Balkır. He has been providing invaluable guidance and full support during the whole process of my research. I have learned many things from him including technical knowledge, research methodologies, and communication skills. I truly appreciate his patience, wisdom, encouragement and understanding which help me to get through many difficult times during my research. I could not have achieved any of the accomplishments without his support.

I would like to thank Professor Michael W. Hoffman for his help on signal processing related topics, especially the guidance on the adaptive filter design. He has introduced an entirely new technology area to me. I would like to thank Professor Gerard Harbison for being the invaluable resource of chemistry and physics knowledge, laboratory equipment and experimental materials. The final experiment could not have been done without his support on the chemical samples. I also would like to thank Professor Wei Qiao for the guidance on power electronics topics. Moreover, I truly appreciate these professors for serving on my supervisory committee.

I want to thank my peer graduate students and friends in Lincoln, Nathan Schemm, Bin Du, Baohua Dong and many others. The discussions with them have always been great innovation sources for me. More importantly, their friendship helps me overcome many difficulties, and makes my life much more colorful.

I would like to thank my parents Ping Zhang and Mingyuan Song, for their unconditional love and support. Finally, I am indebted to my wife Youlu and my son Shi. They are my best friends and my source of strength, which makes me keep moving forward. This dissertation is dedicated to them.

Contents

List of Figures

List of Tables

Chapter 1

Introduction

The society is currently confronting two main severe safety issues which concern explosives. One issue is the global abandoned landmines. According to the United Nations' estimate, approximately 80 million anti-personnel landmines are still in place, mostly in after-war fields. 85 countries throughout Africa, Southeast Asia, the Middle East and South America are facing the threat from uncleared landmines and unexploded ordnance. Although there is no accurate number of people who were injured and killed by landmines, it is believed that in each year, there are approximately 15000 to 20000 new nonmilitary casualties, one third of which are children, according to the estimation provided by [1]. The other issue is the terrorist bomb attacks. It is one of the most destructive terrorism actions that pose a cruel threat to civilians. Although the victims of terrorist actions may be much less compared to those of the landmine issue, it causes worse impacts and more severe panicking atmosphere to the society.

The above issues necessitate the development of prompt and accurate explosive detection systems. In both cases, the landmines and bombs have a big variety in terms of conformation, packaging and triggering setup. In the earlier times, metal was often used to package landmines and bombs. Thus, traditional explosive detectors are mostly metal sensors. However,

landmines with plastic cases became more popular in the past few decades as metal-sensor based detectors cannot locate them. Compared to landmines, terrorist bombs use even more diverse packaging materials and constructing forms. They are usually homemade and can be easily concealed under other ordinary objects [2]. Hence, the traditional explosive detectors based on metal sensors are prone to inaccuracies and errors.

No matter what types of packaging materials are used, explosive materials are indispensable for making landmines and bombs. Therefore, disclosing the explosive substances themselves, instead of the packaging material, could be more reliable and accurate across various circumstances. To that end, a mechanism to detect the explosive itself should be employed, which involves the most advanced physics and chemistry technologies for explosive detection. Furthermore, considering that most of the explosive detection tasks are field applications, a portable detector is highly desired. With the recent advances of semiconductor technologies, an integrated, low-power and compact-sized explosive detector becomes viable. The state-of-the-art analog/mixed-signal circuit design and system-on-chip (SoC) technology can be taken advantage of to realize this portable explosive detection solution.

1.1 Review of Existing Explosive Detection Systems

During the past several decades, a wealth of effort has been dedicated by the researchers to find the solutions for explosive detectors [4]. Depending on the detecting mechanisms, detectors can be divided into two categories. The first type of detectors, referred to as ambiguous detectors, usually are applied to search for the bombs with indirect means, such as detecting the bomb containers, or sensing the environmental changes caused by the existence of the bombs. The second type of detectors, named unambiguous detectors, are able to sense the explosive materials inside the bombs by means of biology, chemistry, and physics technologies. In the second category, the detectors can be further categorized into trace

or bulk detectors, based on the volume of the explosive sample. Trace explosive detectors sample the explosive molecules volatilized from the bombs and recognize them with variant technologies, while bulk detectors usually detect the bomb as a whole object. In the following subsections, a brief synopsis of different detectors is given for each category.

1.1.1 Ambiguous Bomb and Landmine Detectors

Not surprisingly, methods of detecting bombs and landmines were initiated with sensors that detect the containers, especially the metal ones, as this type of detector has simple configurations and accessible background theories. Over years of development, these detection solutions have been improved in many ways including portability, sensitivity and cost. As of today, they are still the most prevalent systems used by military and security departments.

Metal-detection based demining systems are the first type of detectors for locating mines. With more and more anti-personnel mines tending to use plastic packages, metal detectors no longer work for them. Alternatively, ground penetrating radars can detect and image the buried objects, by detecting the density inconsistency under the ground. But they are vulnerable to complicated environments and suffer from a mass of false alarms, as they may also find buries objects other than landmines.

X-ray scanners are another popular detector of this type. They are widely used in airports, train stations, building entrances and other security applications. As it can "see" through concealing covers and locate suspicious objects, the detection coverage of X-ray scanners is quite superior. However, X-ray detectors cannot not be used for field applications in a large area, such as demining. Moreover, the detection automation of X-ray scanners is difficult, as there are no straightforward criteria to determine what types of object appearances are questionable. Trained human operators are always required to make accurate decisions.

1.1.2 Trace Explosive Detection Systems

Trace explosive detection generally refers to the methods that sense the explosive molecules volatilized from the bombs, and process the odor signals to identify and locate the bombs [23]. The most well-known detection method in this category is to employ sniffing canines. As of today, detecting explosives by trained dogs is still the most reliable method. But the cost for training and maintaining sniffing dogs is very high. As an alternative, also inspired by dogs, people started to develop vapor sensing based detectors that mimic dog sniffing.

Ion-mobility spectrometry (IMS), as one of the alternative methods to sniffing canines, has been employed for military and security purposes. It can isolate and identify vaporized explosive molecules by checking the mobility of these molecules in a carrier buffer gas [5, 6]. Mass spectrometry (MS) is a similar means to IMS. The detection is based on identifying the mass of explosive molecules. However, these two types of detectors have bulky sizes and comparatively low sensitivity [7].

Another actively emerging research trend for vapor sensing detectors is to utilize the reactions of some materials to the explosive molecules. The test materials often have high bonding ability to the explosive molecules being searched. Essentially, with the presence of certain explosive molecules, some characteristics of the test materials will be changed. The setups for this type of detectors are similar. The sample air gathered from the detecting area is directed into a chamber that has the test material inside. If explosive molecules are contained in the sample air, and the concentration of explosive molecules is above the detection threshold of the test material, changes of certain characteristics on the test material can be captured and amplified in terms of electrical signals. Some of the reported detection systems are briefly summarized as follows.

- Surface Acoustic Wave (SAW) filter based vapor sensors. The resonant frequency of the SAW filter changes with presence of certain explosive molecules [8, 9, 10].

- Conductive polymer. It has the variable conductivity that changes with the explosive molecules captured by the polymer [11, 12, 13, 14].
- Organic FET (OFET). Similar to the conductive polymer, the OFET's electronic characteristic changes with the presence of specific explosive molecules [15, 16, 17]
- Fluorescence dye or polymer. The detection is based on the change of the fluorescence light with the presence of specific explosive molecules [19, 20, 21, 22].

For the first three detectors, electrical characteristic changes of the test material can be converted into electrical signals directly. For fluorescence materials, the light changes, either in color or in intensity, need to be sensed and captured by an image sensor or a camera system. Then, specifically designed circuits can be employed to process the electrical signals from the image sensor. Compared to IMS and MS, this type of detection systems can be realized in compact sizes with high sensitivity.

Unlike metal detectors and ground penetrating radars, the vapor detection system is an unambiguous detection technique that is searching for explosives inside the bombs. Therefore, low false alarm rate is a promising feature of this type of systems [3]. However, the vapor sensing detectors have difficulties in finding bombs with tightly sealed packages that have very few escaping explosive molecules. As a result, detection coverage may be limited.

1.1.3 Bulk Unambiguous Explosive Detectors

The word "bulk" is used to distinguish this type of detectors from trace explosive detectors. "Bulk" here does not mean "a bigger volume" of the bombs. It indicates this type of detectors detect the bombs or linemines as whole objects, instead of catching traces of explosive molecules. When the bombs are well sealed, bulk detectors are proven to be particularly useful compared to trace detectors.

In the past several decades, nuclear resonance technologies have been developed towards bulk explosive detection applications. Nuclear magnetic resonance (NMR) and nuclear quadrupole resonance (NQR) based detectors are two main trends that the researches are focused on. NMR (also well known by one of its applications, Magnetic Resonance Imaging – MRI [24]) is a radio frequency (RF) technique that is able to locate explosives by sensing the excited resonance signals from a certain type of nuclei inside explosive materials. Due to the fact that NMR needs a large DC magnetic field to enhance the feedback signal level, it is infeasible to be applied for field detection. Most of the NMR based explosive detection systems are developed for luggage screening. NQR, on the other hand, does not require the presence of the DC magnetic field. As a variant technique of NMR, NQR detection only works for the nuclei with a spin number $I > \frac{1}{2}$. In another word, the nuclei need to have quadrupole moments. Coincidentally, most of the explosive substances such as Trinitrotoluene (TNT), Cyclotrimethylenetrinitramine (RDX), Hexamethylene triperoxide diamine (HMTD), etc., are typically rich in ^{14}N (nitrogen) nuclei with a spin quantum number $I = 1$. Therefore, NQR is highly amenable to explosive detection.

NQR is highly sensitive to the distributions of electrons and other nuclei around the nucleus. This characteristic makes NQR an attractive option for realizing the unambiguous explosive detectors. The NQR detection starts with transmitting a high-power RF signal through a customized NQR antenna to stimulate ^{14}N nuclei in the explosive molecules from the equilibrium state to the excited state that has a higher energy level. Then, the detection is achieved by observing the quantum transitions between nuclear quadrupole energy levels of these nitrogen nuclei in the form of a returning RF signal, which may be picked up by either the same antenna or another antenna dedicated to receiving. The frequency of the NQR signals strongly depends on the molecule structure which contains ^{14}N. Hence, the NQR spectra are unique for a given chemical compound and are insusceptible to the interference of other nitrogen containing materials during the NQR measurement [25].

The main disadvantage of NQR, however, is that the returning signals are inherently weak and susceptible to radio frequency interference (RFI) [26]. Typically, the returning NQR signal level is very low and even comparable to the thermal noise level of the probe. To address the weak signal problem, most NQR explosive detection systems actually perform the detection by repeating the detection cycles many times. The NQR feedback signal collected in each detection cycle is called a segment. The segments are averaged to increase the signal-to-noise ratio (SNR). On the other hand, RFI may severely corrupt the detection performance. For general explosives, the NQR signal frequency is in the range of 500 kHz to 6 MHz, which overlaps the frequency band of AM radio. If no precautions are taken, the relatively strong RFI from AM radio stations can lead to a low signal-to-interference ratio (SIR) and poor detection performance. To address this problem, NQR explosive detection systems are often equipped with RFI mitigation circuits.

In short, except NQR, aforementioned explosive detection schemes all have some drawbacks to prevent them from realizing an online, standalone and portable explosive detection system that is capable of detecting general bombs and landmines in field applications [27, 28]. On the contrary, NQR has many advantages over other detection schemes, including the good remote sensing ability in a short range, low false alarm rate, bulk explosive detection independent of surrounding environments. Its advantages also outweigh its own drawbacks, as the impact of the drawbacks can be mitigated with the help from advanced signal processing and circuit design technologies today.

1.2 Review of Related Work for NQR Based Explosive Detection Systems

In the middle 1950s, the first experiment successfully showing the NQR phenomenon was performed by Dehmelt and Kruger [29]. At that time, people did not realize the possibility of applying NQR towards explosive detection. In 1960s, several academic research groups started working on developing NQR devices for explosive detection. But NMR was still the mainstream of the research, as it has much better signal-to-noise ratio that leads to higher detection accuracy and simpler electronic circuit configuration [31]. This situation did not change until 1970s. Since then, many remarkable research milestones have been achieved. In this section, the related work for NQR explosive detection is briefly reviewed based on two main aspects of the detection systems – hardware configuration and NQR signal processing techniques.

1.2.1 Hardware Configuration

Same with most of detection systems, NQR detection systems mainly contain two sections: the transmitting section (TX) and receiving section (RX). Given the requirements of NQR detection, on the TX side, high output power level is demanded. On the RX side, high resolution for the low level RF feedback signal is desired. In addition, the NQR probe, also called the NQR antenna, is a delicate portion of the system that needs to be well designed to have high sensitivity to the signal and reasonable rejection to RFI.

J. A. S. Smith [25], from King's College in England, started his research on NQR based explosive detection systems by the time of around 1970. He made many major contributions to this area, including the fundamental research of NQR Spectroscopy theory and development of explosive detector systems. Based on the NQR signal measurement results of

RDX reported by Landers et al. in 1981 [32], Smith proposed an NQR detection system solution for RDX and high melting explosive (HMX) related explosive devices [33, 34, 35], which became a standard reference system for many later improvements. A demonstration system was built up with the proposed solution. In this system, TX consists of an RF power amplifier, an RF signal source, an RF gate and a pulse pattern generation circuit. RX has a pre-amplifier and a phase-sensitive detector. For the NQR probe, a power matching network, a tuning circuit and a power duplexer are equipped. The whole system is controlled and coordinated by a master computer. Meanwhile, the collected signals are also processed by the master computer. V. S. Grechishkin presented a baggage scanner based on NQR signal detection of RDX explosives in [36]. The structure of the scanner is very similar to the demonstrator system that Smith proposed. But two sets of RF probes, one for transmitting and one for receiving, are employed. Later on, an improved NQR baggage scanning system is presented by Rudakov in [37]. In the above detection systems, to mitigate the RFI impact, the NQR probe has to be shielded, which makes it infeasible for field applications.

A group of researchers from Naval Research Laboratory and Quantum Magnetics Inc., including A. N. Garroway, J. B. Miller, B. H. Suits, et al., have been working on the development of NQR landmines and bombs detection systems for field applications [44, 38, 39, 43]. They were mostly focused on the engineering part of improving the detection performance and robustness under variant and complicated conditions. In their work, they addressed many system design challenges and proposed novel functional modules and approaches [38], including: 1) noise-immune coil for mitigating RFI impact [39, 40, 41, 42], 2) secondary RFI collecting probe for adaptively mitigating RFI impact [43], 3) Q-damping circuit for instantly detecting NQR signals right after the excitation period [44, 45], 4) excitation signal pulse sequence optimization [46].

J. L. Schiano et al. [47] proposed a feedback control scheme to improve the detection performance. With a common NQR detection system, a feedback loop is added to automat-

ically adjust the control parameters for generating multiple excitation pulse sequences, by finding a specific set of parameters that result in the best detection performance under a given test environment [48].

As NQR gains more and more attention for explosive detection, more researchers devote their effort in this area. R. M. Deas et al. [49] proposed an NQR system designated for short range explosive detection. In this work, they proposed a technique for the NQR probe design to improve the RFI rejection capability. H. Itozaki et al. are a research group in Japan. Their work was mainly focused on automatic NQR landmines detection systems [50, 51]. They employ high-TC RF superconducting quantum interference devices (SQUID) to fulfill NQR detection.

In addition to hardware design, some chemistry researchers, such as Ota [53] and Rudakov [54], were focused on developing excitation signal patterns to improve the detection performance for some new emerging explosives, such as Hexamethylenetetramine (HMT) and HMTD.

All of the above accomplishments were initiated from the laboratory's perspective. These NQR detection systems, which exist in the forms of stationary demonstrator systems or large security scanning systems, either consume high power to achieve high accuracy, or have bulky-sized electrical sections and data processing platforms. As a result, they are not suitable for field applications, especially for being used portably.

1.2.2 NQR Signal Post-Processing Techniques

Some researchers who specialize in signal processing have been investigating the algorithms for NQR signal post-processing in order to enhance the detection performance from the software side. Basically, the challenge for NQR signal detection is to reduce the impact from RFI and to differentiate the weak NQR signal from background noise. Therefore, the

algorithms need to cope with these problems.

Y. Tan, S. L. Tantum, et al. [55], a research group from Duke University, proposed to use a digital domain least-mean-square (LMS) adaptive filter to mitigate the background RFI. In this approach, a secondary antenna is needed to collect the RFI signal that correlates with the RFI signal picked up by the main NQR probe. Then, the LMS filter finds the correlation between the two RFI signals and subtract it from the main NQR probe signals. The NQR signals after LMS filtering are processed by a Baysian detector. Following that, they proposed other algorithms for processing post-mitigation NQR signals to improve the detection performance. In [56], an average power detector based on a power spectral estimation algorithm is presented. In [57], Kalman filtering technique is applied to NQR signal detection. They also developed a Cramer-Rao Lower Bound detection approach based on the investigation of the statistical model of non-Gaussian RFI [58]. Nevertheless, using the LMS algorithm to suppress RFI with the help of a secondary antenna is a major contribution to the design of NQR detection systems. In addition, G. Liu, Y. Jiang, P. Stoica, J. Li, et al., a group from University of Florida, claimed that RFI signals collected by the main NQR probe and the secondary antenna array (multiple antennas for collecting RFI only) are not only spatially but also temporally correlated. Based on that, they proposed several methods, including alternating least squares (ALS), doubly constrained robust Capon beamformer (DCRCB), for RFI suppression [59, 60, 61]. The advantage of these methods is that both spatial and temporal information of collected RFI signals from the antenna array is utilized.

S. D. Somasundaram, A. Jakobsson, et al. are an active research group that have done extensive research work in this area. They presented an NQR signal model in [62], and attempted to fully exploit all the information provided by this model for detection algorithm development. In the traditional detection algorithms, NQR signal segments captured after stimulus pulses in one pulse sequence are averaged to produce one NQR signal segment

with high signal-to-noise ratio (SNR), thus to improve the accuracy of decision. On the contrary, Somasundaram, et al. propose to utilize the captured NQR signal segments as a sequence of detection, instead of averaging them to produce one segment. In this way, the decaying characteristic of each NQR signal segment can be used. In [63, 64, 65], the authors proposed to refine two generalized maximum-likelihood ratio test methods and then enable these methods to work on a serial NQR signal sequence. In [66], this approach is further improved to deal with the NQR signal sequence which has uncertain amplitude. This modification makes significant improvement because uncertain amplitude is a common issue for NQR signals detected in the field. Moreover, they proposed several novel techniques to fulfill RFI suppression. In [67], they presented a method to just use one NQR probe for RFI mitigation. Firstly, signal-of-interest free data are collected before or after the real detection without the presence of the stimulus RF pulse sequence. These data contain only the RFI signals, but not the NQR signals. Then NQR signal data are captured during the real detection cycle, which contain both NQR signals and RFI signals. The RFI signals in these two different data sets have temporal correlation. Therefore, the signal-of-interest free data can be transformed and subtracted from NQR signal data to remove RFI.

From the review of NQR signal processing techniques, we can see that to fulfill these complicated detection algorithms, the detection system must be equipped with a versatile computation platform. This platform needs a fast calculating speed and a massive storage memory to restore and process the NQR signal for one detection.

1.3 Contributions and Dissertation Outline

In view of the aforementioned limitations of current explosive detection systems, a portable NQR-based explosive detection system solution is proposed in this work. As the goal of this solution is to feature a compact size and low power consumption for portable applications

while maintaining high detection performance, some novel circuit configurations for different parts in the detection system are proposed and implemented. These circuitry novelties are the main contributions of this dissertation. They are briefly summarized as follows.

1. A novel class-D type power amplifier circuit is specially designed for NQR and NMR systems. In addition to the high power efficiency inherently brought by class-D power amplifiers, this customized PA design is equipped with fast-start and fast-stop functions that can greatly facilitate NQR and NMR detection performance. Moreover, the pure digital control essence of the class-D PA can significantly simplify the control circuit for generating excitation RF pulse sequences.

2. A new power multiplexing scheme between the transmitting circuit and receiving circuit is proposed to cooperate with the class-D PA for NQR detection. It is designed to use a single NQR probe for both transmitting and receiving. To implement the proposed power multiplexing scheme, a PIN diode based RF switch is adopted to provide high isolation during the transmitting period and low signal attenuation during the receiving period.

3. An integrated low noise amplifier (LNA) based on an infinite input impedance power matching scheme is presented. Employing this infinite input impedance power matching scheme not only results in a lower noise factor for the LNA, but also reduces the number of components that are needed to construct the power matching network for the NQR probe.

4. An analog domain adaptive filter is used to fulfill RFI mitigation. With this RFI mitigation method, the resolution constraints of down-stream signal processing circuits, such as the analog-to-digital converter (ADC) and digital signal processing unit are greatly relieved. Furthermore, in order to improve the RFI mitigation performance

of the adaptive filter, a new weight-updating circuit with DC offset cancellation is presented. This adaptive filter and LNA are integrated with an MCU on a customized mixed-signal integrated circuit (IC). The MCU performs the logic control for the NQR detection system.

5. For the digital signal processing section, a digital signal processor (DSP) based platform is employed. It can substantially reduce the system size and power consumption.

The detailed discussions for the contributions are presented in the rest of the dissertation. Chapter 2 briefly reviews the physical principles of NQR technology for better comprehending the design of the NQR detection system. In Chapter 3, the proposed NQR detection system is introduced from the system design's perspective to show the improvements that have been made. The working principles and novelties of the class-D power amplification scheme are depicted in Chapter 4. Chapter 5 mainly discusses the advantages of the proposed power matching and power multiplexing method. The LNA circuit design is described in Chapter 6. The analog adaptive filtering circuit is presented in Chapter 7. Also, the novel weight-updating circuit design is introduced. Moreover, from Chapter 4 to Chapter 7, test results for each circuit module are presented and concluded in each chapter. The software design for the NQR detection system, including DSP-based NQR signal processing and MCU-based logic control, is presented in Chapter 8. The implementation and evaluation results of the complete NQR detection system are discussed in Chapter 9. Finally, this dissertation is concluded and future work is discussed in Chapter 10.

1.4 Publications

The above work has been published in prestigious and peer-reviewed journals and conference proceedings. The publications are listed below:

[A] Xinwang Zhang, Sina Balkır, Michael W. Hoffman and Nathan Schemm, "A low-power CMOS continuous-time LMS adaptive filter with robust DC-offset cancellation," *Proc. of 53rd IEEE International Midwest Symposium on Circuits and Systems*, pp. 977–980, 2010.

[B] Xinwang Zhang, Sina Balkır, Michael W. Hoffman and Nathan Schemm, "A robust CMOS Receiver front-end for Nuclear Quadrupole Resonance based explosives detection," *Proc. of 53rd IEEE International Midwest Symposium on Circuits and Systems*, pp. 1093–1096, 2010.

[C] Xinwang Zhang, Nathan Schemm and Sina Balkır, "A novel power amplification scheme for nuclear magnetic resonance/nuclear quadrupole resonance systems," *Review of Scientific Instruments*, vol. 82, no. 3, pp. 034707–034707-6, 2011.

[D] Xinwang Zhang, Nathan Schemm, Sina Balkır and Michael W. Hoffman, "A Low-Power Compact NQR Based Explosive Detection System," *IEEE Sensors Journal*, vol. 14, no. 2, pp. 497–507, 2014.

The novel class-D power amplification scheme, described in Chapter 4, is published in [C]. The overall system architecture in Chapter 3, power multiplexing and matching mechanism in Chapter 5, LNA circuit design in Chapter 6 and software configuration in Chapter 8 are published in [D]. Chapter 3 and Chapter 6 are also partially published in [B]. [A] presents the work of the adaptive filter and weight-updating circuits described in Chapter 7.

Chapter 2

NQR Background

To better understand the NQR based explosive detection, a brief review of the NQR background is presented in this chapter. More details about the general NQR technology can be found in [25, 69, 70]. In addition, in order to get a more insightful vision of the NQR system design, NQR signal models proposed in the literature are introduced and discussed.

2.1 NQR Theories

2.1.1 Principles of NMR

To understand the NQR theories more easily, we start with introducing its ancestor – NMR, which was initially demonstrated in 1940's [68], shortly before NQR. The NMR phenomenon can be explained in either the microscopic view or macroscopic view [18].

From the microscopic view, for a nucleus that has a spin number $I \neq 0$, i.e. $I = n/2$, where $n > 0$, and n is an integer, it possesses a magnetic dipole moment. We can imagine that these nuclei are tiny magnetic needles with north and south poles, as shown in Fig. 2.1. In common sense, if a magnetic needle is positioned in an external DC magnetic field with a certain strength, denoted as $\mathbf{B}_o$, the needle will point its north pole along the magnetic

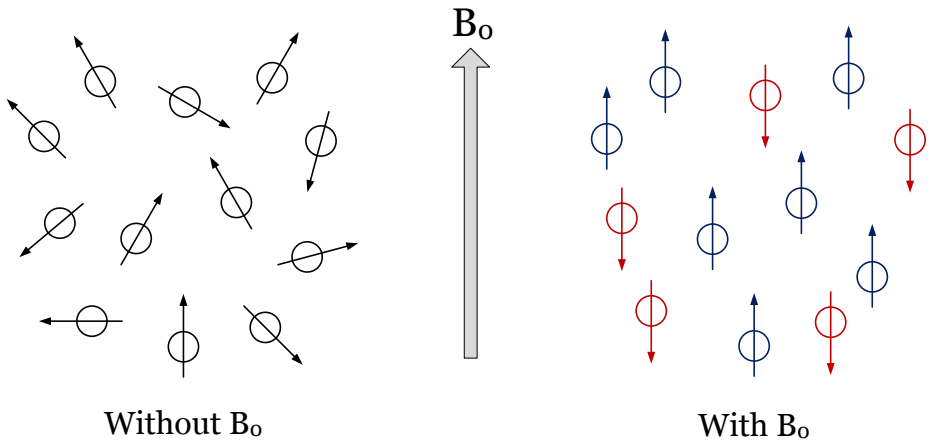

Figure 2.1: Magnetic dipole moments distribution with and without $\mathbf{B}_o$

field direction. The same rule applies to the nuclei. The difference is that with the presence of thermal disturbance, in the microcosmic scale, not all the magnetic dipole moments of the nuclei are oriented along the external magnetic field direction. According to quantum mechanics, the magnetic moments can either be oriented in the same direction of $\mathbf{B}_o$ or oppose the direction of $\mathbf{B}_o$. Therefore, two energy levels are formed. The nuclei whose magnetic moments are against the direction of $\mathbf{B}_o$ have the higher energy level, which is often called the excited state. On the other hand, the nuclei with the magnetic moments in the same direction with $\mathbf{B}_o$ have the lower energy level, which is called the ground state. This phenomenon is called Zeeman interaction. In fact, for nuclei with a spin number $I = n/2$, the resulting number of the energy levels will be $2I + 1$. For the ease of demonstration, we use $I = 1/2$ as an example, which leads to two energy levels. The split states for $I = 1/2$ is shown in Fig. 2.2. The energy difference between these two states are determined by $\mathbf{B}_o$. Higher $\mathbf{B}_o$ makes more nuclei aligned with $\mathbf{B}_o$, and therefore more nuclei reside in the ground state.

In the meantime, if the sample is irradiated by electromagnetic radiation at a certain frequency (the NMR frequency of a certain sample material), and the radiated energy (de-

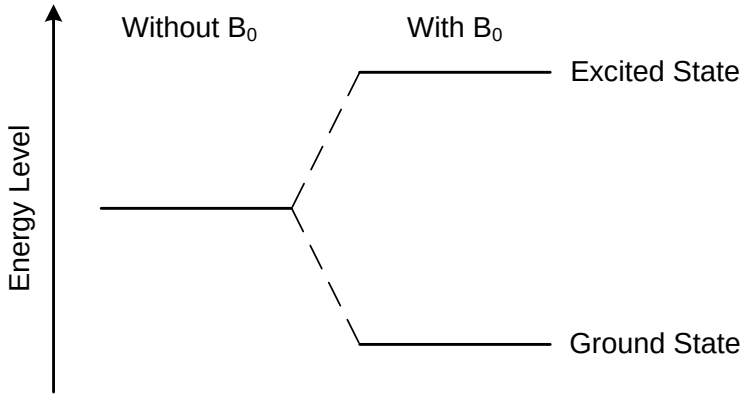

Figure 2.2: Split states for $I = 1/2$ nuclei

termined by the frequency) exactly matches the energy difference between the two states, the nuclear spins in the lower energy state will absorb the energy and transit to the higher energy state. The NMR frequency ν_o is

$$\nu_o = \frac{\gamma B_0}{2\pi} \tag{2.1}$$

where γ is the gyromagnetic ratio of the nuclei.

From the macroscopic view, the NMR phenomenon can be illustrated by Fig. 2.3. The

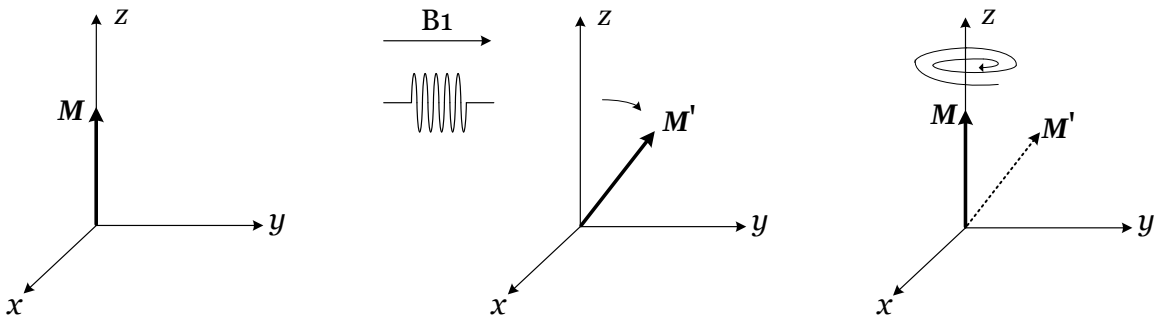

(a) before $\mathbf{B}_1$ applied (b) applying $\mathbf{B}_1$ (c) after $\mathbf{B}_1$ applied

Figure 2.3: The net magnetization changes the rotating direction with the applied radiation

summation of the unevenly distributed magnetic moments leads to the bulk or net magnetization, denoted as $\mathbf{M}$ in Fig. 2.3. If an individual magnetic moment is denoted as μ, $\mathbf{M} = \sum \mu$. In Fig. 2.3, The z axis is chosen as the direction of $\mathbf{B}_o$. With the presence of $\mathbf{B}_o$ and before the radiation applied, $\mathbf{M}$ is a vector along the direction of $\mathbf{B}_o$, as shown in Fig. 2.3 (a). Fig. 2.3 (b) shows the orientation of $\mathbf{M}$ changes when the radiation is applied, whose strength is denoted as $\mathbf{B}_1$. When $\mathbf{B}_1$ is applied, $\mathbf{M}$ will tilt away from its equilibrium position to a non-equilibrium position, with an angle from the z axis. The tilting net magnetization vector is denoted as $\mathbf{M}'$ in Fig. 2.3 (b). After $\mathbf{B}_1$ ceases, the out-of-equilibrium magnetization vector $\mathbf{M}'$ precesses about $\mathbf{B}_o$ at the NMR frequency and relaxes back to the equilibrium position, which is shown in Fig. 2.3 (c). This process is called "relaxation", which induces an RF signal oscillating at the NMR frequency. The RF signal can be picked up by a nearby coil. Actually, this RF signal is the NMR detection signal for the sample under test.

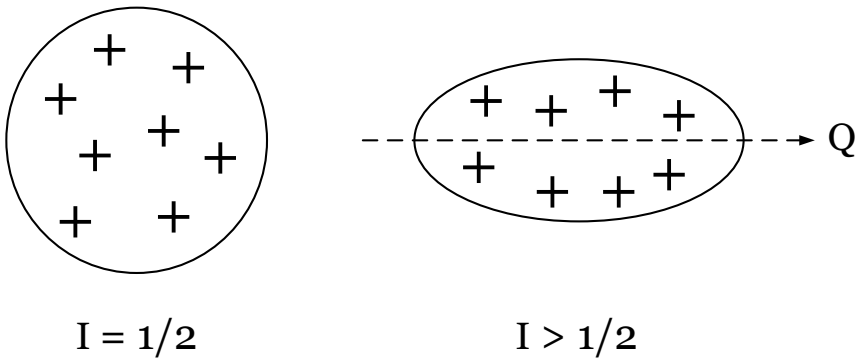

Figure 2.4: The charge distribution of nuclei with $I = 1/2$ and $I > 1/2$

2.1.2 Principles of NQR

The NQR working principles are similar to those of NMR. The difference is that NMR utilizes the interaction between the nuclear magnetic moment and the external magnetic field, whereas NQR exploits the interaction between the electric quadrupole moment of the nucleus and the electric field gradient (EFG) that surrounds the nucleus. For $I > 1/2$ type of nuclei, the charge distribution is non-spherical, whose shape is similar to a squash, as illustrated in Fig. 2.4. Therefore, this type of nucleus has an electric quadrupole moment, usually denoted as $\mathbf{Q}$. Meanwhile, inside the molecule where a $I > 1/2$ nucleus resides, if the charge distribution surrounding the nucleus is asymmetric, an EFG will be produced. Just as the nuclear spins tending to align with $\mathbf{B}_o$ in NMR, $\mathbf{Q}$ will try to align with EFG, as shown in Fig. 2.5. This indicates an important difference between NQR and NMR — NQR does not require the presence of an external DC magnetic field $\mathbf{B}_o$.

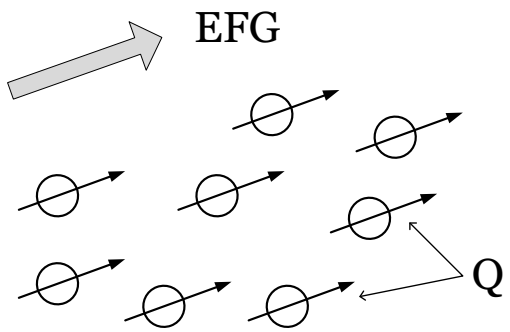

Figure 2.5: EFG interacts with electric quadrupole moments of $I > 1/2$ nuclei

Similar to Zeeman interaction, energy states of the nuclei will be split by EFG. Since the purpose of studying NQR in this dissertation is for explosive detection, only ^{14}N with $I = 1$ is interested. For $I = 1$, there are three energy states allowed. They are States -1, 0 and $+1$, respectively. State 0 is the ground state. State -1 and $+1$ are the excited states. As

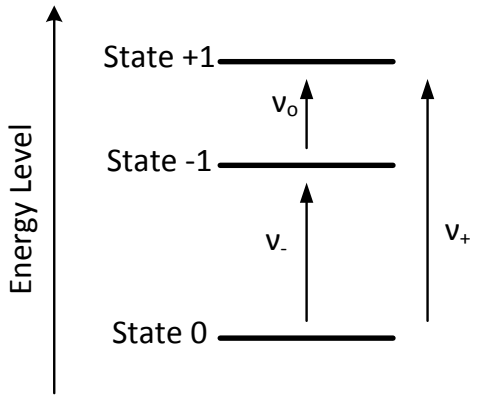

Figure 2.6: Illustration of states and possible transitions for ^{14}N, $I = 1$.

illustrated in Fig. 2.6, three possible transitions between the energy states can be observed, which correspond to three NQR resonant frequencies. These three frequencies are denoted as ν_o, ν_- and ν_+, respectively, and can be derived by

$$\begin{aligned} \nu_o &= \frac{1}{2}\frac{e^2qQ}{h}\eta \\ \nu_- &= \frac{3}{4}\frac{e^2qQ}{h}(1-\frac{\eta}{3}) \\ \nu_+ &= \frac{3}{4}\frac{e^2qQ}{h}(1+\frac{\eta}{3}) \end{aligned} \tag{2.2}$$

where e^2qQ/h represents the nuclear quadrupole interaction between $\mathbf{Q}$ and EFG. η is the asymmetry parameter of EFG [25].

These three frequencies are often well separated and can be excited and observed individually. From Eq. (2.2), we can see that NQR resonant frequencies are proportional to the principal values of the EFG tensor around the nuclei. The EFG can be impacted by many molecular factors, such as bonding, valence, electrons, etc. In fact, the NQR frequency spectrum of a particular material is much more complicated than just having three tones. Some

explosive materials have multiple molecules on the crystal lattice. Each of the molecules may have several ^{14}N nuclei that experience different local EFGs. For instance, TNT has a total of 36 NQR frequencies [71]. Even though a sample material may have many NQR frequencies, these frequencies are nevertheless determined by the inherent chemical structure of the sample material. Hence, the NQR frequency distribution, often called the NQR frequency spectrum or NQR signature, is unique for each type of explosive substances [34]. According to the literature record [73], the NQR technique has been used on more than 10 thousand of substances for around 30 types of nuclei. No identical NQR frequencies have been found. The NQR frequencies of explosive substances usually locate in the range from $500kHz$ to $6MHz$.

For the explosive detection application, the one frequency among these resonance frequencies that carries the strongest energy is captured and regarded as the feature frequency of this sample material. However, in realistic materials, the actual NQR signals distribute in a narrow band instead of in a single tone. Variations of temperature, imperfections in the crystal lattice and magnetic interactions between two nuclei can impact the EFG around each particular nucleus in the same substance. Since the NQR frequency of nuclei is extremely sensitive to EFG, NQR frequencies for all the nuclei across the whole sample scatter closely around the theoretical NQR frequency [26, 72].

From the macroscopic view, similar to NMR, NQR detection can be explained by irradiation and precession of ^{14}N spins. Similar to Fig. 2.3, the process is illustrated by Fig. 2.7. Given the absence of $\mathbf{B}_o$, the reference axis is chosen as the direction of the ^{14}N spins in the equilibrium state. Thus, before the excitation signal is applied, the ^{14}N spins are along the reference axis. The excitation signal is actually a high power RF pulse signal at the NQR resonant frequency of the sample material being tested. The width of the RF pulse is denoted as τ. This RF pulse is driven into a coil that surrounds the sample to induce an oscillating magnetic field, whose amplitude is equal to B_1. The magnetic field tilts the ^{14}N

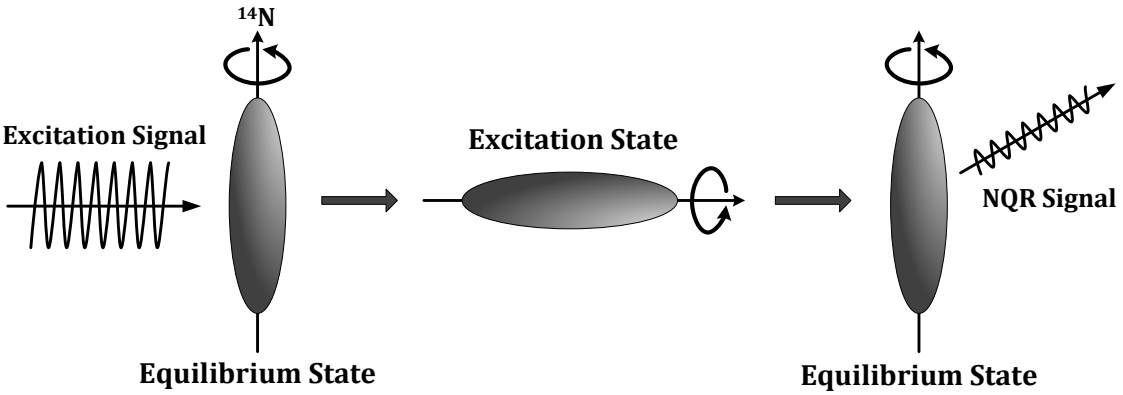

Figure 2.7: Illustration of NQR signal excitation.

spins from the reference axis by a conceptual angle α , which is known as the flip angle. α is proportional to B_1 and τ:

$$\alpha = \gamma B_1 \tau \tag{2.3}$$

where γ is the gyromagnetic ratio. For ^{14}N, γ is equal to $1.932 \times 10^7 rad\ s^{-1}\ T^{-1}$. Then, during the process that the ^{14}N spins precess back to the equilibrium state, a decaying RF signal, which is often called the free induction decay (FID) signal, is emitted and can be detected on the same coil or on a secondary receiving coil.

The time constant by which the sample returns back to the equilibrium state is called *Spin-lattice relaxation time*, denoted as T_1. For general explosive materials, T_1 may last from tens of milliseconds to seconds [26]. Note that the decaying time of FID signals is much shorter than T_1. As stated previously, the actual NQR signals distribute in a very narrow band instead of in a single tone due to crystal lattice imperfection in the sample and temperature distribution variation throughout the sample. The NQR frequencies of the ^{14}N nuclei will be slightly different from the ideal values. When the ^{14}N spins precess after the RF pulse is applied, the small frequency differences from different spins lead to phase differences between the signals which make them add up incoherently and eventually cancel out, which occurs much earlier than the sample actually returns to the equilibrium state.

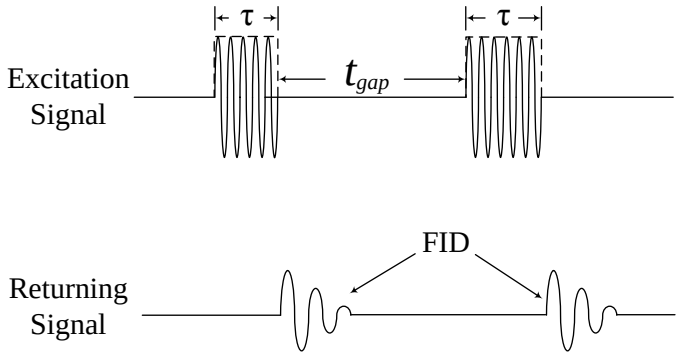

Figure 2.8: Illustration of FID signals in time domain.

The time constant for FID decaying is denoted by T_2^*. Obviously, T_2^* is not only determined by the inherent molecular structure of the sample material, but also affected by the current condition of the sample. Therefore, even for the same material, T_2^* may vary from sample to sample. For explosives, T_2^* often has a value between tens of μs to tens of ms [71].

The strength of FID signal depends on the flip angle α. Intuitively, the highest NQR signal strength can be achieved when $\alpha = 90°$. In real experiments, the results show that NQR signals' highest strength is actually seen when $\alpha = 119°$ [34]. Conventionally, the pulse width that leads to the maximum FID signal power is still referred to as 90° pulse width. Even with optimized α, however, the resulting FID signal induced by one excitation RF pulse is still very weak such that the SNR of the signal is too low to make an accurate detection decision. Therefore, most of the NQR explosive detection systems actually perform the detection by repeating the detection cycles many times. The resultant NQR signals are captured in the time intervals in between the RF pulses. The length of the time intervals are denoted as t_{gap}, as shown in Fig. 2.8. The captured NQR signal during each time interval is called one segment of the whole NQR detection process. Then, all the segments are averaged to increase the SNR so that the detection accuracy can be improved accordingly. The time

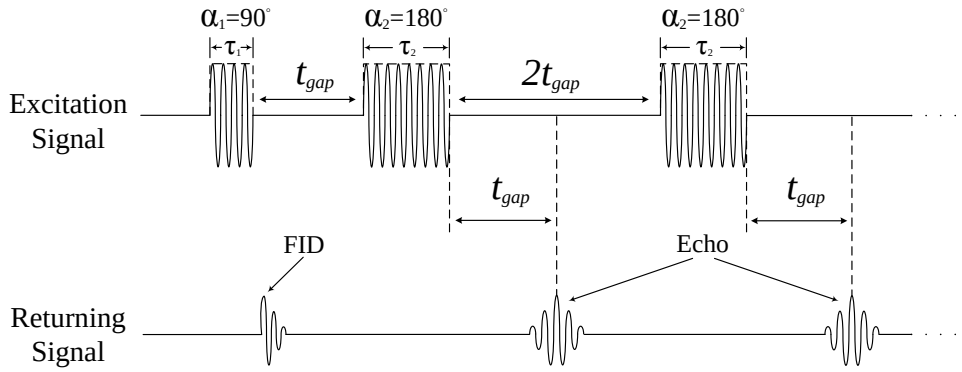

Figure 2.9: Illustration of echo signals in time domain.

domain FID signal for this multi-pulse measurement is illustrated in Fig. 2.8. One matter to be emphasized is that the testing sample has to begin with the equilibrium state for each individual FID signal detection cycle. In other words, after each detection cycle, t_{gap} has to be longer than $5T_1$ in order to guarantee this initial condition. Hence, the detection process with multiple excitation pulses will take long time to finish.

Besides the FID signal, the echo signal is the other type of NQR signals that can be generated by manipulating the flip angles of the spins in different detection cycles. It requires at least two RF pulses with different phases to produce an echo signal. Echo signals in the time domain are shown in Fig. 2.9. The mechanism of generating echo signals can simply be interpreted as refocusing the outphased FIDs. After applying the first RF pulse, an FID signal is generated. With given B_1, τ_1 is usually adjusted to be the 90° pulse width so that the FID signal strength is maximized. As the ^{14}N spins have slightly different NQR frequencies, the emitted NQR signals are soon out of phase and the resultant FID signal decays very fast as expected. Then, a second RF pulse with a width τ_2 is applied. τ_2 is adjusted to achieve a flip angle equal to 180°. Thus, all of the outphased ^{14}N spins are flipped 180° which makes the spins start to precess towards the opposite direction. Consequently, all of the spins are

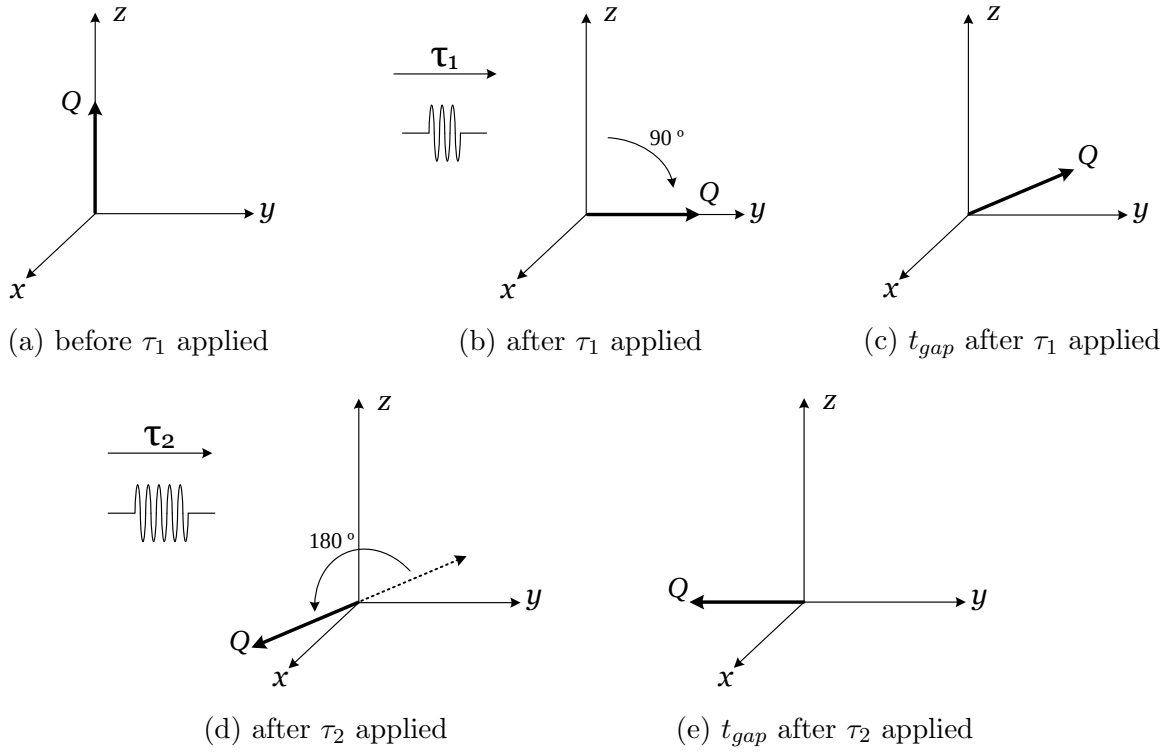

(a) before τ_1 applied (b) after τ_1 applied (c) t_{gap} after τ_1 applied

(d) after τ_2 applied (e) t_{gap} after τ_2 applied

Figure 2.10: The status of an electric quadrupole moment during the echo signal generation

refocused at the time t_{gap} after the second pulse, and a strong NQR signal is radiated.

Fig. 2.10 illustrates this process from an electric quadrupole moment's view. At the beginning, the electric quadrupole moment Q is at its equilibrium state, as shown in Fig. 2.10 (a). After the pulse with the width τ_1 is applied, it rotates on the z axis with an angle of 90° and precesses back to 0° gradually, as shown in Fig. 2.10 (b). Fig. 2.10 (c) illustrates the status of Q at the time t_{gap} after τ is applied, at the point of time right before the τ_2 wide pulse is applied, where Q is not completely back to the equilibrium state yet. Then the τ_2 is applied (Fig. 2.10 (d)), the direction of Q is flipped 180° by this new excitation signal and starts rotating and precessing in the opposite direction. Then at t_{gap} after τ_2 (Fig. 2.10 (e)), Q just precesses back to the 90°. That is when the echo signal is formed.

An interesting example introduced in [75] can help to vividly explain the mechanism of

generating echo signals. We can imagine ^{14}N spins as several running racers that line up at the start point. The first pulse is the starting whistle given by the referee. At the beginning of the race, although the speed (the NQR resonant frequency) for each racer is different, the distance between the racers is relatively small. In the NQR case, the emitted NQR signals are added up coherently at the very beginning. As the running time gets longer, the distances between racers become larger. It means that the emitted NQR signals from the spins are added up incoherently by which the FID is introduced. After t_{gap} length of time, the second pulse is applied. This can be imagined as the referee gives the second order to the racers to turn back and run towards the start point at the same speeds they are running. Then, just as all the racers will return to the start point at the same time, the NQR signals of the spins are in phase again, and an echo signal is formed. The time at which the echo signal reaches its peak value is exactly equal to t_{gap} after the second pulse. An animated illustration of this process is also shown in [76]. The echo signal is often named as Hahn Echo to honor Erwin Hahn, who first demonstrated the echo signal in NMR experiments [77].

As the echo signal generation is a process of refocusing FIDs and relaxing again, the shape of echo signals is analogous to the addition of two back-to-back FID signals. Therefore, an echo signal rises and decays with the same time constant T_2^*. Another property of the echo signal is that its signal strength depends on the length of the time interval t_{gap} between the first excitation pulse and the second refocusing pulse. The peak strength of the echo signal will decay with a time constant, T_2, which may range from tens of ms to several s, and is usually shorter than T_1. Long T_2 can be beneficial for the explosive detection so that multiple echo signals can be generated by using an RF pulse sequence, as shown in Fig. 2.9. Just as with the detection of FID signals with an RF pulse sequence, the captured multiple echo signals can be averaged to increase the SNR. Furthermore, the time for echo signal detection using an RF pulse sequence is significantly shorter than that of the FID detection.

For the former, the total length of the RF pulse sequence, which contains n RF pulses, is $n \times 2t_{gap} \leq 5T_2$ and constrained by the value of T_2. For the latter, the total detection time will be $n \times t_{gap} \geq n \times 5T_1$, not mentioning that T_1 is usually larger than T_2 [71].

In the past decades of NQR technology research, many patterns of RF pulse sequences have been proposed to induce echo signals, such as steady-state free precession (SSFP) [81], pulsed spin locking (PSL) and strong off-resonance comb (SORC) [48, 74].

2.2 NQR Signal Models

Based on the generation mechanisms, the collected NQR signals can be divided into two categories — FID signals or echo signals. Depending on the detection environments and experiment setups, a certain amount of noise and interference may corrupt the NQR signals. In this section, signal models of FID and echo signals are presented. Although simultaneously detecting multiple NQR resonant frequencies is rarely performed in the realistic explosive detection, signal models with multiple resonant frequencies are still discussed here to keep the generality. Also, we only consider the ideal case that the resonant frequencies are in a single tone instead of scattering in narrow band as in real explosive detection.

A FID signal is usually induced by a single excitation RF pulse. Even for the FID detection using an RF pulse sequence, in fact, each FID signal segment is still generated individually by each pulse in the sequence, with a long t_{gap} in between the pulses to guarantee the spins back to the equilibrium state. Therefore, a FID signal that contains d resonant frequencies can be modelled by

$$y(t) = \rho \sum_{k=1}^{d} K_k e^{-[\beta_k + i\omega_k(T)]t} + n(t) \tag{2.4}$$

where $i = \sqrt{-1}$. The subscript k for a parameter indicates that this parameter is for the

k^{th} resonant frequency. β_k, which depends on T_2^* of the sample, is the damping factor for the signal. $\omega_k(T)$ is the k^{th} NQR resonant angle frequency which is a function of the test temperature T. If T changes over a small range, $\omega_k(T)$ can be characterized by $\omega_k(T) = a_k - b_k T$, where a_k and b_k are the constants for a specific explosive substance. ρ is the common magnitude coefficient determined by the power of the applied RF excitation signal. K_k is a known relative scaling factor for the amplitude of the k^{th} component. $n(t)$ denotes the additive noise collected with the FID signal. In [58], $n(t)$ is characterized by an autoregressive model.

The FID signal model is fairly simple and straightforward to understand. The echo signal sequence, however, is very complicated to model as it results from multiple excitation pulses. Moreover, it involves multiple decaying factors. Normally, an NQR echo signal sequence with d possible resonant frequencies induced by an RF excitation pulse sequence can be represented by [56]:

$$y^m(t) = \rho \sum_{k=1}^{d} K_k e^{-\eta_k(T)(t+m\cdot 2t_{gap})} e^{-\beta_k|t-m\cdot 2t_{gap}+t_{gap}|+i\omega_k(T)t} + n(t) \tag{2.5}$$

where $y^m(t)$ denotes the m^{th} single NQR echo signal excited by the m^{th} RF pulse in the RF excitation pulse sequence. $y^m(t)$ is also called the m^{th} segment. Compared to the FID model, a new damping factor $\eta_k(T)$ is introduced for the whole echo signal train of the k^{th} resonant frequency. As discussed in Section 2.1, $\eta_k(T)$ is determined by T_2 of the sample. t_{gap} is the time interval between the first and second pulses. As shown in Fig. 2.9, the time interval after the second pulse becomes $2 \cdot t_{gap}$.

In order to help better understand the above model, a noise free NQR echo signal generated using Eq. (2.5) is shown in Fig. 2.11. From Fig. 2.11, we can see that there are 12 echo signals (segments) in the sequence. Each segment has a decaying time constant, which is T_2^*. And T_2 is the decaying time constant of the peak values in the sequence, which is also

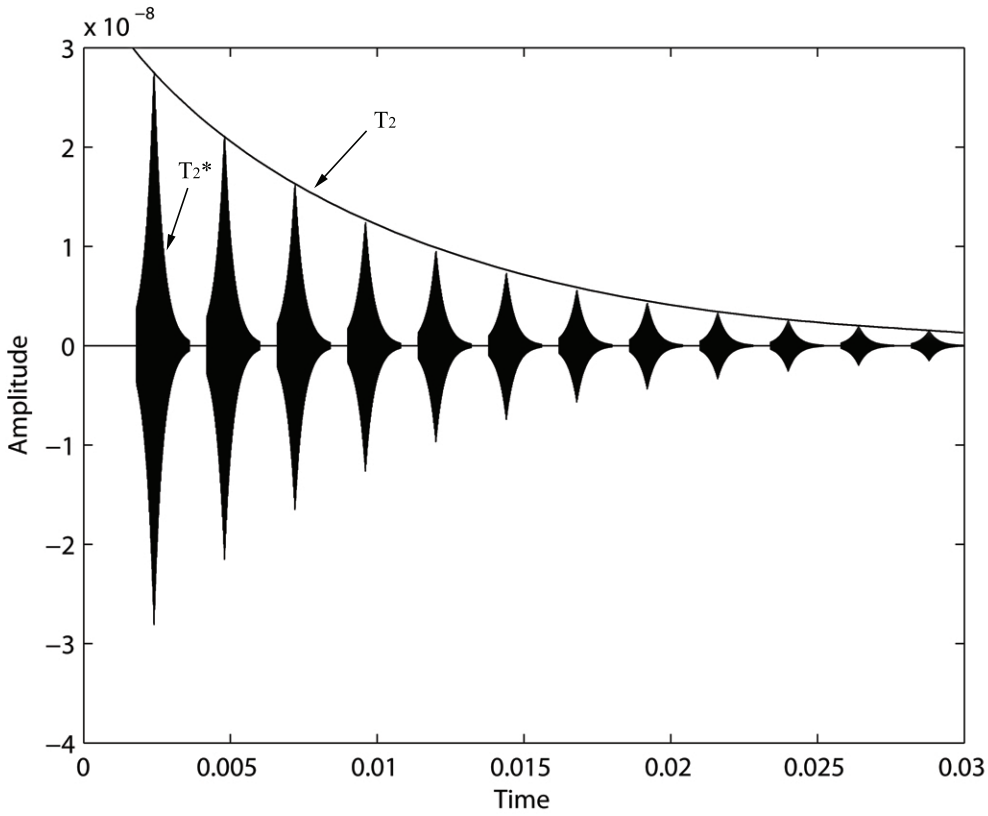

Figure 2.11: Noise free NQR echo signal sequence in the time domain.

indicated in Fig. 2.11.

2.3 Conclusion

The background of NQR detection is introduced in this chapter. The discussion starts with explaining the NMR principles. The NMR utilizes the interaction between the nuclear magnetic moment and the external magnetic field. The NQR, on the other hand, exploits the interaction between the electric quadrupole moment of the nucleus and the electric field gradient (EFG) that surrounds the nucleus. Thus, the advantage of the NQR over the NMR is that the NQR does not require the presence of an external magnetic field.

For NQR-based explosive detection, only the materials containing ^{14}N with $I = 1$ are of interest. For these types of materials, with the excitation by an applied RF pulse, the ^{14}N spins may transit from the equilibrium state to the excited state. When the excitation RF signal ceases, the spins precess back to the equilibrium state, and therefore emit NQR signals. These signals can be captured by a nearby coil. To improve the SNR of the captured signals, an RF pulse sequence might be used instead of a single RF pulse. There are two types of NQR signals that can be captured during the detection — FID and echo signals. The models of these two signals have been presented.

Chapter 3

NQR-Based Portable Explosive Detection System

The goal of this work is to develop a portable explosive detection system solution. To that end, all the hardware design options adopted for this system have to satisfy the low-power and compact-size design requirements. Meanwhile, the sensitivity and reliability are also important factors to be considered. In this chapter, the design considerations from the system-level's perspective are discussed. First, the general design requirements for NQR systems are depicted. Then, by reviewing some traditional and classic NQR detection system designs, the limitations of the existing systems are discussed. Finally, an overview of the proposed NQR-based portable explosive detection system is presented.

3.1 General Design Requirements for NQR Systems

From the NQR physical principles described in Chapter 2, the hardware design of NQR detection systems seems to be simple. During the excitation period, it requires a high power RF signal generator to induce the oscillating magnetic field through the NQR coil. This part

of the system is the TX section. During the receiving period, a receiver which is sensitive enough to capture the weak NQR signals. This is the RX section. As a matter of fact, the actual NQR systems are much more sophisticated than that.

3.1.1 Transmitter Section

According to Section 2.1, the NQR detection procedure starts with generating an RF magnetic field around the sample. This can be fulfilled by driving an oscillating current into an coil. In essence, the actual excitation signal is the oscillating magnetic field whose amplitude is determined by the current flowing through the coil. From the transmitting power efficiency's point of view, less power consumed to generate the same amount of oscillating current inside the coil leads to higher power efficiency of the transmitter section. Therefore, in order to fully utilize the power delivered by the RF signal generator, as shown in Fig. 3.1, along with the coil, a capacitor C is often used to form either a parallel or a series LC network that resonates at the desired NQR frequency.

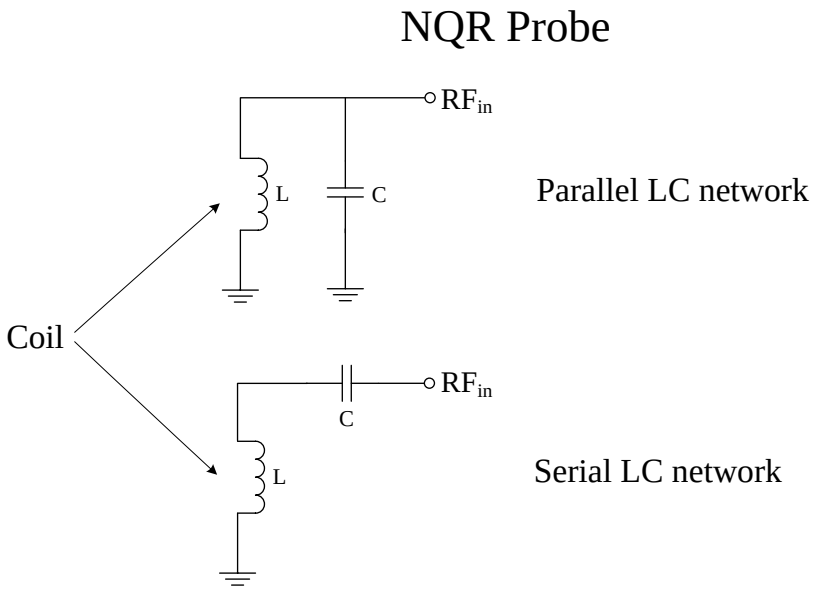

Figure 3.1: The LC NQR probe

To maintain the same current amplitude in the coil, less power is dissipated with smaller series resistance of the LC tank. The small series resistance means that the LC tank needs to have a high Q factor. Hence, in order to achieve high power efficiency during the transmission period, a high Q factor of the LC network is desired. Note that the Q factor of the LC network is dominated by the series resistance of the coil due to the fact that capacitors usually have much higher Q values compared to the coil. On the other hand, after the excitation signal stops, the dissipation time of the residual excitation power in the NQR probe is proportional to the Q of the LC network. A high-Q NQR probe will have long ringing time. As the FID signal appears right after the excitation signal, the residual power needs to be eliminated as soon as possible. Otherwise, either the detection has to wait for the ringing to cease, or the collected FID signal is interfered with the ringing signal. To address this problem, a Q damping circuit is required to switch the Q factor to a lower value such that the ringing time can be shortened.

Another property which is essential for the echo train detection is the programmability. To adapt the excitation signals to various explosive materials under complicated detection conditions, the parameters of the excitation RF pulse sequences, such as the pulse width τ_i, the gap between each two pulses $t_{gap,i}$, the frequency of the RF signal ω_o, and the amplitude of the RF signal, need to be configurable. The configurability by means of software programs is beneficial to improve the versatility of the system.

Certainly, for portable detection systems, the power efficiency of the RF signal generator itself is also appreciated. In order to realize programmability, the signal pattern has to be initiated from a low voltage power grid. Then, a power amplification circuit is employed to magnify the signal to a desired power level. As the excitation signals delivered to the NQR probe have a high power level, the power wasted on the power amplification circuit is a big portion of the overall power consumption of the system. As the power budget for portable systems is extremely limited, the efficiency of the power amplification circuit is critical to

reduce the power consumption during excitation period. Moreover, since the detection time is usually much longer than the excitation period, the power consumption of the transmitter section in the idle state is also important. The idle time of the transmitter section and receiver section are illustrated in Fig. 3.2. τ_1 and τ_2 are the excitation durations while $t_{gap,1}$ and $t_{gap,2}$ are the detection periods. During τ_i, the transmitter is on whereas the receiver is idle, and vice versa in $t_{gap,i}$. If the idle-power and on-power of the transmitter and the receiver are denoted as P_{TX_idle}, P_{TX_on}, P_{RX_idle}, and P_{RX_on}, respectively, the average power consumption P_{sys} can be computed by

$$P_{sys} = \frac{\sum_i [(P_{RX\_idle} + P_{TX\_on})\tau_i + (P_{TX\_idle} + P_{RX\_on})t_{gap,i}]}{\sum_i [\tau_i + t_{gap,i}]} \tag{3.1}$$

As the transmitter section delivers high power signals to the NQR probe during the exci-

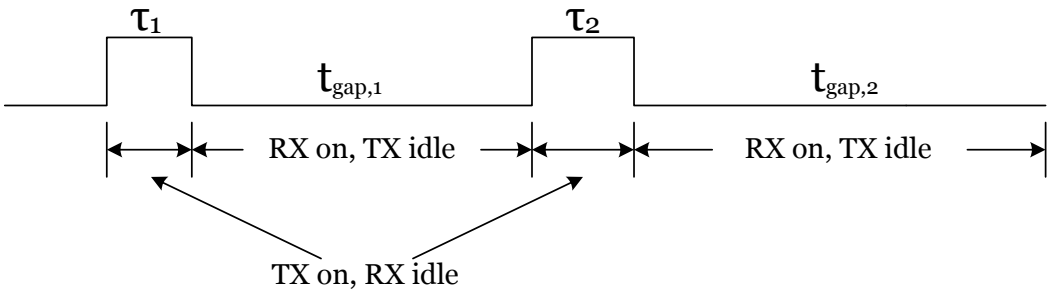

Figure 3.2: Detection sequence and power computation

tation period, a power multiplexer is needed to isolate the receiver section from the probe in the meantime. During the receiving period, the power multiplexer connects the receiver section back to the probe. Since NQR signals are very weak, the power multiplexer also needs to have low signal attenuation while it is in on-state. Moreover, this power multiplexer should have fast switching capability for collecting FID signals, as FID signals will decay very quickly.

3.1.2 Receiver Section

After the excitation period, the RF excitation magnetic field ceases. The ^{14}N spins precess and introduce a weak oscillating magnetic field which is usually in the direction of the RF excitation magnetic field. The traditional and mainstream technique for sensing this oscillating magnetic field is *Faraday Detection*. The Faraday NQR signal detection relies on Faraday's law of induction: the oscillating magnetic field can induce an oscillating current signal in the surrounding coil that is in a close loop circuit. This coil is often the same one that is used to generate the RF excitation magnetic field. Although in some designs, such as the baggage scanner proposed by Grechishkin in [36], and the one proposed by Rudakov in [81], a separate receiving coil is used for the detection task, the single coil design is still preferable due to its simplicity and low cost. Many ideas and solutions have been proposed for how to design the NQR coil. For lab equipment, solenoid coils are often employed because the sample can be put inside the coil, and thus the magnetic field are fully utilized. For field applications such as landmine detection, a flat pattern coil is often used. Moreover, there are some coil designs which provide more robust interference rejection performance [41, 42].

In terms of the receiver section circuit design, by revisiting the NQR probe configurations in Fig. 3.1, we can see that the parallel LC NQR probe is more desirable. The reason is that the parallel LC network is able to directly convert the induced current signal into the voltage signal. For the following signal amplification circuit, voltage signals are much easier to handle than current signals. In the following discussion, we assume that the receiving NQR probe is configured in the fashion of the parallel LC network.

3.1.2.1 Sensitivity of NQR Detection

As the resulting oscillating magnetic field from the ^{14}N spin precession is very weak inherently, the voltage signals picked up by the NQR probe also have very low power. In fact,

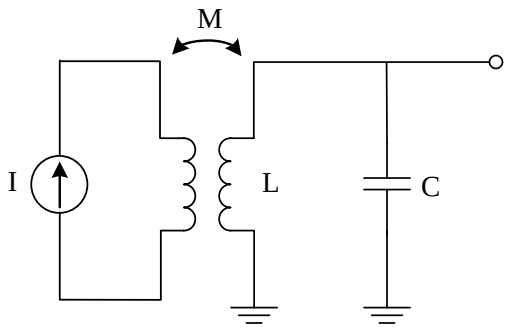

Figure 3.3: The model of Faraday NQR detection

the signal strength is at the same power level as the thermal noise in the NQR coil. The low signal-to-noise ratio (SNR) is a main concern for the NQR system design. To analyze the NQR signal strength and noise sources, we use the NQR detection model proposed in [26] for further discussion.

In [26], the authors modelled the Faraday NQR detection as mutual inductance coupling from the sample to the NQR probe. Since the detailed derivation and proof have been fully presented in [26], in this context, only a brief summary of the detection model is presented. As depicted in Fig. 3.3, the sample is modelled by a current source I, which can be represented by

$$I(\omega) = \beta \frac{\omega m \xi}{VT} \tag{3.2}$$

where ω is the NQR angle frequency of the sample. β is a constant to describe the relation between the characteristics of the sample material and the strength of the NQR signal. It is specific for a certain type of material. T is the test temperature. m and V are the mass and volume of the sample under test, respectively. ξ is the physical spatial distribution factor of the sample.

Then, the current signal is converted to a voltage signal by an LC network. Different

structures of the NQR probes may yield different voltage signals. Fig. 3.3 shows one of the possible configurations, which only consists of an NQR coil and a resonant capacitor. The power matching scheme of this configuration is often called the infinite impedance matching network. The induced voltage signal V_s by the probe configuration in Fig. 3.3 will be:

$$V_s = \omega M I Q \tag{3.3}$$

where Q is the quality factor of the NQR coil. And M is the coupling factor which depends on the spacial relation between the sample and the NQR coil. This spacial relation involves many aspects, including the coil setup, the sample filling factor, etc. For different coil setups, the value of M varies in a wide range. Solenoid coils may lead to the maximal M value compared to flat wire coils. Given the same coil, if the sample spreads wider and occupies more space in the effective magnetic field area (a higher filling factor), the resulting M is larger. For the flat wire coil, M decreases exponentially with respect to the increase of the distance between the sample and the coil [26].

Different from Eq. (3.3), the traditional NQR probe, as shown in Fig. 3.4, may produce a different voltage signal. The resulting NQR voltage signal is

$$V_s = \omega M I \sqrt{\frac{Q R_o}{\omega L}} \tag{3.4}$$

where L is the inductance of the NQR coil. For this type of NQR probe, a power matching network is usually used to form the output impedance $R_o = 50\Omega$, thus to match the input impedance of the driving power amplifier in TX section and the receiving signal amplifier in RX section (the TX and RX sections share the same probe). This power matching scheme is often referred to as 50Ω power matching network. The comparison of 50Ω matching strategy and the aforementioned infinite impedance matching strategy will be discussed in detail in

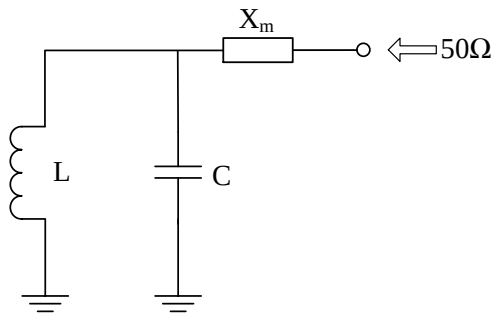

Figure 3.4: The NQR probe with 50Ω matching network

Chapter 5.

One thing that needs to be emphasized for this discussion is that in both cases, the amplitude of V_s is proportional to the Q value of the NQR coil. In another word, a high Q value is also desired during the detection period. Hence, the Q damping circuit should only switch Q to a low value during ringing suppression, and switch it back to a high value afterwards.

If only considering the NQR probes for noise analysis, the thermal noise of the NQR probe resistance is the main contributor. We use the traditional probe as the example to discuss the thermal noise here. The noise signal for this type of NQR probe can be derived by

$$\sqrt{\overline{V_n^2}} = \sqrt{4kTR_oB} \tag{3.5}$$

where B is the bandwidth of the NQR signal and k is the Boltzmann's constant.

By definition, the SNR will the ratio of V_s to $\sqrt{\overline{V_n^2}}$. To have a quantitative idea of the SNR, we can use an example given in [71]. If the 50Ω matching method is adopted to construct the NQR probe, and the bandwidth is $1kHz$, the noise voltage is approximately $29nV$. The NQR probe used in this method has a coil with $Q = 200$ and $L = 1\mu H$. The

sample fills all of the coil volume. If a single NQR frequency of 840kHz is monitored for a $m = 100g$ TNT sample, the estimated RMS NQR signal using this model is $47nV$, which results in $SNR = 1.6 = 4\ dB$.

In a realistic detection system, the amplifiers along the signal processing chain also contribute to the noise power. In theory, the noise factor of a detection system is defined as the ratio of the total output noise power of the system to the portion of the output noise power directly caused by the input noise power. The noise factor is mainly constrained by the first amplifier stage. Therefore, a low noise amplifier (LNA) is desired to realize the initial amplification of NQR signals.

From the example given above, we can see that the SNR for detecting a single NQR signal is fairly low. Thus, it may not be able to achieve high detecting accuracy by making the decision based on just one NQR signal, collected in one detection cycle. As stated in Chapter 2, NQR signal segments excited by an RF excitation pulse sequence, both for FID and echo signals, are often collected to improve the SNR. For the noise signal, it is stationary and uncorrelated in time. For the NQR signal segments, they are correlated and can be added up coherently. Hence, if n NQR signal segments are averaged, the noise power will be reduced to $1/n$ whereas the NQR signal power stays the same. As a result, the SNR is increased by n times. As far as the post-processing unit is concerned, a large memory buffer is desired to store the data collected in the multiple detection cycles.

3.1.2.2 Other Approaches to Improve the Sensitivity

According to Section 3.1.2.1, the sensitivity of Faraday detection is considerably degenerated by the thermal noise of the NQR coil. To relieve this situation, researchers proposed some alternative techniques to improve the NQR detection sensitivity.

To reduce the thermal noise of the NQR coil, a straightforward method is to cool down the coil. Copper is generally the material used to fabricate the NQR coil. It is well known

that the resistivity of copper is lower than most of conductive materials except silver. In the room temperature ($T = 20^o$), copper has the resistivity equal to $\rho = 1.697 \times 10^{-8}\ \Omega \cdot m$. The temperature coefficient of copper is $\alpha = 3.95 \times 10^{-3}\ /^oC$. If liquid N^2 is used for cooling (its boiling point is $-196\ ^oC$), using the resistance temperature equation $\frac{\Delta\rho}{\rho_o} = \alpha * \Delta T$, the copper resistivity drops to $0.517 \times 10^{-8}\ \Omega \cdot m$, almost just 30% of its value at the room temperature. According to Eq. (3.5), the noise voltage signal is proportional to $\sqrt{R}$. As a result, the noise voltage decreases to 54.8% of its value at the room temperature. Meanwhile, the signal gain also increases as it is proportional to Q which increases with resistance decreasing.

Compared to cooled copper, a superconductor has even lower resistivity. Some NQR and NMR equipment using the coils made of superconducting materials has already been reported [78, 79]. However, a high Q factor of the superconductor coils brings some inconvenience for the detection. Due to the high Q, the ringing down time is longer. Also, the detection bandwidth is very narrow so that when the test temperature changes, the NQR frequency may shift out of the probe bandwidth.

Another low noise NQR detection technique uses superconducting quantum interference devices (SQUID) to detect the change of the magnetic field [52, 80]. A SQUID is a superconducting material loop, segmented by some Josephson tunnel junctions. Unlike Faraday detection, it senses a DC magnetic flux by conducting a DC current inside the loop. Therefore, it is very sensitive at a low frequency, around hundreds of kHz. The regular amplifiers have very noisy behaviour as the main noise source is $1/f$ noise in this frequency range. Moreover, SQUID detection has extremely low noise contribution. A detection resolution of $1\ fT/\sqrt{Hz}$ for a SQUID-based NQR detection system is reported in [52].

Despite of their high sensitivity, the superconductor-based detection techniques are not preferable for field applications. The reason is that it requires a large system volume to maintain a low temperature for generating the superconducting phenomenon. Furthermore, since superconductor coils have extremely high Q factors, it is very sensitive to the mechanical

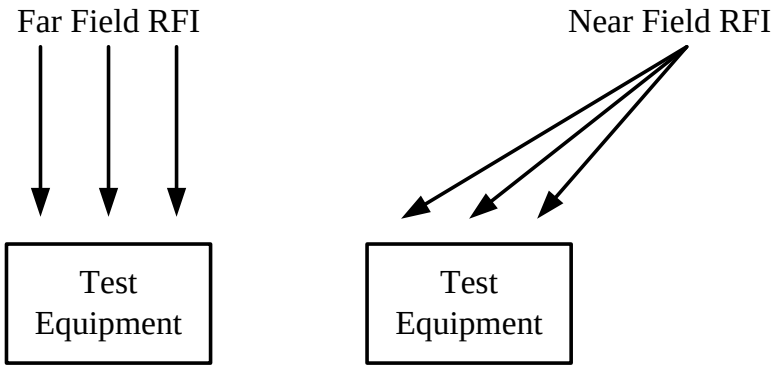

Figure 3.5: Far field and near field RFI

vibration, which is inevitable for mobile detection systems.

3.1.2.3 Radio Frequency Interference

As the NQR signals are inherently weak, they are vulnerable to RFI from other sources. The interfering sources may include electrical equipments, power lines, and most severely, commercial and amateur radio stations. Basically, depending on the distance from the interfering source, they can be divided into two categories — far field RFI and near field RFI. Commercial AM radios, whose frequencies range from $500kHz$ to $1.5MHz$, are the biggest far field RFI sources. Usually it is assumed that the far field RFI is uniformly distributed, as shown in the left half of Fig. 3.5. For the test equipments, the amplitude and orientation of RFI are all equal in the surrounding space. Near field RFI, as shown in the right half of Fig. 3.5, is generated from a source close to the test equipment. Actually, it may come from the NQR test equipment itself. If no precaution is taken, the ratio of the NQR signal power to to RFI power can be as low as $-60dB$ [26].

So far, the most effective method to reject RFI is still shielding. For lab test equipments and stationary security screeners, shielding the testing sample and the detection system is

applicable and reliable. But for field applications, such as landmine detection or mobile bomb detection, shielding is impractical owing to the fact that the detection targets often cannot be enclosed. To address the RFI problem for these applications, several techniques have been proposed.

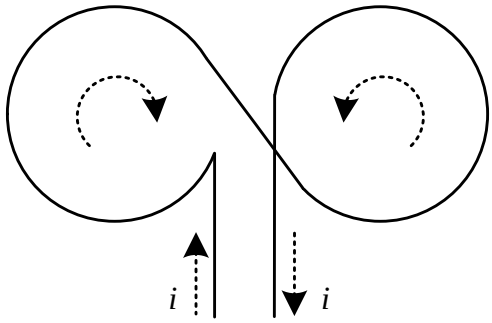

Figure 3.6: A simplified gradiometer for RFI Cancellation

The first technique is to use a special NQR coil, named the gradiometer coil [39, 40, 41]. The regular NQR coils normally respond to the presence of any magnetic fields. However, the gradiometer coil has two sets of turns in the same plane, and it only captures the magnetic field gradient between these two sets. As shown in Fig. 3.6, the currents in these two sets of turns flow in the opposite direction with each other. Therefore, if a uniformly distributed magnetic field (far field RFI) encounters the gradiometer coil, the currents induced in the two turns will cancel out one the other. On the other hand, the NQR sample is placed near the gradiometer coil. Thus, the currents introduced by the NQR signal in the two sets of turns will be different, and the current gradient between the two sets will be picked up. Obviously, the limitation for this technique is that the gradiometer is not immune to the near field RFI.

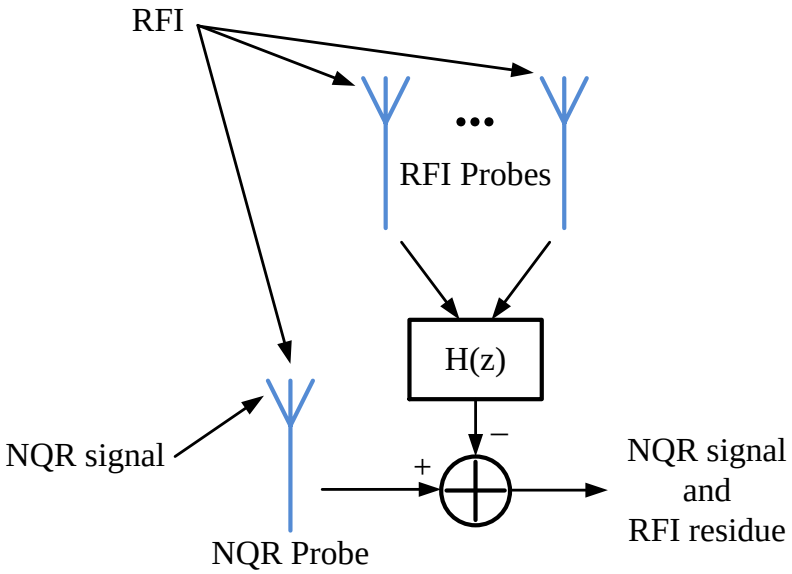

Figure 3.7: Architecture of multi-probe RFI cancellation

Another RFI cancelling method employs one or multiple auxiliary probes, often referred to as RFI probes, dedicated to picking up RFI. The architecture of a system with multiple RFI probes is depicted by Fig. 3.7. RFI can be picked up by both of the RFI probes and NQR probe whereas the NQR signal can only be sensed by the NQR probe. The RFI captured by the RFI probes is transformed by a linear system $H(z)$ to match the RFI that is received by the NQR probe. The transformed RFI is then subtracted from the signals captured by the NQR probe so that the RFI portion is suppressed, and the NQR signal portion is left for detection. There are two assumptions for this method. First, the RFI probes only pick up RFI, not NQR signals. This assumption holds if RFI probes are positioned far enough from the NQR test sample such that the NQR signals vanish to a power level much lower than the noise power level. According to Section 3.1.2.1, this can be easily achieved as the power of NQR signals decreases exponentially with the distance increasing. In actual detection systems, the RFI probes are often placed several meters away from the NQR probe [56].

The second assumption is that the RFI signals on the NQR probe and on the RFI probes are correlated. Moreover, this correlation can be reverted through a linear system $H(z)$, such that the RFI signals on the RFI probes can be reshaped to match the RFI signals on the NQR probe. For far field RFI, this assumption easily holds as the RFI probes get the identical RFI signals as those captured by the NQR probe. For near field RFI, since the only difference is the phase and amplitude shifts between the RFI signals captured by these two types of probes, they are also revertible by a linear system. By using this approach, both far field and near field RFI is mitigated. The only problem remaining is how to build up the reverting linear system. A popular method employed by most systems today is to use an adaptive filter in the digital domain [55, 59].

3.1.2.4 NQR Signal Processing for Explosive Detection

The detection decision is made based on the processing and analysis of the amplified NQR signals. As mentioned previously, multi-pulse sequence detection is often adopted to enhance the SNR. Traditionally, the signal train is first demodulated with the known NQR frequency, and then digitalized. However, to avoid loss of information, direct digitalization without demodulation is more preferable here. Then, the digitalized signal segments are averaged. If the integrated power of the averaged signal is greater than a pre-defined threshold, a decision is made that explosive of interest is detected. From the hardware's perspective, direct digitalization without demodulation requires a much higher sampling frequency. Fortunately, the advances of analog-to-digital converter (ADC) circuits guarantee that in the NQR signal range from $500kHz$ to $6MHz$, the signals can be oversampled with a high resolution to preserve more useful information. Based on this hardware development, more advanced signal processing techniques for NQR detection have been proposed. As mentioned in Chapter 1, Tantum et al. propose to use an LMS-based adaptive filter to mitigate RFI, and then apply a Bayesian detector for making a decision. Later, the same group of researchers improve the

RFI mitigation by applying the Kalman filtering technique [57]. This detector processes the averaged data in the frequency domain by transforming the data with Fast Fourier Transform (FFT). On the contrary, Somasundaram et al. propose to process the signal in the time domain and use the raw signal train without averaging. Although the assumptions and the theories behind these two detection algorithms are different, one thing they need in common is powerful computation hardware to execute the calculation tasks.

3.1.3 Summary for the Requirements of NQR Systems

Through the above discussion, we summarize the general requirements for NQR detection systems as follows.

For the Transmitter Section:

- A signal source to generate the excitation RF pulse sequence is required. In order to facilitate the NQR detection for different materials in various different environments, a certain level of programmability is desired.
- A high power amplifier is necessary to drive the excitation signal into the NQR probe with a desired power level. Certainly, high power efficiency is always preferable especially for portable systems.
- In order to protect the receiving circuitry during the transmission period, a power multiplexer with high off-state isolation, low on-state signal attenuation, and fast switching is needed.
- A Q damping function needs to be integrated with the NQR probe to quickly stop the residual ringing signal.

For the Receiver Section:

- Considering that the detection performance is significantly influenced by the noise factor, especially the first amplification stage, a low noise amplifier is essential for constraining the noise contribution of the NQR system. In addition, the precaution has to be taken to ensure that the following gain stages do not sabotage the SNR.
- An RFI mitigation method needs to be employed so that the detection performance can be improved with high SIR presence.
- To fulfill the sophisticated signal processing techniques, the data computation module should provide massive storage memory and powerful calculation capability.

In addition, to coordinate all of the functional blocks in the system, a logic control module is required and the programmability of this module is desired.

On top of the above requirements, for portable detection systems, a compact size and low power consumption is always favored.

3.2 Traditional NQR System Designs and Limitations

Many NQR based explosive detection systems have been proposed since the NQR phenomenon was first demonstrated in the 1950's. Depending on the targeted applications, there have been various ways to build the system. No matter what configuration is adopted, the detection system have to meet the general requirements that are summarized in Section 3.1.3. Also, the solutions to address these requirements are essentially similar. In this section, a classic NQR detection system proposed by Smith is used as an example to discuss the traditional designs and their limitations.

Fig. 3.8 shows the block diagram of the NQR detection system proposed by Smith in [33]. The RF source (Block 1 in Fig. 3.8) generates a low power RF signal at the desired

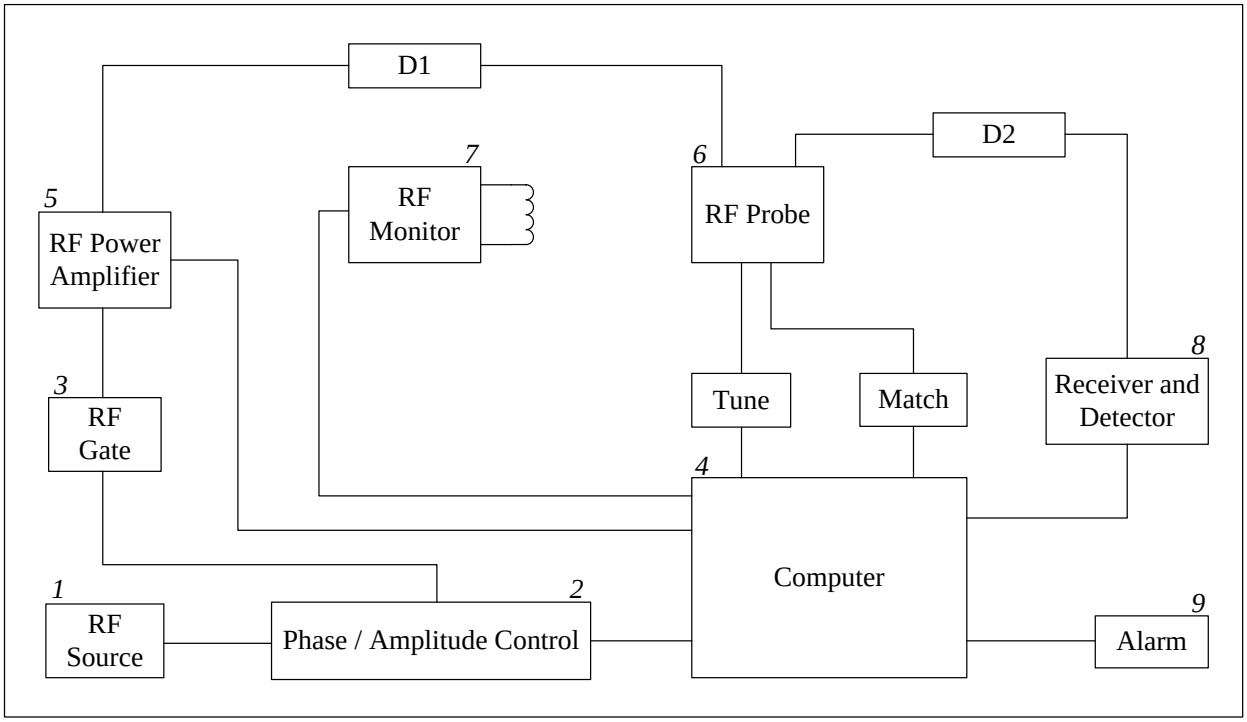

Figure 3.8: Block diagram of the NQR detection system proposed in [33]

excitation frequency. Block 2 is the phase and amplitude control unit. Block 3 is the RF gate that provides the on-off function to generate the RF pulse sequence. Both Block 2 and 3 are controlled by the central computer (Block 4), which is a PC. The RF power amplifier (Block 5) is an off-the-shelf class-AB type power amplifier that is employed to enlarge the power of the excitation RF pulse sequence. A blocking diode pair $D1$ functions as a one-way switch. The purpose of having $D1$ is to provide a low impedance path for the excitation signal and high impedance isolation from the noise generated by the RF power amplifier. Block 6 is the NQR probe which can be tuned for power matching. Block 7 is the RF monitor for the tuning purpose. $D2$ is another one-way power switch to protect the receiver section. It is essentially a quarter wave switch. The receiver and detector (Block 8) consists of a pre-amplifier and a demodulator to transform the signal into the audio signal band. Finally, the signal is fed into the PC for post-processing. If the pre-defined

detection criterion is satisfied, the alarm (Block 9) is triggered. As this system is designed for non-mobile application, an RFI mitigation module is not included. The RFI mitigation is achieved by completely shielding the system from outside RFI sources.

From this example, we can see some limitations of the traditional NQR system solutions.

- The analog RF power amplifier is power consuming because not only it is active during the entire detection period, but also it has low power efficiency when the signal power level is low or varying. Additionally, it still brings extra noise for the NQR probe even though $D1$ is used for noise isolation. Another drawback of the off-the-shelf analog RF power amplifier is its large volume.

- The power multiplexing system constructed by $D1$ and $D2$ is hard to calibrate for detecting different explosives. For different NQR frequencies, the length of the transmission line in $D2$ has to be changed accordingly, which is equal to a quarter of the wavelength. The changeability of $D2$ is very difficult to implement. Also, for the frequency range in NQR detection, which is $500kHz$ to $6MHz$, the quarter wavelength can be as long as $150m$. That also demands a large size and heavy weight.

- A PC can surely provide powerful calculation capability and versatile programmability. However, the power consumption and the large physical size also hinders its mobility.

3.3 Proposed NQR Portable Explosive Detection System

In view of design requirements for NQR detection systems and limitations of the existing systems, in this work, a portable solution that employs state-of-the-art semiconductor technologies is presented. Compared to the traditional NQR detection systems, some new

circuitry schemes and designs are proposed and implemented to address the aforementioned limitations.

The block diagram of the proposed system is shown in Fig. 3.9. This system consists of a transmitter section, an NQR probe, an RFI probe, a receiver section and some auxiliary modules.

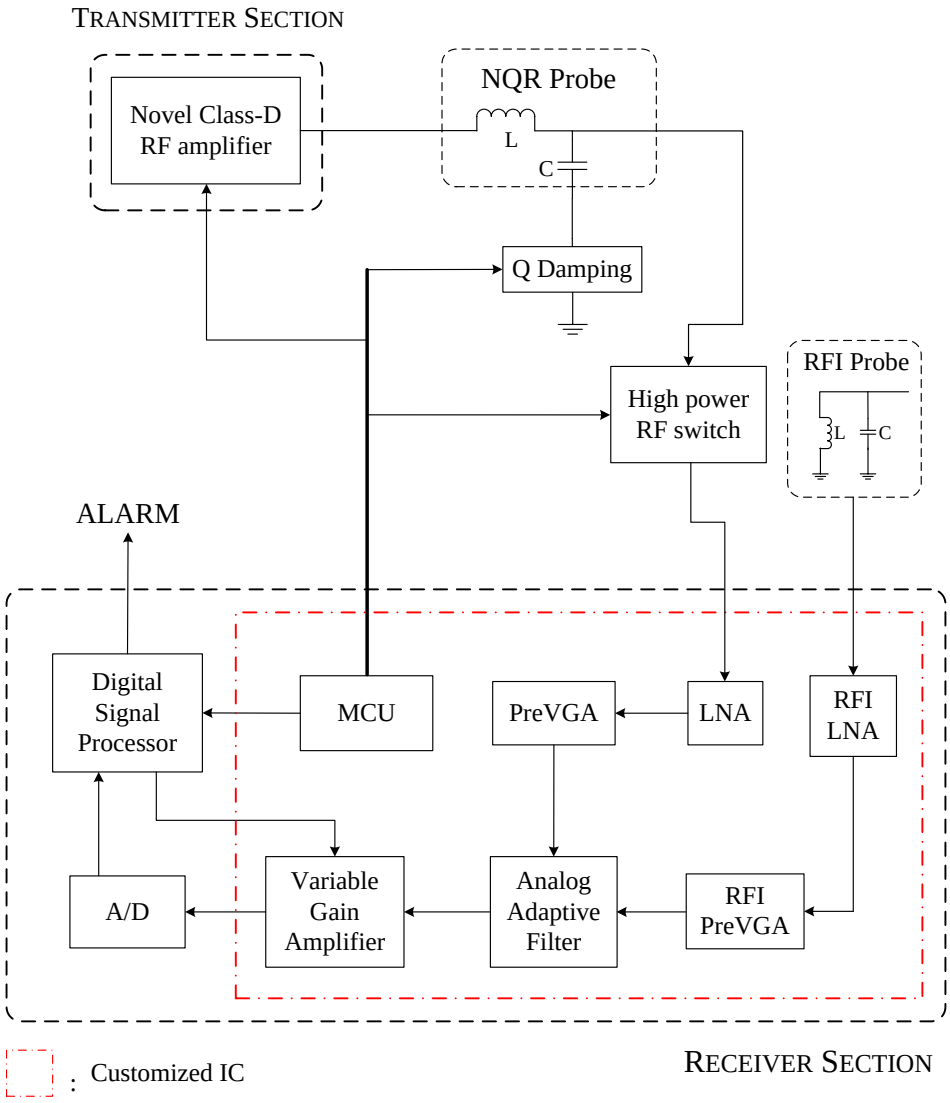

Figure 3.9: Block diagram of the proposed NQR-based explosive detection system

3.3.1 Transmitter Section

In the transmitter section, a novel Class-D type power amplifier is employed and tailored to suit the needs of NQR detection systems. As the NQR probe is basically a LC resonant network, it automatically filters the square wave signal and produces a sinusoid resonant signal inside the probe. Due to its digital control essence, all the analog modules required by traditional detection systems, including the RF source, the phase / amplitude control, and the RF signal gate, can be replaced by a digital control module. This modification greatly simplifies the system design and reduces the overall power consumption. Compared to analog-domain power amplification schemes, Class-D amplifiers generally have a considerably higher power efficiency for generating the same power level of the RF pulse excitation sequence. In addition, a more important advantage of using Class-D amplifiers is that it can be turned off during receiving and idle period. As the receiving period is usually much longer than the excitation period, the power saving thanks to this feature is more appreciable. Furthermore, it is equipped with a special circuit that can fast-start and fast-stop the high power RF pulses to facilitate the rapid acquisition of quickly decaying FID signals. Apparently, an auxiliary Q damping circuit is needed to help the fast-stop function.

3.3.2 Receiver Section

The receiver section is responsible for receiving and detecting the NQR signatures of explosive materials with an acceptable SNR. In particular, this section performs low-noise amplification, RFI mitigation, and NQR signal detection with a low false alarm rate.

The signal path of the receiver section starts with a low noise amplifier (LNA) to amplify the received NQR signals while constraining the noise figure (NF) of the whole signal chain. In this design, a so-called infinite input impedance power matching scheme [82] is adopted for the LNA in order to achieve a low NF. As the LNA can be damaged by the high power

RF signal during the transmitting phase, an RF switch is added to isolate the transmitting signal. On the other hand, during the receiving phase, to detect the inherently weak NQR signal, small additive attenuation and low noise contribution is required for the RF switch. A PIN diode based RF switch is employed to satisfy these requirements. Compared to the traditional quarter wavelength ($\lambda/4$) RF switch, the main advantage of a PIN diode RF switch is its compact size.

In the proposed system, an auxiliary RFI probe with an analog adaptive filter is employed for RFI suppression. The RFI probe is an LC tank that has the same resonant frequency with the NQR probe. It is placed apart from the NQR probe (usually 0.5 to 1 meters) to pick up the background RFI. As the signal from the RFI probe is eventually subtracted from the signal coming from the NQR probe to suppress RFI, the uncorrelated noise of this signal path, such as the thermal noise, will also be transferred to the NQR signal in this process, and decrease the final SNR for detection. Hence, it is equivalently critical to constrain the NF in this signal path. To that end, an RFI LNA is used to achieve this purpose.

Following the LNA, both of the NQR signal path and the RFI path have a pre-amplifier to amplify the signals. To adjust the signal levels from the two paths close to each other, a variable gain controller is included in each pre-amplifier. Then, an adaptive filter is used to perform RFI mitigation in the analog domain. In terms of design complexity for an adaptive filter, a digital adaptive filter is simpler to be realized. However, from the system's perspective, a digital adaptive filter needs additional supporting hardware, such as an additional ADC for the RFI path. Moreover, the detection performance is comprised. To explain this better, we consider an example in a field detection application. We assume that an NQR signal has the SIR equal to $-40dB$. In another word, the interference voltage level is 100 times higher than the NQR signal voltage level. This assumption is fairly reasonable for an unshielded field detection system [26]. If a digital adaptive filter is used for RFI mitigation, each signal path needs to have an ADC. Let us focus on the ADC for the NQR signal path. If

the ADC has n-bit resolution, because of $-40dB$ SIR, the first log_2100 MSBs are corrupted by the RFI. Therefore, the effective resolution decreases to $n - log_2100$. As a result, the detection is compromised in this setup. On the contrary, if the RFI mitigation is performed in the analog domain, it is finished before the quantization. Thus, only one ADC is required to digitalize the RFI-suppressed NQR signal. Theoretically, the whole dynamic range of the ADC can be utilized. In short, if an analog adaptive filter is adopted, as RFI mitigation is handled before quantization, the requirements for high precise ADCs and complex downstream processing algorithms will be effectively relaxed.

After the adaptive filter, a variable gain amplifier (VGA) amplifies the RFI-suppressed NQR signal before it is fed into an ADC. The gain of the VGA can be tuned to adequately utilize the input dynamic range of the ADC, as well as to prevent the signal from saturating the input stage. Then, the NQR signal is digitalized by the ADC and sent to a DSP for the downstream processing. Compared to the traditional system configurations wherein the bulky PCs or other comprehensive computation units are employed, using a DSP as the data processing platform is another advantage introduced by this design. Although PCs can provide versatile programmability and extensive computation power, the state-of-the-art DSPs possess the specialized computational structures to cope with NQR data analysis in the frequency domain while maintain an ultra small volume and low power consumption.

One of the important advantages of the proposed NQR detection system is that the entire analog signal chain is integrated on a mixed-signal customized IC. Additionally, an MCU is included on this IC to fulfill the logic control of the whole detection system. In this way, the DSP dedicates to NQR signal post-processing such that the responding time of the system is further optimized.

Using a customized IC leads to many benefits for the system. The integration level of the receiver section is greatly improved from the traditional discrete circuit component solutions. First, the noise coupling and signal corruption from either outside or between the

Table 3.1: Comparison between the proposed system and the traditional solutions based on the general requirements for NQR detection systems

General Requirements	**Traditional Systems**	**Proposed System**	**Improvements**
Programmable RF sequence signal source	RF oscillator with RF gate	Digital oscillator and control	Reduce the power consumption; simplify the system architecture
Power amplifier with a high power level	Class AB	Class D	Increase the power efficiency; reduce the idle power
Power multiplexing	Quarter wavelength RF switch	PIN diode RF switch	Greatly shrink the size
Power matching for LNA	50Ω input impedance	Infinite input impedance	Result in better NF
RFI mitigation	Digital adaptive filtering	Analog adaptive filtering	Simplify the system architecture; improve the detection resolution
Analog signal processing chain circuit implementation	Discrete off-the-shelf components	Customized IC	Enhance the noise immunity of the system; greatly shrink the hardware size and cost
Digital processing unit	PC	DSP	Reduce the system size and the power consumption

circuit blocks are significantly mitigated. Therefore, the detection performance is enhanced due to the improvement of noise immunity. Second, the size and cost for the hardware setup is considerably reduced. It is an important advance for the portable detection systems.

According to the preceding discussion, the improvements that are made by the proposed system compared to the existing solutions are summarized in Table 3.1.

3.4 Conclusion

The general system design requirements for NQR explosive detection systems are reviewed and summarized in this chapter. An NQR detection system usually consists of an NQR probe, a transmitter section and a receiver section. The design concerns and commonly used methods for each section are discussed. The traditional NQR detection systems and their limitations are also briefly reviewed. To address those limitations, we propose a portable NQR explosive NQR detection system solution, wherein a customized mixed-signal IC is designed and fabricated for the analog signal chain and logic control. Comparing our solution with the existing ones item by item, our solution makes significant improvement in every aspect of the design requirements.

Chapter 4

Novel Class-D Voltage-Switching Power Amplification Scheme for NQR and NMR Systems

Through the discussion of general requirements for NQR systems in Chapter 3, we can see that a power amplifier (PA) is indispensable for amplifying the stimulus RF signal to induce the required oscillating magnetic field $\mathbf{B}_1$ in the NQR coil. In this chapter, we will describe the power amplification scheme we employ in the proposed system in detail. Although this power amplifying scheme is proposed for our NQR detection system, it is also applicable for NMR systems. From the perspective of the transmitter section, NMR and NQR detection systems are identical in terms of functionality and working principles. Therefore, we will address both NMR and NQR systems when we explain the proposed power amlifying scheme. In order not to lose generality, the coil and the probe are referred to as the RF coil and the RF probe, respectively, to suit both systems.

Most of the current NMR/NQR systems utilize analog PAs, such as class-A and Class-AB amplifiers, because of their mature design techniques, relatively simple control schemes, and

large operational frequency ranges [43, 84]. However, the large volume and inherently low power efficiency of this type of PAs are prohibitive for realizing portable and field applicable NMR and NQR instruments. To address this problem, this work presents a novel class-D based voltage-switching power amplification scheme suitable for being implemented in NMR/NQR systems [83]. In addition, in Section 3.1.1, we explained why fast-start and fast-stop functions are important for the transmitter section. In this design, the mechanisms for fast-start and fast-stop functions are also incorporated.

In the rest of this chapter, first, general PA design requirements for NMR/NQR systems and limitations of existing designs are explored. Second, a detailed analysis of the architecture of the proposed power amplification scheme is described. Then, the PA circuit implementation for the proposed scheme is presented. Test results show the success of the implemented circuits. Finally, a conclusion is drawn to end this chapter.

4.1 General PA Design Requirements for NMR/NQR Systems

Fig. 4.1 illustrates the RF pulse sequence (ideal and realistic) and a series LC tank RF probe (L, R_{coil} and C) used in NMR/NQR systems, wherein τ_i represents pulse widths. $\mathbf{B}_1$ is generated by driving a high RF pulse current signal into the RF coil. As the sample material, which is usually not conductive, only absorbs a very small amount of RF power and causes negligible effect on the RF probe during the transmitting period, it can be modeled as a small resistor, R_{sample}, in series with the RF coil. An ideal RF stimulus signal consists of a set of RF pulses to form a certain patterned sequence either to fulfill a specific measurement, such as spin-lattice relaxation time (T_1), spin-spin relaxation time (T_2), and so forth; or to enhance the SNR of the emitting signal. The pulse width of the RF pulses varies from a few

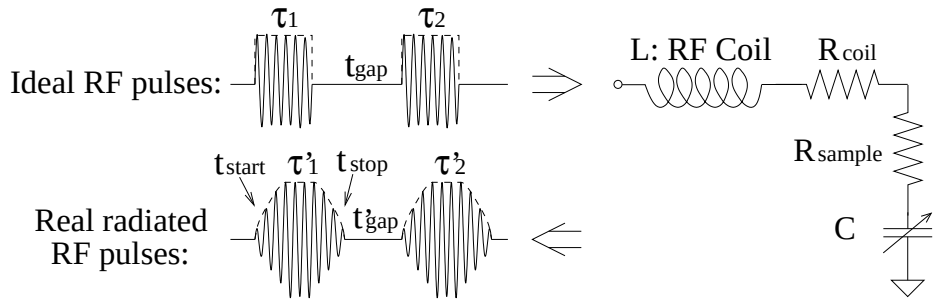

Figure 4.1: The RF pulse sequence and RF probe.

microseconds to hundreds of microseconds, depending on the frequency of $\mathbf{B}_1$ and the flip angle intended to be achieved for the nucleus spins [70]. The time gap between two pulses, t_{gap}, which usually ranges from a few milliseconds to a few seconds, is the receiving period during which the return signal can be detected.

While an RF probe is composed of an RF coil and several resonant capacitors to form a series or parallel LC tank, RF coils have variant types in different applications. For the laboratory equipment, solenoids are often employed. For MRI machines, saddle coils are preferred [85]. For field explosive detection, the spiral planar inductors are commonly used [43]. The Q factor of the RF probe is normally a high value (≥ 30) in order to achieve narrow band power transmission. If one RF probe is used for both transmitting and receiving, Q needs to be even higher ($80 \leq Q \leq 200$) [26]. It is well known that t_{start}, which is the time length of starting the oscillation from initial zero state to a steady value in an LC tank with a constant driving voltage or current, is proportional to the Q factor of the LC tank, as is the time length for the oscillations to die, t_{stop}. Therefore, due to the high Q factor of the RF probe, the real RF stimulus signal radiated by the probe is not a square shaped pulse sequence.

As shown in Fig. 4.1, because of t_{start} and t_{stop}, the pulse width and the time gap of the real radiated RF signal are shortened to τ_i' and t_{gap}'. Since the control of the flip angle by

changing τ_i is based on the assumption that the RF pulse signal has constant amplitude, long t_{start} can significantly affect the precision of this design parameter. Compared to t_{start}, t_{stop} has much more critical impact on the experimental results. As the return signal is always collected right after the RF pulse, the residual oscillating stimulus signal, caused by t_{stop}, becomes interference for the return RF signal. Consequently, the experimental results can be severely corrupted by long t_{stop}.

One method that helps to reduce t_{start} is to drive the RF probe with a higher power signal at the beginning of each RF pulse. When the power reaches the intended level, the amplitude of the driving signal is then lowered to maintain this power level for NMR/NQR detection. This method is called *fast-start shaping*. The mechanism of fast-start shaping can be explained by using Fig. 4.2. If the current driven into the RF coil is denoted as I_{coil}, the ramping-up time of I_{coil} is inversely proportional to the amplitude of the driving signal. Thus, if the driving signal is shaped to have higher amplitude at the beginning of the RF pulse, it will result in a shorter t_{start}. Assuming that the desired RF signal amplitude for NMR/NQR detection is A, we raise its amplitude by n times to $A' = n \cdot A$ during the fast-start period T_{set}. The resulting starting time t'_{start} will be equal to t_{start}/n, where t_{start} is the start time without fast-start shaping. t'_{start} is determined by A' and the Q factor of the LC network. Apparently, T_{set} should be tuned to be equal to t'_{start}. If T_{set} is longer than t'_{start}, the resultant I_{coil} will have an overshoot after t'_{start}, as I_{coil} is still ramping up towards the current level determined by A'. If T_{set} is shorter than t'_{start}, the resultant start time will be longer than t'_{start}.

Q-damping is a technique that has been widely used for fulfilling fast-stop shaping. The idea is to lower the Q factor of the LC tank by adding extra resistance in series with the RF coil at the end of each RF pulse. As a result, the residual power remaining inside the LC tank will dissipate faster.

Based on the above discussion, we identify the key design requirements on the PA section

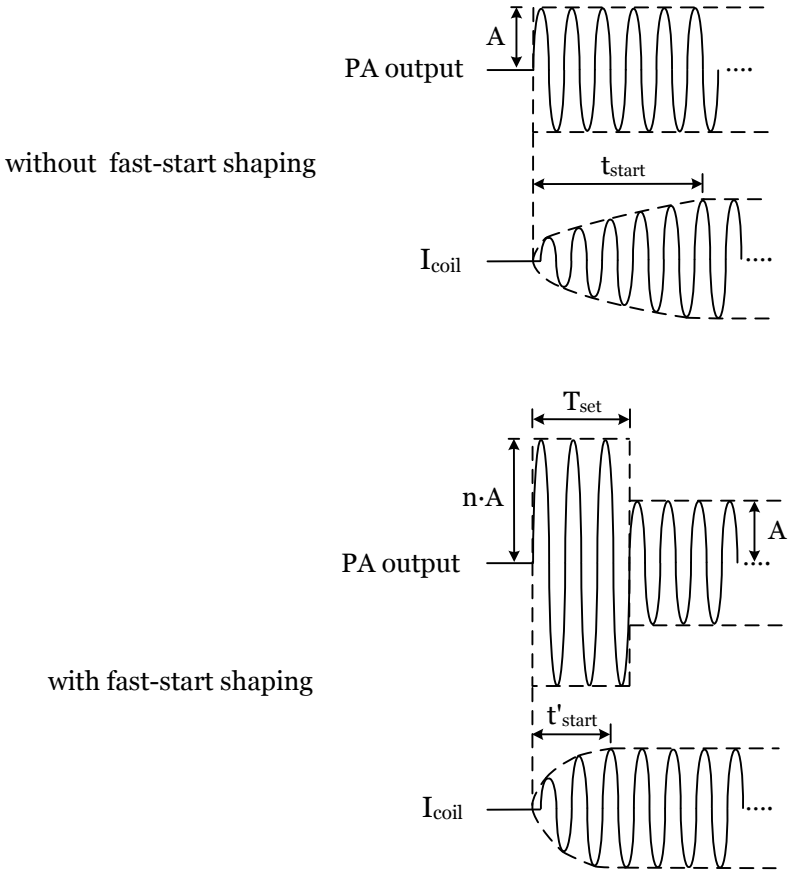

Figure 4.2: Comparison of t_{start} with and without fast-start shaping

of NMR/NQR systems as follows.

- Fast-start (short t_{start}): The PA must have high instantaneous power driving capability at the start of each RF pulse.
- Fast-stop (short t_{stop}): The PA must stop the residual oscillating power very quickly at the end of each RF pulse.
- High power efficiency: This quality is appreciated by all types of system applications, especially for portable systems.

4.2 Performance of Conventional PAs Used in NMR/NQR Systems

An example of a widely used analog PA is shown in Fig. 4.3. It includes a simplified class-AB PA with a parallel LC matched RF probe. C_1 and C_2 in Fig. 4.3 constitute a power matching network combined with the RF coil to match the PA's output impedance (Z_{out}, normally resistive only) at a certain operating frequency, such that the maximum power transfer can be achieved. S_1 and R_{damp} form a Q-damping circuit to fulfill fast-stop shaping [26]. During the transmitting period, S_1 is closed to short R_{damp} in order to make the Q factor of the RF probe higher. Right after an RF pulse stops, S_1 is opened so that the energy stored in the RF probe can dissipate on R_{damp}. If the same RF probe is used for detection, during the receiving period, S_1 is closed again to enhance the Q factor.

We can investigate this example to discover the drawbacks of using conventional analog PAs in NMR/NQR systems according to the aforementioned key design requirements.

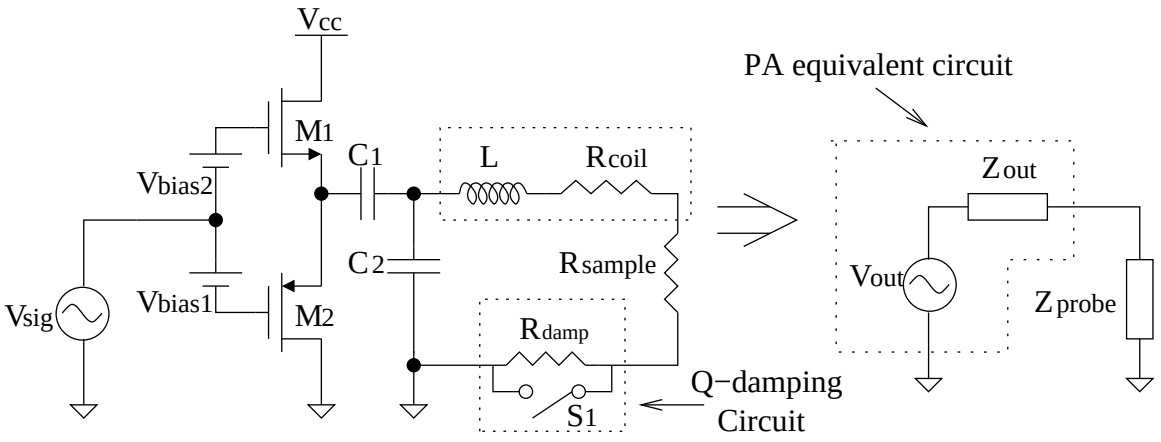

Figure 4.3: A class-AB type PA with a parallel LC matched RF probe and the equivalent circuit.

Firstly, the conventional analog PAs do not have a dedicated circuit design for enforcing the fast-start function. As discussed in Chapter 3, the traditional NQR systems use an RF oscillator as a signal source and generate the on-off keyed RF pulses by gating the RF signal. Then, the generated RF pulses are fed into an analog PA for amplification. However, the fast-start function and high power efficiency can not be achieved at the same time in analog PAs. To realize fast-start, the output voltage amplitude of the PA (A' in Fig. 4.2) during T_{set} must be higher than the output voltage amplitude afterwards (A in Fig. 4.2). As a result, with constant V_{CC}, the power efficiency becomes lower after T_{set} since the power efficiency is proportional to the output amplitude. Secondly, the theoretical highest power efficiency that class-AB PAs can reach is 78.5% in the full-swing mode [86]. In practical applications, the power efficiency is significantly lower than 78.5%. This is due to the fact that at least one voltage gain stage, which consumes a certain amount of power, is required to enhance the signal scale to drive the class-AB PA. In addition, as M_1 and M_2 require voltage headroom to work in the linear range, the full-swing mode can never be reached, which further degrades the power efficiency.

4.3 Novel Class-D Voltage-Switching Power Amplification Scheme

A class-D voltage-switching PA collaborating with a series LC tank RF probe is proposed to address the NMR/NQR power section design requirements. The reason for choosing the class-D voltage-switching PA scheme over other PAs is that the circuit setup for a voltage-switching PA is simpler, compared to a current-switching PA which requires a current source. A series LC tank RF probe can be used in conjunction with the voltage-switching PA to generate narrow band sinusoidal signals.

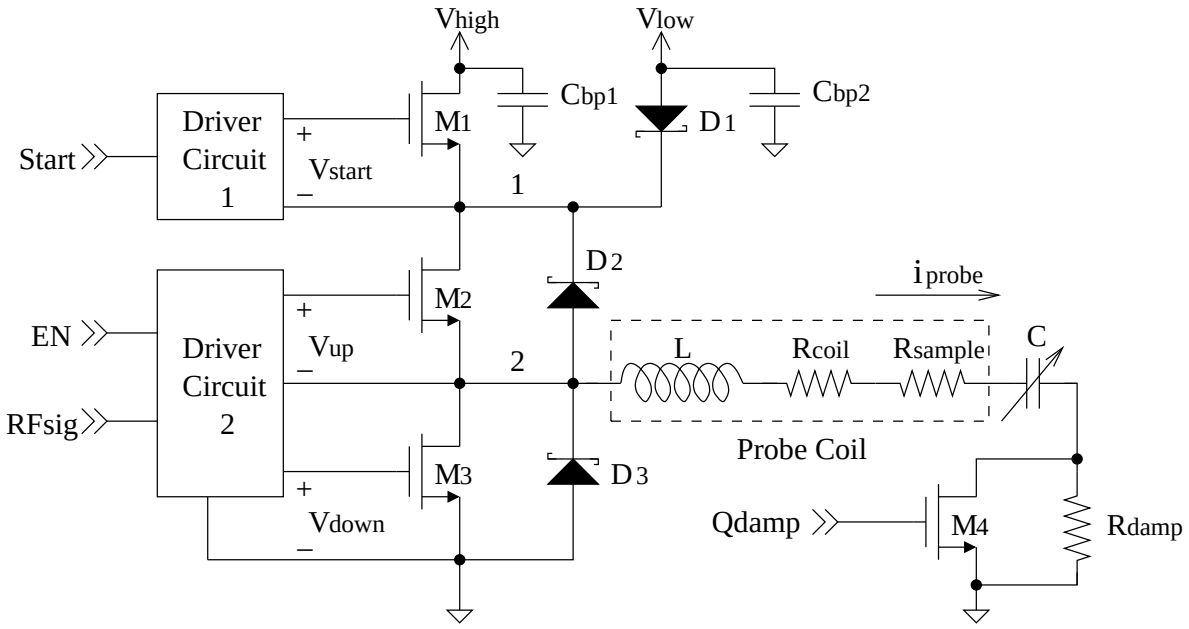

Figure 4.4: Class D voltage-switching PA with additional fast-start and fast-stop function.

Fig. 4.4 shows the circuit of the proposed power amplification scheme. MOSFETs M_2 and M_3 combining with diodes D_2 and D_3 are configured as two bidirectional switches. Schottky diodes are used for D_2 and D_3 because they have a smaller reverse recovery time that can greatly reduce the switching transition loss [89]. These two switches are turned on and off alternately with 50% duty cycle. If the frequency of the gate control signals, V_{up} and V_{down}, is equal to the RF probe's resonant frequency f_o, a square wave voltage signal with a frequency f_o is generated at Node 2. Then, the series LC RF probe functions as a resonant filter by which only the fundamental frequency component of the square wave is delivered into the RF coil. As a result, an oscillating magnetic field at the resonant frequency f_o is induced in the RF coil. By turning on or off M_1, the supply voltage, V_1, can be switched to realize the fast-start function. The Q-damping circuit, M_4 in parallel with R_{damp}, is similar to the one used in the analog PA structure. C_{bp1} and C_{bp2} are the bypass capacitors for the two power supplies V_{high} and V_{low}, respectively.

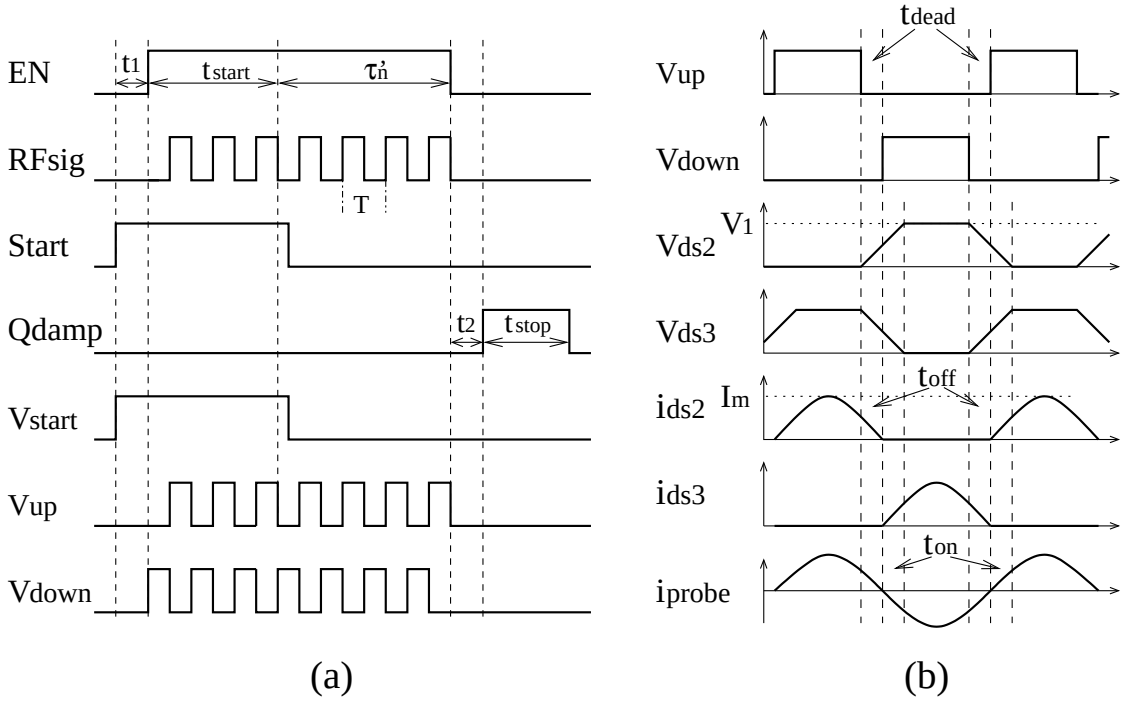

Figure 4.5: (a) Control signals and gate driving signals of the proposed PA circuit. (b) V_{gs}, V_{ds} and i_{ds} of M_2 and M_3 when $f = f_o$ and $t_{on} = t_{off} = t_{dead}$.

The control signals and the MOSFET driving signals are shown in Fig. 4.5 (a). EN is the enable control of the class-D PA. $RFsig$ is the signal at a frequency that can be precisely adjusted to f_o. As far as only the PA is concerned, $RFsig$ can be enabled all the time. However, since the strength of the received NMR/NQR signal is inherently weak, $RFsig$ must be disabled during the receiving period to avoid interference. EN and $RFsig$ are fed into Driver Circuit 2 (Fig. 4.4) to generate the gate driving signals V_{up} and V_{down}, which are non-overlapping with sufficient dead time t_{dead} for turning on M_2 and M_3 alternately and avoiding shoot-through of M_2 and M_3. The length of t_{dead} is mainly determined by the turn-off time t_{off} of M_2 and M_3. $Start$ is the control signal for switching between the higher voltage power supply V_{high} and the normal power supply V_{low}. Its level is shifted by Driver Circuit 1 to form V_{start} for turning on and off M_1. The $Qdamp$ signal is directly coupled to

M_4 for damping the energy to R_{damp} after each RF pulse.

4.3.1 Power Efficiency of the Proposed PA Circuit

The most significant benefit of using switched-mode PAs is the improvement of the power efficiency. For the proposed PA circuit, Fig. 4.5 (b) illustrates the gate-source voltages, drain-source voltages and drain-source currents when $f = f_o$ and $t_{on} = t_{off} = t_{dead}$. The square wave voltage on Node 2 (V_2) has the maximum value equal to V_1, which is approximately $V_{low} - V_d$ under steady state conditions, where V_d is the voltage drop of D_1 in Fig. 4.4. Only the fundamental component of V_2 will pass the series LC tank and be effective on the total resistance R_{total}, which is given by

$$R_{total} = R_{coil} + R_{sample} + R_{on4} + R_{on2,3} \tag{4.1}$$

where R_{on4} is the on-state resistance of M_4, and $R_{on2,3}$ is the on-state resistance of M_2 and M_3. The fundamental component of V_2 has the RMS value as:

$$V_{fund2} = \frac{\sqrt{2}V_1}{\pi} \tag{4.2}$$

The RMS current through the probe, i_{probe}, can be obtained by dividing V_{fund2} by R_{total}.

$$i_{probe} = \frac{\sqrt{2}V_1}{\pi R_{total}} \tag{4.3}$$

Then, the power delivered to the series RF probe, which is considered as the "load" in this case, is:

$$P_{load} = i_{probe}^2 \left(R_{coil} + R_{sample} + R_{on4}\right) \tag{4.4}$$

The power losses of the circuit in steady-state operation come from three main sources. They are the conduction power loss of M_2 and M_3, $P_{conloss}$, the loss in the gate driving circuits, $P_{gateloss}$, and the loss in the Schottky diode D_1, P_{dloss}. A fourth source of loss is the switching losses in the MOSFETs which is incurred during switching events when the voltage across and the current through the MOSFET are both large. However, in the case where $f = f_o$, the current through the MOSFETs when they are switching is naturally zero, so this loss is small and will be neglected [87]. A summary of the losses is listed in Table 4.1.

Table 4.1: Major power losses in the circuit.

Loss	**Equation**
$P_{conloss}$	$i_{probe}^2 R_{on2,3}$
P_{dloss}	$i_{probe} V_d$
$P_{gateloss}$	$2Q_g V_g f$

Q_g is the gate charge of M_2 and M_3
V_g is the voltage of the gate drive circuits

Finally, the power efficiency η is:

$$\eta = \frac{P_{load}}{P_{load} + P_{conloss} + P_{gateloss} + P_{dloss}} \tag{4.5}$$

The following observations of the proposed PA circuit can be made based on the above discussion.

1) The power amplification level (the amplitude of i_{probe}) can be controlled by adjusting the power supply voltage V_1.

2) The output impedance of the PA is mainly determined by R_{on} of M_2 and M_3. For today's devices, R_{on} can be as low as tens of a $m\Omega$, which is significantly lower than

the inherent resistance of the probe. Therefore, for most of the NMR and NQR probes, the matching network can be greatly simplified to just a resonant capacitor.

3) In order to achieve high η, both $P_{conloss}$ and $P_{gateloss}$ should be reduced. However, $P_{conloss}$ is proportional to R_{on}. MOSFETs with small R_{on} often have large Q_g, which leads to a higher $P_{gateloss}$. In NMR/NQR systems, high power RF signals require big MOSFETs with large Q_g to bear high voltage, V_1, and high current, i_{probe}. Therefore, $P_{gateloss}$ is the dominant factor for the power efficiency of the proposed PA circuit.

4.3.2 Fast-Start and Fast-Stop Configuration

Unlike the analog PAs, the bias condition is no longer required for active devices in the switched-mode PAs because they are operating in the nonlinear range. Hence, increasing the power supply voltage does not affect the MOSFETs operating condition. On the other hand, the amplitude of V_2 is equal to the power supply voltage V_1. Therefore, we can use the power supply switching method to fulfill fast-start shaping. If the steady-state $\mathbf{B}_1$ requires the power supply to be V_{low}, we use a higher voltage, V_{high}, at the beginning of each RF pulse. Once $\mathbf{B}_1$ reaches the desired value, the power supply is switched back to V_{low}. Theoretically, higher V_{high} leads to a shorter t_{start}. However, due to the limitations of the devices such as the maximum V_{DS} tolerance, the maximum value that V_{high} can attain will be limited in circuit implementations.

The fast-stop scheme of the proposed PA circuit is partially similar to the one used in the analog PA. The difference is that the power supply switch circuit is reused to absorb the major portion of the oscillation power at the end of each RF pulse in our design. M_4 is not turned off right after EN is disabled. A time interval t_2 is introduced, during which, M_2 and M_3 are turned off by the EN signal while M_4 remains on. Fig. 4.6 shows the equivalent circuit of the PA in fast-stop working mode. Since M_1, M_2 and M_3 are off, they

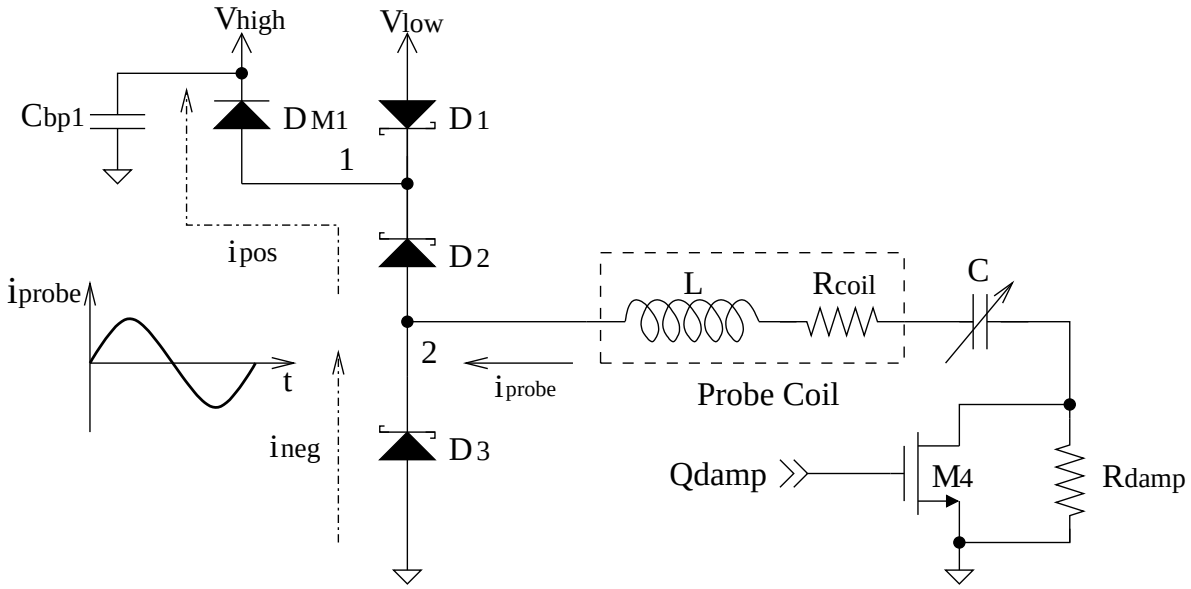

Figure 4.6: Equivalent circuit of the fast-stop mode.

are not included in this discussion. D_{M1} is the intrinsic diode of M_1. The current direction is defined as from the RF coil to Node 2. C_{bp1} is the bypass capacitor for V_{high} voltage power supply. During the time when $i_{probe} > 0$, D_{M1} and D_2 conduct the positive current i_{pos} from the probe back to C_{bp1}. Thus, most energy stored in the probe is pushed back into C_{bp1} for future use. When $i_{probe} < 0$, D_3 conducts the negative current from ground to the probe. After several cycles of i_{probe}, M_4 can be turned off so that the residual energy in the probe can be absorbed by R_{damp}. Despite of the fast decay speed that is provided by D_{M1} and D_2 at the beginning of the damping period, R_{damp} is essential for the fast-stop operation. Before the receiving cycle, the residual energy has to be rapidly dissipated to an extremely low level that is comparable to the return signal.

The advantages of this configuration are summarized as follows:

1) Through the path constructed by D_{M1} and D_2, most energy stored in the probe can be dumped to C_{bp1}. Compared to the regular Q-damping fast-stop methods, the proposed

circuit provides much shorter t_{stop}.

2) Since the energy is pushed back to the power supply, the power efficiency of the circuit is further improved.

In addition, the higher V_{high} leads to a larger pushed-back energy per cycle with the same amplitude of i_{probe} and the same cycle length T, considering that $E = P \cdot T = V_{high} \cdot i_{probe} \cdot T$. Therefore, similar to fast-start, fast-stop also requires high V_{high} voltage.

4.4 Circuit Implementation for the Proposed Power Amplification Scheme

4.4.1 Considerations and Issues of Implementation

The operating frequency and output power scale are the two most important specifications for the design of a PA in NMR and NQR systems. To achieve these specifications, two important issues need to be addressed when the proposed power amplification scheme is considered for implementation in such systems. First, suitable components need to be chosen for the MOSFETs: M_1, M_2, M_3, and M_4. Among the four MOSFETs, M_2 and M_3 are more critical as they are alternately and repeatedly switched on and off during the whole excitation period. Second, each of the MOSFETs should be equipped with a compatible driving circuit.

Generally, there are three important criteria for choosing the suitable MOSFETs for a circuit: the maximum bearable drain-source voltage (V_{dsmax}), the maximum DC drain-source current during on-state (I_{dsmax}), and the on-state resistance (R_{on}). For the implementation of the power amplification scheme, these criteria are mainly determined by the required max output power $max(P_{out})$ for a specific probe setup. For a given RF probe, the maximum output power $max(P_{out})$ that can be delivered to the load relies on $max(V_{low})$ and the ratio

of R_{coil} to $R_{on4} + R_{on2,3}$, with the assumption that R_{sample} is negligible compared to R_{coil}.

$$\begin{aligned} max(P_{out}) &= max(V_{low}) \cdot max(i_{rms,probe}) = max(i_{rms,probe})^2 \cdot R_{coil} \\ &= \left(\frac{max(V_{low})}{R_{coil} + R_{on4} + R_{on2,3}} \right)^2 \cdot R_{coil} \\ &= \left(\frac{max(V_{low})}{1 + \frac{R_{on4}+R_{on2,3}}{R_{coil}}} \right)^2 \cdot \frac{1}{R_{coil}} \end{aligned} \tag{4.6}$$

As $M2$ and $M3$ only conduct half cycle of i_{probe}, I_{dsmax} must be larger than $2 \cdot max(i_{rms,probe})$. Based on Eq. (4.6), to achieve a high maximum output power level for a given $max(V_{low})$, $R_{on2,3}$ and R_{on4} should be minimized. It can also be seen from the PA efficiency's perspective. According to Eq. (4.5), reducing the conduction loss, $P_{conloss}$, which is determined by $R_{on2,3}$, can increase η of the PA. In real design, $R_{on2,3}$ and R_{on4} are chosen such that $R_{on2,3} + R_{on4} \ll R_{coil}$. In fact, since M_4 is switched much less frequently than M_2 and M_3, and R_{on} is inversely proportional to $P_{gateloss}$, R_{on4} is usually chosen to have a much smaller value than $R_{on2,3}$. On the other hand, by knowing $max(V_{low})$ and corresponding t_{start}, the value of $max(V_{high}) = n \cdot max(V_{low})$ can be found, where n is the scale factor depending on the length of t_{start}. Now, to choose proper MOSFETs for M_2 and M_3, the three criteria can be summarized as:

$$V_{dsmax} \geq max(V_{high}) \tag{4.7}$$

$$I_{dsmax} \geq 2 \cdot max(i_{probe}) = \sqrt{max(P_{out})/R_{coil}} \tag{4.8}$$

$$R_{on} < \frac{R_{coil}}{10} \tag{4.9}$$

Similar principles are applicable to decide the specifications for M_1 and M_4. For M_1, V_{dsmax} and i_{dsmax} are the same with those of M_2 and M_3. However, R_{on} for M_1 is not equally critical. This specification can be relaxed if it is necessary for the sake of cost. For M_4,

i_{dsmax} and R_{on} are determined by using Eq. (4.8) and Eq. (4.9). V_{dsmax} also can be relaxed.

After the MOSFETs are decided, the driving circuits can be designed accordingly. As M_2 and M_3 are switched on and off at the NMR/NQR resonant frequency, the drivers for these two devices should be elaborately configured to reach the desired operating frequency. The frequency of the PA is mainly constrained by the turn-on time of M_2 and M_3. As mentioned before, devices that are able to bear large output power usually have fairly large Q_g. Therefore, the driving circuit must provide a large instant driving current to achieve short turn-on time. On the contrary, M_1 and M_4 are only toggled once or twice for each RF pulse. As a result, the driving speed for these two drivers is designed comparatively slow to save power consumption and cost.

4.4.2 Class-D PA Design for the Portable NQR Detection System

Today's advanced semiconductor technologies provide a variety of power devices and compatible driver circuit schemes so that the proposed power amplification scheme can be implemented. For the NQR explosive detector system in this work, the possible maximum output power is designed to be capable of supporting 1 kW. Considering that the explosive materials have the NQR signal frequency range from $0.5-6$ MHz, the maximum operating frequency of the PA is $10MHz$. The simplified schematic for the class-D type PA circuit is shown in Fig. 4.7.

In Fig. 4.7, we can see that NMOS devices are used for M_1, M_2, M_3, and M_4. The reason is that NMOS has better conductivity with a similar gate area compared to PMOS (usually 3 times higher). Moreover, Q_g is proportional to the gate area. Hence, with the same gate driving loss $P_{gateloss}$, NMOS will have less conduction loss $P_{conloss}$. For high power class-D PAs, NMOS devices are often used to realize both high-side and low-side switches

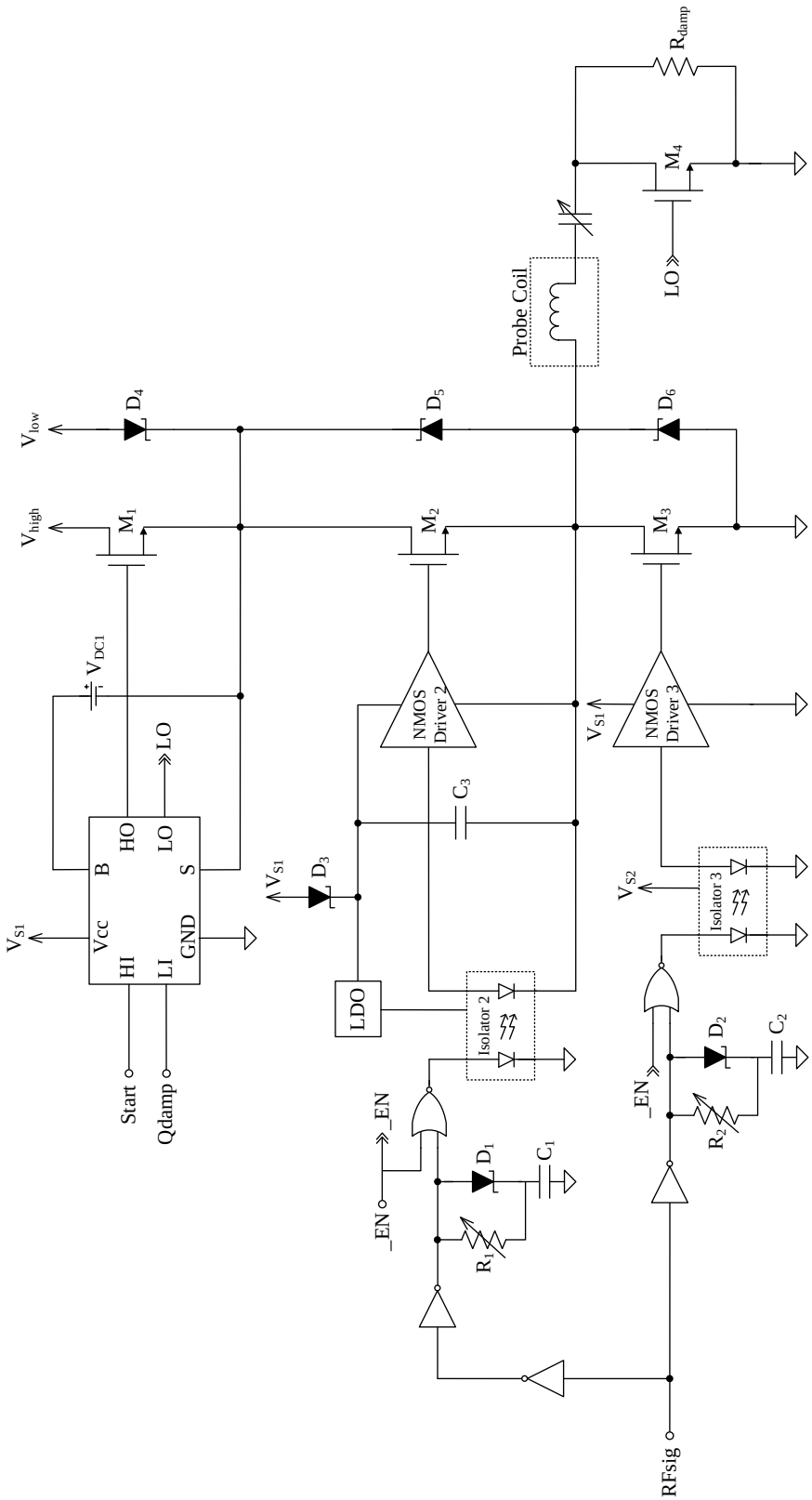

Figure 4.7: Driver circuit for the Class D PA

[88]. The drawback of using NMOS as the high-side switch is that a floating driver circuit is needed to turn on and off the NMOS. The MOSFETs that are selected for M_2 and M_3 have $V_{dsmax} = 100V$, $I_{dsmax} = 20A$ ($i_{dsmax} = 80A$), and $R_{on} = 50m\Omega$. Actually, the specification I_{dsmax} for the MOSFETs is the maximum DC current it can carry, and i_{dsmax} is the maximum pulse current which has the duration less than $10us$. In other words, i_{dsmax} can be interpreted as the peak current value that the MOSFETs can bear. Therefore, in addition to the criterion shown in Eq. (4.8), the peak value of i_{probe} must be less than i_{dsmax}. As each of M_2 and M_3 only conducts the i_{probe} for half of the cycle, the selected MOSFETs can support i_{probe} up to $40A$ RMS. The peak value of $40A$ RMS i_{probe} is approximately $56A$, which is less than $80A$ i_{dsmax} of the MOSFET specification. With the chosen MOSFET, we can see that the possible maximum output power is $max(P_{out}) = 2 \cdot max(V_{dsmax}) \cdot max(I_{dsmax}) = 4kW$. A MOSFET with $V_{dsmax} = 100V$, $I_{dsmax} = 75A$, and $R_{on} = 10m\Omega$ is used to function as M_1 and M_4.

To initiate the driving circuits design for M_1, M_2, M_3, and M_4, Q_g and the maximum operating frequency need to be considered. For M_2 and M_3, Q_g is equal to $12nC$. As the maximum operating frequency is $f_{max} = 10MHz$, the minimum period is $T_{min} = 100ns$. In each cycle, each of M_2 and M_3 will be turned on and off once. In total, 4 switching actions will be executed. The transition time for turning on and off are assumed to be equal, which is denoted as t_{on}. In addition, a dead time t_{dead}, as shown in Fig. 4.5, happens twice in each cycle: the one between turning off M_2 and turning on M_3; the other between turning off M_3 and tuning on M_2. Firstly, in order to ensure that the class-D PA can generate a signal at the frequency of $10MHz$, $4 \cdot t_{on} + 2 \cdot t_{dead}$ has to be less than the minimum period T_{min}. Secondly, revising the statement claimed in Section 4.3.1, the switching loss cannot be ignored unless t_{on} and t_{dead} is a small portion of cycle time length even though the probe current is naturally zero at the transition point between M_2 and M_3. In other words, if t_{on} and t_{dead} is so long that the switching loss becomes noticeable, the power efficiency of

the PA will be compromised. Therefore, t_{on} and t_{dead} should be minimized such that power efficiency can be improved. However, as the shoot-through between M_2 and M_3 may damage the devices, t_{dead} needs to remain in a reasonable range to definitely avoid the occurrence of the shoot-through. Consequently, minimizing t_{on} is the goal for designing the driving circuit. Ideally, t_{on} can be computed by

$$t_{on} = \frac{Q_g}{I_{drv}} \tag{4.10}$$

where I_{drv} is the driving current from the MOSFET driver circuit. In this design, an NMOS driver IC with a $9A$ peak driving current is adopted to drive M_2 and M_3. Theoretically, according to Eq. (4.10), the resultant t_{on} should be around $1.4ns$. With the losses caused by parasitic effect and PCB layout, the measured t_{on} is $3ns$.

As opposed to M_2 and M_3, M_1 and M_4 do not demand fast switching capability from the driving circuit. To have low R_{on} and high V_{dsmax}, Q_g for M_1 and M_4 is $76nC$. In this design, an off-the-shelf half bridge driving IC is used to collaborate with the two MOSFETs. The driving current of this circuit is $2A$, which leads to $t_{on1,4} \simeq 40ns$.

Due to the varying source voltage of M_2, denoted as V_{M2S}, the driving circuit for M_2 needs be tailored to work floatingly on the basis of V_{M2S}. In Fig. 4.7, C_3, D_3, $Isolator$ 2 and $NMOS\ Driver$ 2 form the circuit to fulfill the floating driving function for M_2. When M_3 is on, the source voltage of M_2, V_{M2S} is pulled down to ground. D_3 is turned on to charge C_3 to the voltage V_{S1}. Then, after M_3 is turned off, C_3 will hold the voltage for $NMOS\ Driver$ 2 to turn on M_2. V_{M2S} is pulled up to either V_{high} or V_{low} depending on the state of M_1. D_3 is then reverse biased as the voltage on it cathode is $V_{S2} + V_{M2S}$, which is higher than V_{S2}. Note that since V_{M2S} can be as high as $max(V_{high})$, D_3 needs to have the reverse break-down voltage specification that is greater than $max(V_{high})$, which is $100V$ in this design. $Isolator$ 2 is used to level-shift the control signal from the low power domain to the floating basis domain. It should be noted that $Isolator$ 3 is not required for the

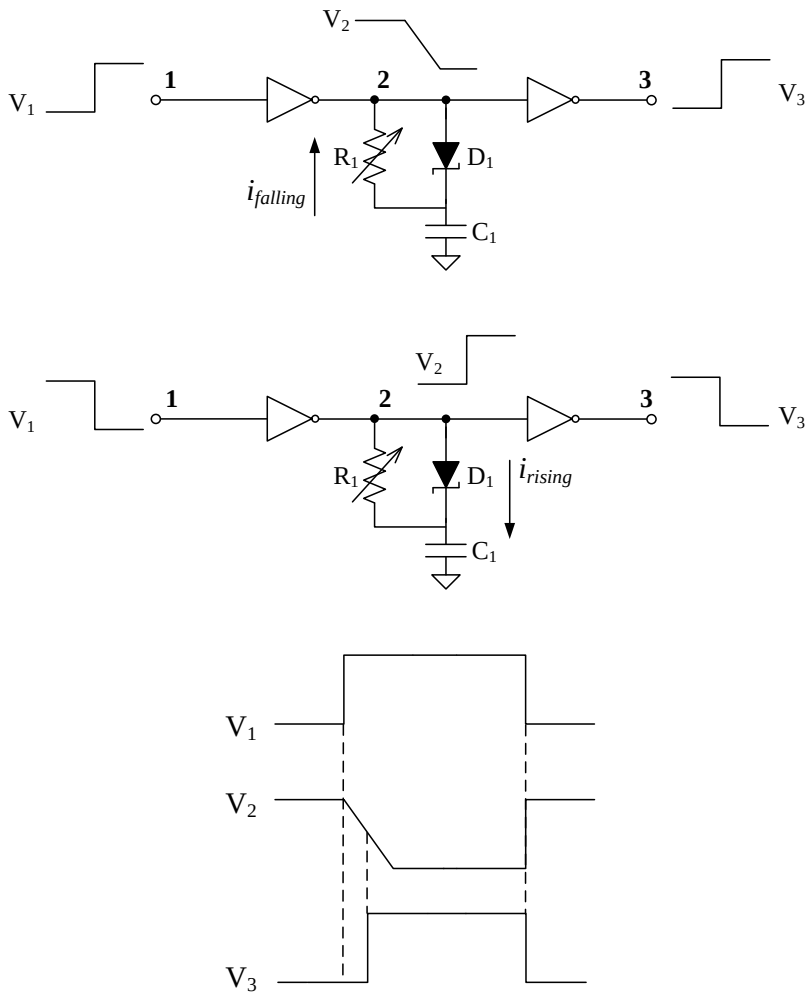

Figure 4.8: The working mechanism of the falling edge delay circuit

low-side driver circuit. The reason of adding it is to introduce the same gate delay to both driving circuits for M_2 and M_3, such that t_{dead} is stable enough to prevent the shoot-through between M_2 and M_3.

The dead time t_{dead} is generated by a one-side edge delay circuit constructed of R_1, D_1 and C_1. The working mechanism of the circuit can be depicted by Fig. 4.8. When V_1 is rising, the output voltage of the first inverter, V_2, is on the falling edge. C_1 is being discharged by the inverter. As the current i is flowing from C_1 to ground, D_1 is reverse

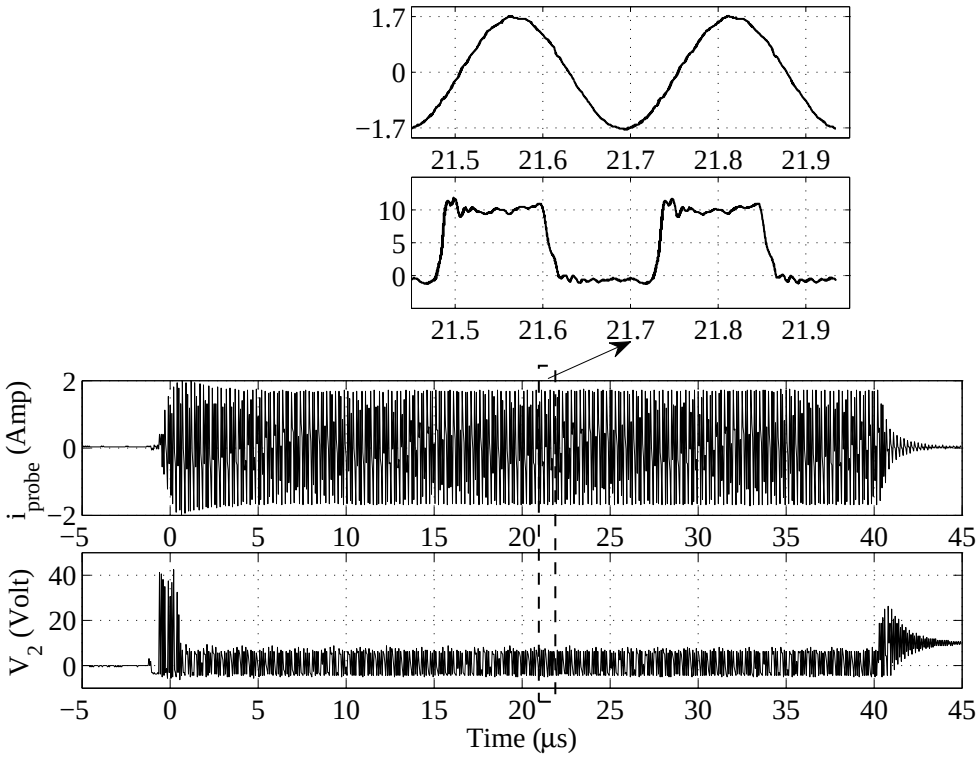

Figure 4.9: i_{probe} and V_2 when $V_{high} = 40V$ and $V_{low} = 10V$.

biased so that R will conduct i. Then, the RC network slows down the falling edge of V_2. With the regulation of the second inverter, the rising edge of V_3 is delayed compared to V_1. On the contrary, during the falling edge of V_1, D_1 is turned on so that charging C_1 is finished instantly. As a result, if D_1 is assumed to be an ideal diode, which has 0 forward bias voltage and 0 on-state resistance, only one edge of the toggling signal, V_1, is delayed. Obviously, delay time is determined by the value of R_1 and C_1. Therefore, a variable R_1 can be tuned to control the delay time given a fixed C_1 value.

4.5 Test Results

The proposed PA circuit is implemented as a part of the transmitter board, which will be shown in Chapter 9. In this section, the detailed evaluation results specifically for the Class-

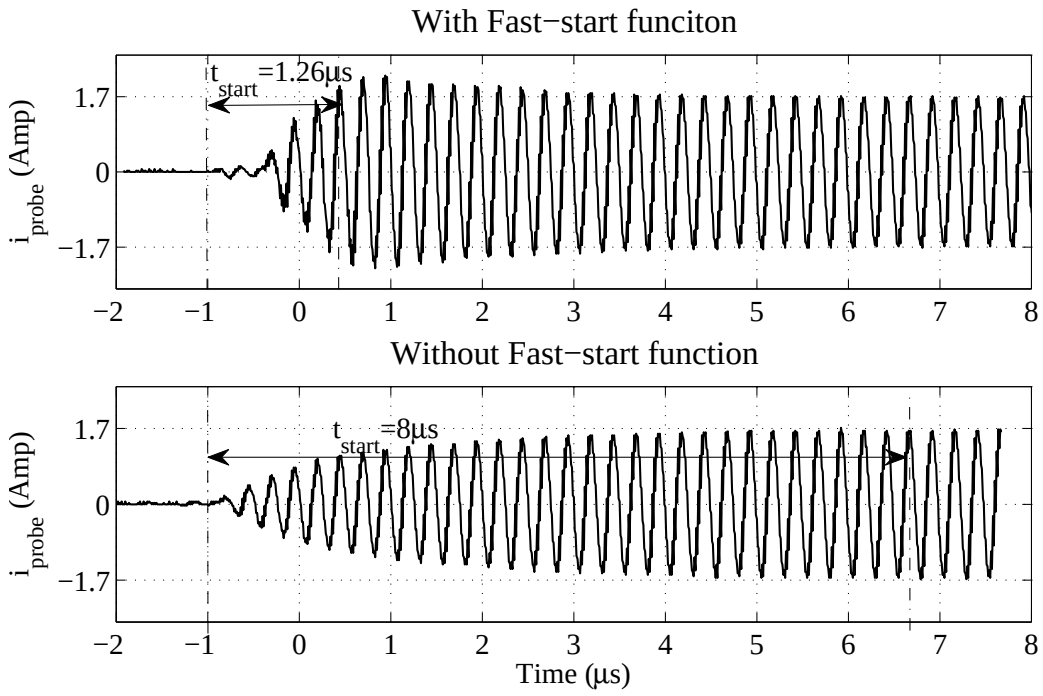

Figure 4.10: t_{start} with and without fast-start function.

D PA is presented. An RF coil which has $L = 2.9\mu H$ and $R_{coil} = 3.5\Omega$ ($Q = 20.9$) is used for the tests. The reason for choosing a low Q coil is that the current probe for measuring the coil current can introduce large parasitic impedance on the coil. It degrades the efficiency noticeably if R_{coil} is not significantly higher than the parasitic impedance.

Fig. 4.9 shows a measured NQR excitation signal generated by the PA, used in detection of HMTD. The NQR resonant frequency of HMTD f_o is 4.009MHz at room temperature. The pulse width of the excitation signal τ_1 is $41\mu s$. In Fig. 4.9, i_{probe} is the current through the probe, and V_2 is the voltage on Node 2 (Fig. 4.4). With $V_{high} = 40V$ and $V_{low} = 10V$, i_{probe} has an amplitude of $1.7A$ in the steady working state.

Fig. 4.10 shows the comparison of t_{start} with and without fast-start shaping. M_1 in Fig. 4.4 is turned on for $1.5\mu s$ to fulfill the fast-start function, which leads to $t_{start} = 1.26\mu s$. Compared to the startup time without turning on M_1, $t_{start} = 8\mu s$, the improvement is

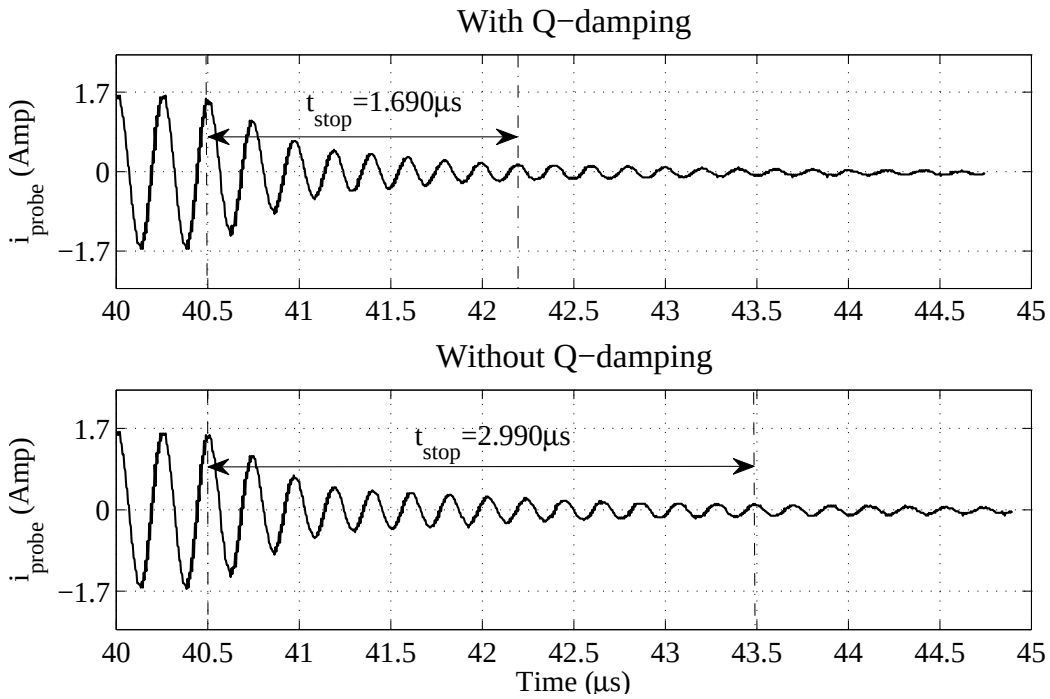

Figure 4.11: t_{stop} with and without Q-damping function.

significant, 80% less.

The comparison results of t_{stop} with and without turning off M_4 (Fig. 4.4) are shown in Fig. 4.11. The improvement on t_{stop} in percentage is relatively large, 43%. Hence, for the rest of damping period, R_{damp} is still necessary to maintain an overall fast-stop function.

Fig. 4.12 shows the current provided by V_{low}, i_{Vlow}, and the current of the power supply of the driver circuit, i_{driver}, during the whole transmitting period τ_1 ($\overline{EN}$ means this control signal is low effective). To find the efficiency of the designed PA, the averaged power of V_{low}, P_{low}, and the averaged power of the power supply for the driver circuit, P_{driver} during the transmitting period is computed and compared with the averaged power delivered to the RF probe (P_{probe}) in one cycle, $T = 1/f = 0.249\mu s$. According to Fig. 4.12, $P_{low} = 5.7317W$ and $P_{driver} = 2.2925W$. According to Fig. 4.9, $P_{probe} = 4.8927W$. Then, the power efficiency $\eta = P_{probe}/(P_{driver} + P_{low}) = 61\%$. In the above discussion, P_{driver} is the dominant factor of

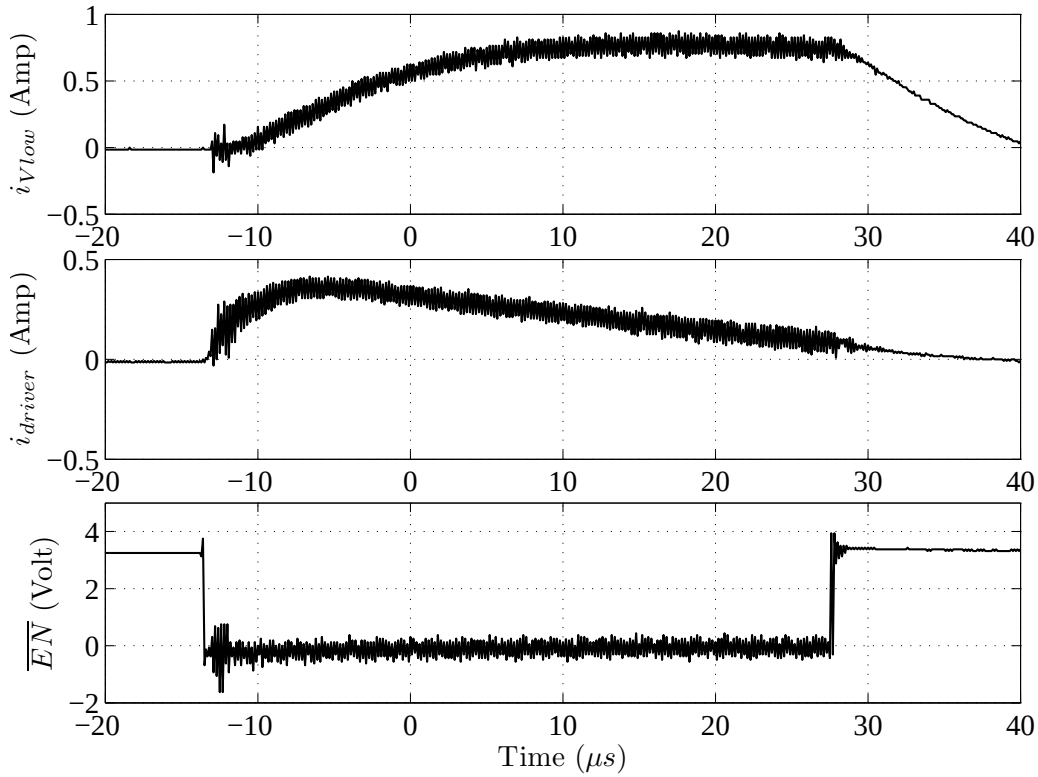

Figure 4.12: i_{Vlow} and i_{driver} during the whole transmitting period.

the power loss. Moreover, P_{driver} is nearly constant for various P_{low} and P_{probe}. Therefore, as V_{low} becomes higher, which indicates that P_{low} and P_{probe} are higher, η will increase.

4.6 Conclusion

A class D voltage-switching PA circuit design with novel fast-start and fast-stop functions has been presented in this chapter. The PA scheme can greatly decrease the power loss as well as the physical size, which makes it a suitable solution for the portable NMR or NQR based detection systems. Test results of the prototype PA show that fast-start and fast-stop functions of excitation signals have been successfully realized within a compact volume while

maintaining high power efficiency. It can be foreseen that with the compact size and high power efficiency, the proposed PA structure will significantly shrink the volume and power consumption of the whole NMR/NQR systems. Therefore, NMR/NQR based low cost field applicable instruments such as mini MRI systems, portable bomb scanners, and landmine detectors can benefit from the techniques presented.

Chapter 5

Power Multiplexing and Matching Mechanism

Inspired by [82], in the proposed NQR detection system, an infinite impedance power matching mechanism is employed in the NQR probe to achieve low noise detection. With this matching method, only one resonant capacitor is required in a parallel LC RF probe for NQR signal detection. Compared to the traditional 50Ω matching method, the infinite impedance matching mechanism not only simplify the hardware configuration of the NQR probe significantly, but also benefit the power multiplexing scheme for the proposed Class-D PA.

During the receiving period, a parallel-LC-tank type of RF probe is used for NQR signal detection. However, during the transmitting period, in order to realize low power operation, a series-LC-tank type of NQR probe is demanded by the proposed Class-D PA circuit. Therefore, a power multiplexing strategy is designed to coordinate the transmitting section and receiving section. In particular, there are two tasks this power multiplexing network needs to accomplish. First, the NQR probe should be switched between the parallel LC tank and series LC tank so that the probe can be shared for transmitting and receiving. Second,

as the receiver circuit is designed to be sensitive to extremely low power NQR signals, it needs to be isolated from the NQR probe during transmitting period to protect it from being damaged by high power signals.

In this chapter, the infinite impedance matching mechanism is presented first. Then, the power multiplexer design is discussed. Specifically, the PIN diode based RF switch, which is the key component of the power multiplexer, is depicted in detail. Finally, a conclusion is drawn based on the discussion presented in this chapter.

5.1 Infinite Impedance Power Matching Scheme

The portable detection systems are in general designed to have minimum but reasonable volume and weight for mobile applications. This requirement still applies in this work. For this purpose, the connecting cable between the NQR probe and the input of the receiver circuit is chosen to be short (less than $1m$ in the proposed system). As NQR frequencies of explosive materials range from $500kHz$ to $6MHz$, the wave lengths of NQR signals (from $50m$ to $600m$) are substantially longer than the scale of the system. Therefore, the lumped circuit model are used to analyze the power matching mechanism.

Among the laboratory NQR systems, standard LNAs with 50Ω input impedance are often employed to provide initial amplification for NQR signals as they are off-the-shelf devices. Accordingly, an NQR coil is often equipped with a matching network which transfers the output impedance of the NQR probe to 50Ω to pair up with the standard LNA's input impedance. A widely used matching network along with the NQR coil is shown in Fig. 5.1 (a). C_1 and C_2 construct a L–section matching network to transfer the NQR probe output impedance for impedance matching. The input impedance of an LNA is denoted as Z_{in}. For standard LNAs, usually $Z_{in} = 50\Omega$. Note that this type of matching network can only be applied when $R < Z_{in}$, where R in Fig. 5.1 (a) represents the DC resistance of the coil.

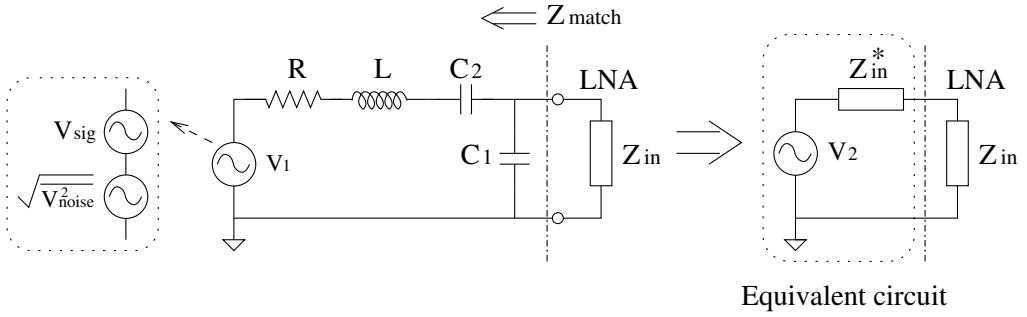

(a) 50Ω matching scheme

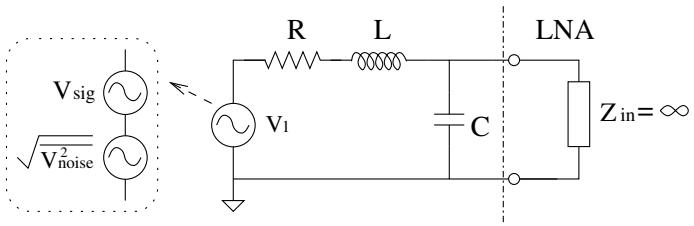

(b) Infinite Z_{in} matching scheme

Figure 5.1: Comparison of the power matching schemes

In practical applications, $R < Z_{in}$ is normally true as the Q factor of the NQR coil is very high. In the model shown in Fig. 5.1 (a), a signal source V_{sig} is used to represent the NQR signal picked up by the NQR coil. Two main noise sources determine the noise power at the receiver. The one is caused by the parasitic resistance of the coil; the other is the noise from the detection environment. Hence, without loss of generality, the noise is modeled by $\sqrt{\overline{V_{noise}^2}}$. The detailed review of the noise sources and noise model will be given in Chapter 6. If perfect matching is achieved at the NQR signal frequency ω_o, the equivalent circuit in Fig. 5.1 (a) can be used to derive the signal power and the input noise power for the LNA. The equivalent voltage source V_2 in Fig. 5.1 (a) is found by combining $\sqrt{\overline{V_{noise}^2}}$ and V_{sig}:

$$V_2 = \frac{(V_{sig} + \sqrt{\overline{V_{noise}^2}})}{1 + \frac{C_1}{C_2} + j\omega RC_1 - \omega^2 LC_1} \tag{5.1}$$

By letting $\sqrt{\overline{V_{noise}^2}} = 0$, the input signal to the LNA is

$$V_{sig\_in} = \frac{1}{2}V_2\Big|_{\sqrt{\overline{V_{noise}^2}}=0} = \frac{\frac{1}{2}V_{sig}}{1+\frac{C_1}{C_2}+j\omega_o RC_1-\omega_o^2 LC_1}$$

$$\Rightarrow \ |V_{sig\_in}| = \frac{\frac{1}{2}|V_{sig}|}{\sqrt{(1+\frac{C_1}{C_2}-\omega_o^2 LC_1)^2+(\omega_o RC_1)^2}} \tag{5.2}$$

By letting $V_{sig} = 0$, the input noise to the LNA is

$$\sqrt{\overline{V_{n\_in}^2}} = \frac{1}{2}V_2\Big|_{V_{sig}=0} = \frac{\frac{1}{2}\sqrt{\overline{V_{noise}^2}}}{1+\frac{C_1}{C_2}+j\omega_o RC_1-\omega_o^2 LC_1}$$

$$\Rightarrow \ |\sqrt{\overline{V_{n\_in}^2}}| = \frac{\frac{1}{2}|\sqrt{\overline{V_{noise}^2}}|}{\sqrt{(1+\frac{C_1}{C_2}-\omega_o^2 LC_1)^2+(\omega_o RC_1)^2}} \tag{5.3}$$

When $w = w_o$, the L–section matching network should be able to transfer the coil impedance $R + j\omega L$ to $Z_{match} = Z_{in} = 50\Omega$. To that end, C_1 and C_2 should be [90]:

$$C_1 = \frac{1}{\omega_o Z_{in}}\sqrt{\frac{Z_{in}-R}{R}} \tag{5.4}$$

$$C_2 = \frac{1}{\omega_o^2 L - \omega_o\sqrt{R(Z_{in}-R)}} \tag{5.5}$$

Bringing Eq. (5.4) and (5.5) into Eq. (5.3), the input noise becomes

$$|\sqrt{\overline{V_{n\_in}^2}}| = \frac{\frac{1}{2}|\sqrt{\overline{V_{noise}^2}}|}{\sqrt{\frac{R^2}{Z_{in}^2}+\frac{(Z_{in}-R)R}{Z_{in}^2}}} = \frac{1}{2}\sqrt{\frac{Z_{in}}{R}}|\sqrt{\overline{V_{noise}^2}}| \tag{5.6}$$

Similarly, substituting Eq. (5.4) and (5.5) in Eq. (5.2), the input signal becomes

$$|V_{sig\_in}| = \frac{1}{2}\sqrt{\frac{Z_{in}}{R}}|V_{sig}| \tag{5.7}$$

Let us also consider the power matching scheme shown in Fig. 5.1 (b). The LNA in Fig. 5.1 (b) is customized to have infinite input impedance. The input of the LNA is directly connected to the resonant capacitor C. Similarly, the input signal of this LNA can be derived as

$$V_{sig\_inf\_in} = \frac{V_{sig}}{1 + j\omega RC - \omega^2 LC} \tag{5.8}$$

and the noise is

$$\sqrt{\overline{V^2_{n\_inf\_in}}} = \frac{\sqrt{\overline{V^2_{noise}}}}{1 + j\omega RC - \omega^2 LC} \tag{5.9}$$

Unlike the 50Ω matching network, Fig. 5.1 (b) only contains one resonant capacitor — C. When $\omega = \omega_o$, $\omega_o^2 LC = 1$. Therefore, Eq.(5.8) becomes

$$V_{sig\_inf\_in} = \frac{V_{sig}}{j\omega_o RC} = \frac{\omega_o L V_{sig}}{jR}$$

$$\Rightarrow \ |V_{sig\_inf\_in}| = \frac{\omega_o L |V_{sig}|}{R} = Q|V_{sig}| \tag{5.10}$$

and Eq.(5.9) becomes

$$\sqrt{\overline{V^2_{n\_inf\_in}}} = \frac{\sqrt{\overline{V^2_{noise}}}}{j\omega_o RC} = \frac{\sqrt{\omega_o L \overline{V^2_{noise}}}}{jR}$$

$$\Rightarrow \ |\sqrt{\overline{V^2_{n\_inf\_in}}}| = \frac{\omega_o L |\sqrt{\overline{V^2_{noise}}}|}{R} = Q|\sqrt{\overline{V^2_{noise}}}| \tag{5.11}$$

Comparing Eq.(5.6) to Eq.(5.11) and Eq.(5.7) to Eq.(5.10), both of the passive LC networks, (L,C_1,C_2) for the 50Ω matching scheme and (L,C) for the infinite matching scheme, provide certain gains to the signal as well as the noise. For the 50Ω matching scheme, the gain G_{50} is:

$$G_{50} = \frac{|V_{sig\_in}|}{|V_{sig}|} = \frac{1}{2}\sqrt{\frac{50}{R}} \tag{5.12}$$

For the infinite matching scheme, the gain G_{inf} is:

$$G_{inf} = \frac{|V_{sig\_inf\_in}|}{|V_{sig}|} = Q = \frac{\omega_o L}{R} \tag{5.13}$$

By inspecting Eq. (5.12) and (5.13), it is not apparent which one is larger. Here we use a real design example to demonstrate the difference between the two matching schemes. An NQR coil made of copper can easily have $L = 2.5\mu H$ with $Q = 80$ at $4MHz$, which leads to $R \approx 0.79\Omega$. As a result, $G_{50} \approx 4$ whereas $G_{inf} = Q = 80$. The infinite impedance matching scheme have much higher gain than the 50Ω matching scheme. The gain from the passive networks will help improve the noise factor. By definition, the noise factor (NF) of a circuit (LNA in this case), is the ratio of the total output noise power to the portion of output noise power contributed by the input noise of the circuit. Thus, the NF is derived by

$$\begin{aligned} NF &= \frac{P_{noise\_out}}{A^2\ P_{noise\_in}} = \frac{A^2G^2\overline{V_{n\_in}^2} + A^2\overline{V_{n\_LNA\_in}^2}}{A^2G^2\overline{V_{n\_in}^2}} \\ &= 1 + \frac{\overline{V_{n\_LNA\_in}^2}}{G^2\overline{V_{n\_in}^2}} \end{aligned} \tag{5.14}$$

where A is the gain of the LNA; G represents the gain of the passive network; and $\overline{V_{n\_LNA}^2}$ denotes the input referred additive noise power of the LNA. From Eq.(5.14), we can see that two design options can be adopted to minimize the NF. The first option is to minimize additive noise from the LNA. This part of work will be discussed in Chapter 6. The other option is to maximize G, the gain of the passive network. Therefore, assuming the LNA for each case has similar additive noise power, and $\overline{V_{noise}^2}$ is at the same level for both matching networks, since the infinite impedance matching scheme has a much higher gain than the 50Ω matching scheme, the NF of the LNA with infinite impedance matching is much lower.

Furthermore, tuning the 50Ω matching network requires changing two design variables

C_1 and C_2 for a specific NQR frequency, whereas infinite impedance matching only needs to change one resonant capacitor C. From the perspective of design complexity, the infinite impedance matching is obviously more favorable.

5.2 Power Multiplexing Strategy

In order to benefit from both the Class-D PA, which requires a series LC network, and the infinite impedance power matching scheme, which requires a parallel LC network, there should be two switchable configurations for connecting the NQR probe coil and resonant capacitor. To fulfill this function, a power multiplexing strategy is proposed.

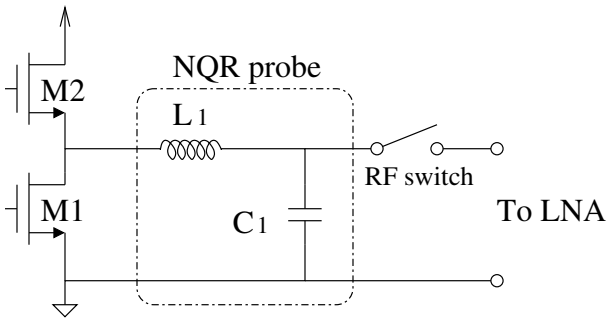

Figure 5.2: The Class-D PA output stage with the NQR probe

Fig. 5.2 shows the output stage of the class-D PA and NQR probe. During the transmitting period, $M1$ and $M2$ is turned on alternately to maintain the transmission power while the RF switch is kept open. When the receiving period starts , $M1$ is turned on while $M2$ is shut off such that the NQR probe is connected in a parallel LC tank manner. Now the RF switch is closed to conduct signals to the LNA. When $M1$ is turned on to construct the parallel-LC-tank NQR probe, this NMOS can be modeled as a resistor in series with the NQR probe. Its resistance is equal to R_{on}, the on-resistance of $M1$. Usually, $M1$ is chosen

to have very small R_{on} value (tens of $m\Omega$) such that the Class-D PA can achieve high power efficiency. On the other hand, the series resistance of the coil is generally greater than hundreds of $m\Omega$. Therefore, $M1$ only contributes around 10% additional series resistance. The Q factor of the NQR probe is compromised to 10% less of its original value. $M1$ will certainly increase the thermal noise level. But for NQR detection, this degradation is tolerable.

Apparently, the proposed power multiplexing strategy is specifically designed to cooperate with the Class-D PA in the system. On the receiving side, the 50Ω matching scheme can also be used. The only difference from Fig. 5.2 is that between the RF switch and 50Ω LNA a matching network is needed. This also reveals another reason of why the infinite impedance matching scheme is chosen for this detection system.

5.3 RF Switch for Power Multiplexing

In Fig. 5.2, it can be seen that the RF switch is playing a key role throughout the whole NQR detection process. On one hand, the RF switch needs to have high isolation capability so that the high transmission power efficiency can be sustained. Meanwhile, the sensitive receiver-side circuit also needs to be protected from high transmission power. On the other hand, the RF switch must have low introducing signal degradation as NQR signals are inherently weak and vulnerable to any disturbance.

5.3.1 Traditional Quarter Wave Switches

In traditional NQR lab equipment, quarter-wave switches, shown in Fig. 5.3, are ideal for realizing this function. During the transmitting period, two back to back diodes on the receiving side will be turned on such that this side of transmission cable can be considered as shorted to GND. As a result, with a quarter wave length of transmission line connected between $RFin$ and $RFout$, the equivalent impedance seen from $RFin$ side is infinity, which

will block transmission power from passing into the receiver. During the receiving period, the NQR signal power level is so small that the two diodes cannot be turned on. Thus, NQR signals can pass through the transmission cable and be captured by the receiver.

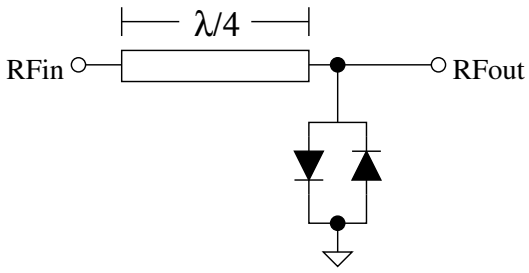

Figure 5.3: The quarter-wave RF switch

Obviously, the quarter-wave switch is favorable to lab equipment. It has a very simple circuit structure. Also, it cooperates with NQR systems automatically without any control circuit. Its low additive noise benefits detection accuracy. However, for portable explosive detection NQR systems, it is not a practical choice because of its bulky volume. For instance, for a $6MHz$ NQR signal (the upper limit of explosive NQR signal frequencies), a quarter of its wavelength is equal to $12.5m$, which requires the same length of the transmission cable. Besides, for different explosive materials, different NQR frequencies demand different cable lengths accordingly to realize the quarter-wave switch. It apparently complicates the system design.

5.3.2 Features of PIN Diodes

PIN diodes are semiconductor devices which consist of three layers: a high resistive intrinsic I layer in between a highly doped P-type layer and N-type layer [92]. The function of the added I layer can be described as a charge pool. When the PIN diode is forward biased,

the charge pool is loaded with free charges so that the PIN diode acts similarly to a regular diode. The PIN diode will introduce a PN conjunction voltage drop and a low additive resistance value. The resistance value depends on the DC bias current for the PIN diode. With a $100mA$ DC forward biasing current, the resistance can drop to less than 1Ω. When the PIN diode is reverse biased, the charge pool is drained up. The I layer provides high isolation between P and N so that the capacitance between P and N terminals is very low (around a few pF). A more interesting characteristic of PIN diodes is that as charging and discharging I layer requires a certain amount of time (usually around tens of μS), high power AC signals can be switched on and off with a low power DC biasing control signal.

5.3.3 PIN Diode Based RF Switches

Compared to quarter-wave switches, PIN diode switches obviously have some drawbacks. 1) It requires extra control and driving circuit to support PIN diodes. 2) It consumes power during the on-state as a DC bias current is needed to provide low signal attenuation. Despite the drawbacks, the advantages of PIN diode switches are more remarkable. 1) It can be integrated in a compact volume. 2) It has a universal setup for all explosive materials' NQR frequencies.

In this design, a 3-stage PIN diode based switch is employed. The simplified schematic of the circuit is shown in Fig. 5.4. As the NQR stimulus signal is in a high power level, the 3-stage structure is used to provide high isolation between the NQR probe and the receiver circuit during the transmission period. The first two stages are operating on a high voltage (*High_volt* in Fig. 5.4). Since the voltage amplitude of the oscillation inside the NQR probe during the transmission period can easily reach $500V$, *High_volt* must be able to be tuned up to $100V$. Two regular RF diodes are added at the receiver side to guarantee the protection for the LNA. The third stage is switched by a low voltage, $5V$ in Fig. 5.4, to make sure

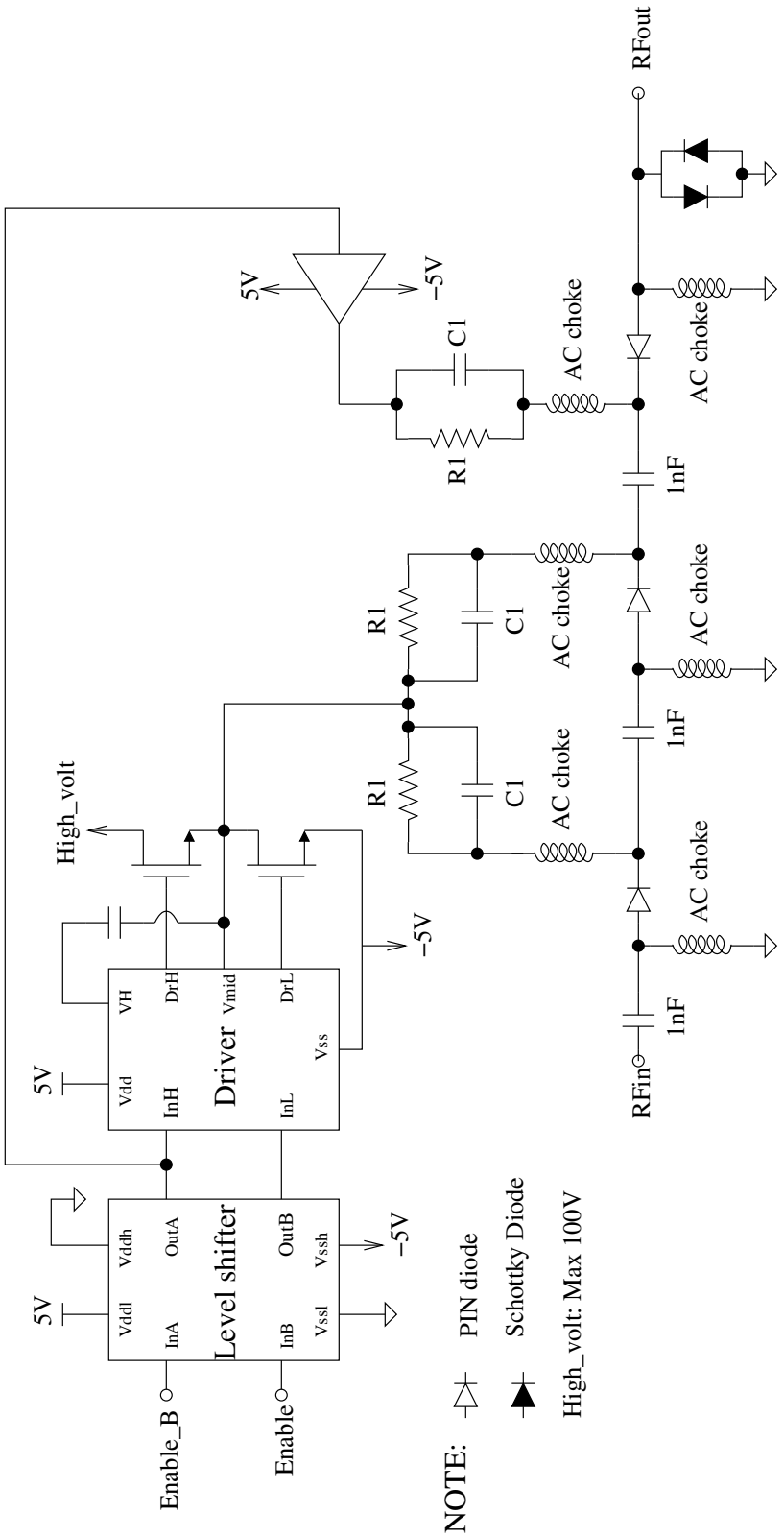

Figure 5.4: The 3-stage PIN diode RF switch

those two RF diodes are well isolated from the NQR probe during high power transmission. During the receiving period, all PIN diodes are forward biased with a $100mA$ DC current. In each stage, two AC choke inductors are needed to provide a DC current path while blocking AC signals from leaking to GND. On the contrary, the $1nF$ capacitors between each stage block the DC current. $R1$ in Fig. 5.4 provides the current limitation. When the PIN diodes are being turned on, i.e. the driving signal is switching from $High\_volt$ to $-5V$, $C1$ provides a low impedance path to reduce the turning-on time for PIN diodes. The test results show that this 3-stage PIN diode switch can provide up to $75dB$ isolation with $20\mu s$ turning-on time.

5.4 Conclusion

In this chapter, the infinite impedance power matching mechanism is presented. Compared to the traditional 50Ω matching scheme, the infinite matching scheme can result in a much higher passive gain with a simpler network configuration, which only requires one resonant capacitor. This feature also benefits the tuning process for the NQR probe as only one resonant capacitor needs to be adjusted for different NQR frequencies. In addition, a power multiplexing strategy is proposed to cooperate with the Class-D PA to switch the NQR probe configuration between the series LC network and the parallel LC network for the transmitting and the receiving period, respectively. To implement the power multiplexing strategy, a PIN diode based RF switch circuit is designed to provide high isolation during off-state and low additive noise during on-state. The test results of the infinite matching scheme and power multiplexer will be presented together with the LNA in Chapter 6.

Chapter 6

Receiver Hardware Configuration I: LNA and VGA Design

As introduced in Chapter 3, the receiver section is mainly dedicated to acquiring, amplifying and processing NQR signals. In this and the following chapters, the front-end analog receiving circuit chain is presented with detailed designs. This part of circuits consist of two LNAs for the NQR signal path, an LNA for the RFI signal path, an RFI mitigation filter and a VGA. Basically all of the circuits before ADC are included. The two LNAs correspond to the 50Ω and infinite power matching networks, respectively. Thanks to the fast evolving CMOS mixed-signal design technologies, the mainstream idea of designing compact circuit systems nowadays is to integrate multiple function units, which even cross digital and analog signal domains, into one single chip. In this work, we also take this advantage to further reduce the volume and cost of the system by designing and fabricating a customized CMOS IC. This chip is designed with 0.18 μm CMOS process. The whole front-end receiving circuit chain is integrated into the IC.

In this chapter, the amplification circuits, including the LNAs and VGA, are discussed with detailed design concepts and circuit configurations. The RFI mitigation filter circuit

design will be discussed in Chapter 7. In addition, an MCU, which is responsible for generating control logic to coordinate the transmitting and receiving sections, is also included in the customized IC. This part of work will be discussed in Chapter 8.

6.1 LNA Design

An LNA provides signal amplification with low additive noise to overcome the noise added during the subsequent signal processing. In the proposed receiver circuits, there are totally three LNA circuits integrated in the customized IC. Two LNAs have the identical circuit configuration. The input impedance of this type of LNA is equal to 50Ω. One of them is for the NQR probe with a 50Ω power matching network, and the other is for the RFI probe. The third LNA has high input impedance and a fully differential circuit structure. Obviously, this LNA is designed to work with the NQR probe which has the so-called "infinite" power matching network that has been introduced in Chapter 5.

6.1.1 Background

To help to understand the design details of LNAs used in this work, first, the related background knowledge is briefly reviewed. We start from noise models of MOSFETs and resistors, which are the major components used to construct LNA circuits. Also, the general design requirements of LNAs for NQR systems are discussed.

6.1.1.1 Noise Sources and Models for CMOS Technology

There are mainly three types of noise that are usually seen in semiconductor devices: thermal noise, shot noise and flicker noise. As the shot noise occurs in PN junctions, it is prevalent in diodes and bipolar transistors but not common in MOSFETs and resistors. In CMOS LNA circuits, diodes and bipolar transistors are seldom used. Or, we can even say that they have

never been used. Therefore, only thermal noise and flicker noise are considered for noise analysis of CMOS LNA circuits.

Thermal noise is caused by thermal excitation of charge carriers in conductors. It is also known as Johnson-Nyquist noise to honor the two authors who discovered this phenomenon [93, 94]. Thermal noise has a white spectral density that is proportional to the temperature. As long as the device has resistance and the temperature isn't absolute zero degree, which is true for all electronic devices, the thermal noise will appear. Flicker noise is also called $1/f$ noise or pink noise as its power spectral density is inversely proportional to f^a, where a has typical value between 0.8 and 1.3 [95]. It is often see in the active device with a DC current flowing. The mechanism of flicker noise is still remaining mysterious even though many researchers have proposed some models to explain it. A common acceptable interpretation is that the flicker noise is due to the random capture and emission effect of the surface traps to the free charge carriers [96] inside semiconductors.

The main noise source that concerns resistors is thermal noise. It can be modeled as a voltage source V_n, in series with a noise free resistor R, as shown in Fig. 6.1 (a). As expected, V_n has random values which demonstrate the white spectral density that is described by

$$\overline{V_n^2}(f) = 4kTR \tag{6.1}$$

where k is the Boltzmann's constant, T is the absolute temperature, and R is the resistance of the resistor under discussion. For the interested signal that has the bandwidth equal to B, the voltage source has the averaged voltage power equal to $\overline{V_n^2} = 4kTRB$. Here, the averaged voltage power is defined as the averaged power delivered by the voltage source on a 1Ω resistor.

MOSFETs have the noise contributions from both flicker noise and thermal noise. The noise model for a NMOS is illustrated in Fig. 6.1 (b). Flicker noise is conventionally

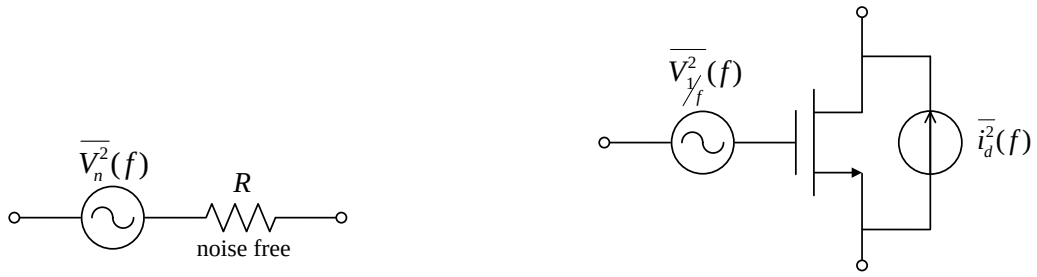

(a) noise model for resistor R (b) noise model for a NMOS

Figure 6.1: Noise models for the devices used in LNAs

represented by a voltage source $V_{1/f}$ in series with the gate. Its power spectral density can be numerically calculated by:

$$\overline{V_{1/f}^2}(f) = \frac{K}{WLC_{ox}f} \tag{6.2}$$

where K is a constant related to the MOSFET device. W and L are the width and length of the device. C_{ox} is the gate capacitance per unit area. Based on Eq. (6.2), one straightforward observation is that power of flicker noise can be reduced by increasing the size of the device.

Thermal noise is caused by the channel resistance. It is usually represented by a current source in parallel with the device channel. Given the unevenly distributed resistance along the channel when the device is in active working region, the resultant thermal noise can be modeled by:

$$\overline{I_{d,thermal}^2}(f) = 4 \cdot \frac{2}{3} kT g_m \tag{6.3}$$

where g_m is the transconductance of the NMOS. Same as $1/f$ noise, the thermal noise current source can also be equivalently modeled by a gate noise voltage source by:

$$\overline{V_{g,thermal}^2}(f) = \frac{4 \cdot \frac{2}{3} kT}{g_m} \tag{6.4}$$

Therefore, assuming $1/f$ noise and thermal noise are uncorrelated, these two gate noise

voltage sources can be summed up into one noise voltage source:

$$\overline{V_g^2}(f) = \frac{K}{WLC_{ox}f} + \frac{4 \cdot \frac{2}{3}kT}{g_m} \tag{6.5}$$

6.1.1.2 General Design Requirements of LNAs for NQR Systems

As the NQR signal is inherently weak, SNR of the signal collected by the probe is very low. The noise factor of the signal chain needs to be controlled to a low value. As discussed in Chapter 3, the noise factor of the detection systems is mainly constrained by the first amplification stage, the LNA. Hence, the first requirement for the LNAs is to have a low noise factor. In fact, the noise figure (NF) is preferably used to evaluate the performance of an LNA circuit. An NF is simply a noise factor in decibels.

The second requirement is that the LNA needs to have relatively wide working bandwidth. Since NQR signal frequencies for explosives range from $500kHz$ to $6MHz$, LNAs in detection systems should be able to work in the whole frequency range. If the median frequency, $(6 + 0.5)/2 = 3.25MHz$, is considered as the center frequency, the bandwidth that an LNA needs to cover is $6 - 3.25 = 2.75MHz$, almost 90% of the center frequency.

Third, the LNA should provide a relatively high gain for NQR signals so that the noise impact from the downstream circuit is suppressed. It can be explained with the example shown in Fig. 6.2. Let us assume that a detection system has three amplification stages. The gain, input referred noise power and noise factor of the three stages are denoted as G_1, $P_{n,1}$, F_1, G_2, $P_{n,2}$, F_2, and G_3, $P_{n,3}$, F_3, respectively. Note that the gain G_i, $i \in 1, \ldots, 3$ for each stage is actually the power gain, which is the square of the voltage gain. The overall

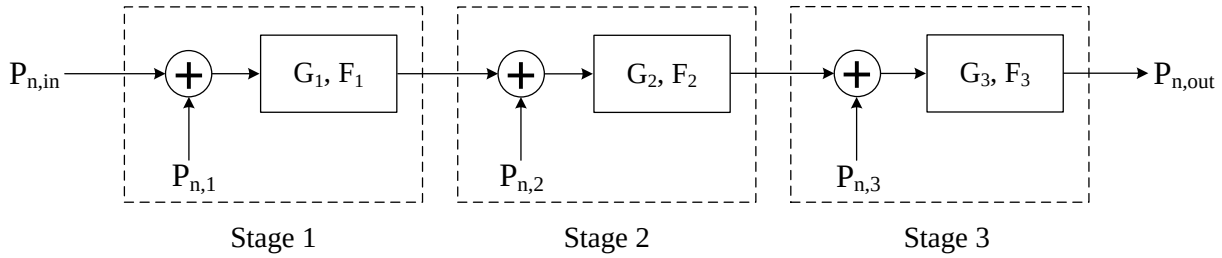

Figure 6.2: A cascaded system with 3 gain stages

noise factor F_o of the system is derived by:

$$\begin{aligned} F_o &= \frac{\textit{total output noise power}}{\textit{output noise power due to the input noise}} \\ &= \frac{P_{n,in} \cdot G_1G_2G_3 + P_{n,1} \cdot G_1G_2G_3 + P_{n,2} \cdot G_2G_3 + P_{n,3} \cdot G_3}{P_{n,in} \cdot G_1G_2G_3} \\ &= \frac{P_{n,in} \cdot G_1G_2G_3 + P_{n,1} \cdot G_1G_2G_3}{P_{n,in} \cdot G_1G_2G_3} + \frac{P_{n,2} \cdot G_2G_3}{P_{n,in} \cdot G_1G_2G_3} + \frac{P_{n,3} \cdot G_3}{P_{n,in} \cdot G_1G_2G_3} \end{aligned} \tag{6.6}$$

The first term of Eq. (6.6) is obviously equal to F_1. The second term can be rewritten as:

$$\begin{aligned} \frac{P_{n,2} \cdot G_2G_3}{P_{n,in} \cdot G_1G_2G_3} &= \frac{1}{G_1} \cdot \left(\frac{P_{n,2} \cdot G_2}{P_{n,in} \cdot G_2} + 1 - 1 \right) \\ &= \frac{1}{G_1} \cdot \left(\frac{P_{n,2} \cdot G_2 + P_{n,in} \cdot G_2}{P_{n,in} \cdot G_2} - 1 \right) \\ &= \frac{1}{G_1} \cdot (F_2 - 1) \end{aligned} \tag{6.7}$$

Similarly, the third term can also be rewritten as:

$$\frac{P_{n,3} \cdot G_3}{P_{n,in} \cdot G_1G_2G_3} = \frac{1}{G_1G_2} \cdot (F_3 - 1) \tag{6.8}$$

Substituting Eq. (6.7) and Eq. (6.8) into Eq. (6.6), the noise factor for the whole system is:

$$F_o = F_1 + \frac{1}{G_1} \cdot (F_2 - 1) + \frac{1}{G_1 G_2} \cdot (F_3 - 1) \tag{6.9}$$

From Eq. (6.9), we can see that F_o mainly depends on F_1. F_2 is mitigated by the power gain of the first stage, G_1. F_3 is mitigated by G_1 and G_2. Actually, in general, the noise factor contribution from the n_{th} stage, $F_{o,n}$, is:

$$F_{o,n} = \frac{F_n - 1}{\prod_{i=1}^{n-1} G_i} \tag{6.10}$$

Based upon Eq. (6.9), we can see that a high LNA gain G_1 can significantly suppress the noise contribution from the following stages.

Finally, high linearity is also a requirement for the LNA. This is due to the influence of RFI. In some cases, RFI is much higher than NQR signals, and an LNA with poor linearity will be saturated by high RFI. However, RFI signals still have much lower power level than the RF signals in conventional communication systems. Hence, the demand on linearity in this design is not strict.

6.1.2 LNA with Infinite Input Impedance

CMOS-based amplifiers can have large input impedance as their active devices, MOSFETs, are voltage controlled. More specifically, the input end can be connected to the gate of a MOSFET which ideally has no DC current path except a small amount of gate leakage current. For AC signals, when MOSFETs are working in the saturation region, which normally is the case for CMOS amplifiers, the gate parasitic capacitor is usually less than $1pF$ [97], even for large-sized MOSFETs. Therefore, compared to the resonant capacitor of the NQR probe, the input impedance of CMOS-based amplifiers is considered as a very high value

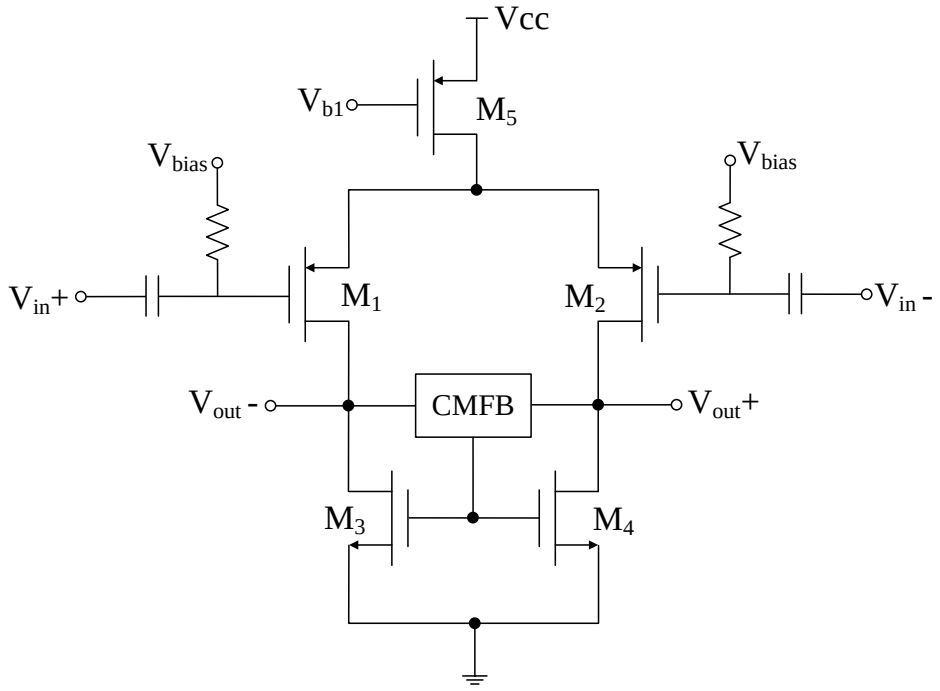

Figure 6.3: A differential low-noise amplifier

which satisfies the infinite input impedance power matching scheme.

The simplified schematic of the LNA circuit is shown in Fig. 6.3. A fully differential structure is used to cancel the common mode noise that is prevalent in the NQR probe. The two input ends of LNA are connected to the two sides of the NQR probe via the RF switch.

Fig. 6.3 can be redrawn to be Fig. 6.4 for noise analysis. Here, all the noise sources are assumed to be independent to each other. The input referred noise model is adopted for every noise source for analyzing its impact. In addition, the superposition theory is applied, which means that every noise source is analyzed with letting other sources equal to zero. As the LNA is fully differential, ideally, the noise from the common mode feedback (CMFB) circuit and the tail bias $M5$ causes equal voltage variations on V_{out-} and V_{out+}, which is considered as common mode noise, and has no impact on the following differential circuit. The noise

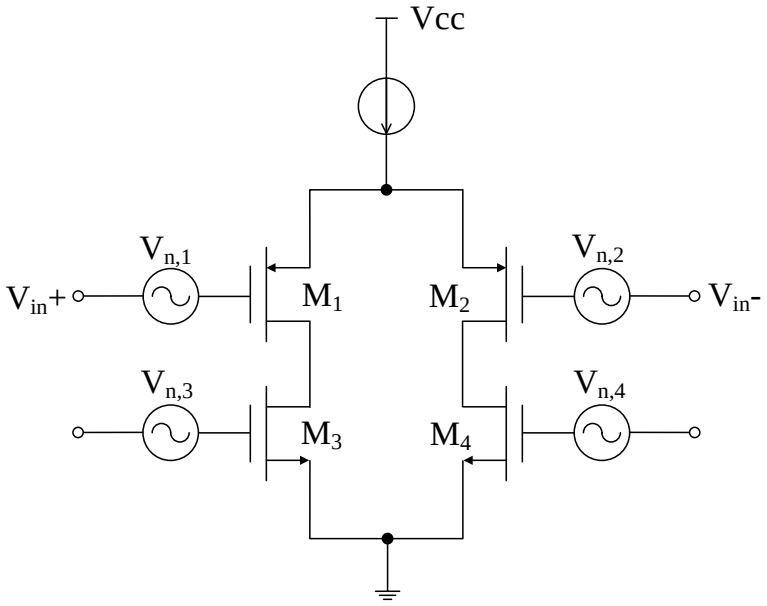

Figure 6.4: Noise sources of MOSFETs

contribution thereof is ignored for noise analysis. However, since mismatch is unavoidable in the realistic circuits, these two noise sources will still contribute some additive noise on the differential output.

For the input device $M1$, the gate noise source $V_{n,1}$ can just be treated as an input signal. Hence, according to Eq. (6.5), the input referred noise power density from $M1$ is:

$$\overline{V_{in,1}^2}(f) = \frac{K_p}{W_1 L_1 C_{ox} f} + \frac{4 \cdot \frac{2}{3} kT}{g_{m1}} \tag{6.11}$$

where K_p is the $1/f$ noise constant for PMOS $M1$ and $M2$. W_1 and L_1 are the width and length of $M1$. g_{m1} is the transconductance of $M1$.

For $M3$, the gate noise source leads to a current signal $i_{n,3} = V_{n,3} g_{m3}$, where g_{m3} is the

transconductance of $M3$. This equivalent input referred noise voltage of $M3$ is:

$$V_{in,3} = \frac{i_{n,3}}{g_{m1}} = \frac{g_{m3}}{g_{m1}} V_{n,3}. \tag{6.12}$$

The input referred noise power density of $M3$ can be calculated using Eq. (6.5) and Eq. (6.12):

$$\begin{aligned} \overline{V_{in,3}^2}(f) &= \left(\frac{g_{m3}}{g_{m1}}\right)^2 \left(\frac{K_n}{W_3 L_3 C_{ox} f} + \frac{4 \cdot \frac{2}{3} kT}{g_m 3}\right) \\ &= \left(\frac{g_{m3}}{g_{m1}}\right)^2 \frac{K_n}{W_3 L_3 C_{ox} f} + \frac{g_{m3}}{g_{m1}^2} \left(4 \cdot \frac{2}{3} kT\right) \end{aligned} \tag{6.13}$$

Similarly, as the circuit is symmetric, $V_{n,2}$ and $V_{n,4}$ lead to input voltage variations identical to $V_{n,1}$ and $V_{n,3}$. Therefore, the total input referred noise is:

$$\begin{aligned} \overline{V_{in}^2}(f) &= 2 \cdot \overline{V_{in,1}^2}(f) + 2 \cdot \overline{V_{in,3}^2}(f) \\ &= \frac{2K_p}{W_1 L_1 C_{ox} f} + \frac{\frac{16}{3} kT}{g_{m1}} + \left(\frac{g_{m3}}{g_{m1}}\right)^2 \frac{2K_n}{W_3 L_3 C_{ox} f} + \frac{g_{m3}}{g_{m1}^2} \left(\frac{16}{3} kT\right) \\ &= \underbrace{\frac{\frac{16}{3} kT}{g_{m1}} + \frac{g_{m3}}{g_{m1}^2} \left(\frac{16}{3} kT\right)}_{Thermal\ noise} + \underbrace{\frac{2K_p}{W_1 L_1 C_{ox} f} + \left(\frac{g_{m3}}{g_{m1}}\right)^2 \frac{2K_n}{W_3 L_3 C_{ox} f}}_{1/f\ noise} \end{aligned} \tag{6.14}$$

According to Eq. (6.14), it can be seen that thermal noise from the devices can be reduced by enlarging g_{m1}. That can be achieved by increasing the bias current and the width of M_1 and M_2. Decreasing g_{m3} seems helpful to reduce thermal noise as well. But it has side effects such as decreasing the CMFB loop gain.

Regarding $1/f$ noise, to get more insight of the relation between adjusting devices dimensions and the resulting noise performance, the latter term in Eq. (6.14) can be rewritten

by substituting $g_{mi} = \sqrt{2\mu_i C_{ox} I_d \frac{W_i}{L_i}}$:

$$\begin{aligned}
\overline{V_{in,1/f}^2}(f) &= \frac{2K_p}{W_1 L_1 C_{ox} f} + \left(\frac{g_{m3}}{g_{m1}}\right)^2 \frac{2K_n}{W_3 L_3 C_{ox} f} \\
&= \frac{2K_p}{W_1 L_1 C_{ox} f} + \frac{2\mu_n C_{ox} I_d \frac{W_3}{L_3}}{2\mu_p C_{ox} I_d \frac{W_1}{L_1}} \frac{2K_n}{W_3 L_3 C_{ox} f} \\
&= \frac{2K_p}{W_1 L_1 C_{ox} f} + \frac{2K_n}{C_{ox} f} \cdot \frac{\mu_n L_1}{\mu_p W_1 L_3^2}
\end{aligned} \tag{6.15}$$

where I_d is the bias current for $M1$ and $M3$. From Eq. (6.15), L_1 needs to be optimized as it is inversely proportional to the first term whereas proportional to the second term. L_3 should be enlarged to reduce $1/f$ noise. Same with the thermal noise case, W_1 needs to be maximized to minimize $1/f$ noise.

The LNA with infinite input impedance is designed based on the above noise performance considerations. In the NQR frequency range, $1/f$ noise is still fairly comparable to thermal noise for CMOS technology. Hence, PMOS is used as the input stage to have lower $1/f$ noise because with the same bias condition and size, PMOS generally has 1/3 $1/f$ noise of NMOS. $M1$ and $M2$ are assigned a big area, $W_1 \times L_1 = 800\mu m \times 0.36\mu m$ to suppress $1/f$ noise. In addition to a large W_1 value, a large bias current, $2mA$, is driven into the input pair to reduce thermal noise. On the NMOS side, a long channel length, $L_3 = 2\mu m$, is applied to reduce $1/f$ noise.

The gain of the differential pair LNA is:

$$Gain = g_{m1} r_{out} = g_{m1}(r_{o,3} \parallel r_{o,1}) \tag{6.16}$$

where r_{out} is the output resistance of the LNA that is equal to the output resistance of $M3$, $r_{o,3}$, in parallel with the output resistance of $M1$, $r_{o,1}$. Same with the design for noise optimization, to have a high $Gain$ value, g_{m1} needs to be maximized. In addition, a long

channel length of $M3$ will not only reduce $1/f$ noise, but also increase the value of $r_{o,3}$ and therefore increase the gain.

As the differential pair LNA is configured as an open-loop and single stage network, the transfer function $G(f)$ can be approximated with a first order system. In other words, $G(f)$ only has one pole. $G(f)$ is given by

$$G(f) = \frac{A_{DC}}{1 + f/f_o} = \frac{g_{m1} r_{out}}{1 + r_{out} C_{load} \cdot 2\pi f} \tag{6.17}$$

The bandwidth of a first order system is mainly limited by its single pole, which is the output node pole, $f_o = 1/2\pi r_{out} C_{load}$. Since the load of this LNA is the input stage of next amplification stage, C_{load} is usually less than $1pF$. In addition, as the bias current for $M1$ and $M3$ is set to be a large value in favour of noise performance, and $r_{o,i} = 1/\lambda I$, $r_{out} = r_{o,1} \parallel r_{o,3}$ often has a value around several $k\Omega$. As a result, the $-3dB$ bandwidth of the LNA is around tens of MHz, much higher than the upper limit of NQR frequency range.

In short, this LNA can meet all the requirements for NQR systems very well. The detailed performance evaluations of this LNA is presented in Section 6.3.

6.1.3 LNA with 50Ω Input Impedance

In this design, two wide-band LNAs with 50Ω input impedance are incorporated. One is for the RFI signal path. The other is for the NQR probe which has the general 50Ω matching network. The purposes of having this type of LNA are to provide options for the receiver circuit to work with a traditional transmitter circuit, or the proposed transmitter circuit but with a secondary receiving probe whose output impedance is matched to 50Ω. The discussion in this section starts with a review of the conventional one-stage LNA to see its noise figure limitations. Then, the adopted circuit configuration is presented.

6.1.3.1 NF Limitations of the Conventional Single Stage LNA ($Z_{in} = 50\Omega$)

As the noise performance is the primary design concern for either the RFI signal LNA or the NQR signal LNA, pursuing lowest possible NF is the main goal to choose a circuit configuration. Single stage LNAs with the input impedance matched to 50Ω have been widely applied for wide-band RF signals. However, this type of LNAs suffer from NF limitations due to the trade-off between impedance matching and noise factor. Some commonly used circuit structures are reviewed to explain this issue.

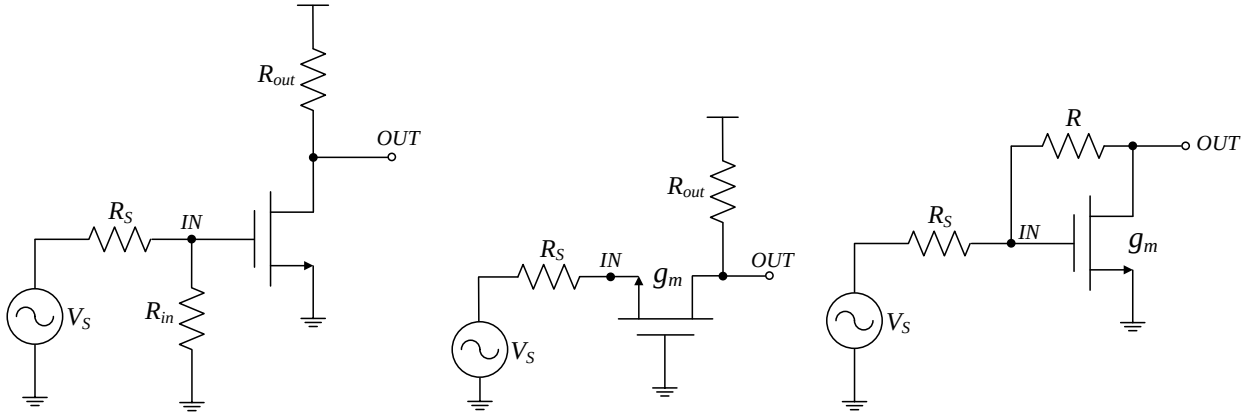

(a) (b) (c)

Figure 6.5: Commonly used single stage LNAs with $Z_{in} = 50\Omega$: (a) R_{in} matching; (b) g_m matching, common-gate amplifier; (c) g_m matching, common-source amplifier.

Fig. 6.5 lists the simplified schematics of three single stage LNAs. In Fig. 6.5 (a), the LNA is a common-source amplifier with a gate resistor R_{in} that is equal to R_s to match the source impedance. It can be seen that R_{in} already contributes the same noise power with R_s, $\overline{V_{R_s}^2}(f) = 4kTR_s$. If the noise power from the MOSFET and R_{out} is taken into account, the noise factor of this LNA can not be lower than 2. In Fig. 6.5 (b) and (c), the impedance matching is realized by adjusting g_m to $1/R_s$. According to Eq. (6.5), the noise introduced

by the MOSFET is:

$$\begin{aligned}\overline{V_g^2}(f) &= \frac{K}{WLC_{ox}f} + \frac{4 \cdot \frac{2}{3}kT}{g_m} \\ &= \frac{K}{WLC_{ox}f} + 4 \cdot \frac{2}{3}kTR_s \end{aligned} \tag{6.18}$$

As a result, the lower bound of the noise factor is derived by:

$$F = \frac{\overline{V_g^2}(f) + \overline{V_{R_s}^2}(f)}{\overline{V_{R_s}^2}(f)} = 1 + \frac{K/WLC_{ox}f}{4kTR_s} + \frac{2}{3} > \frac{5}{3} \tag{6.19}$$

For NQR frequency range, $1/f$ noise may still be the dominant noise source. The actual noise factors of the circuits are much higher than the lower bound.

6.1.3.2 Noise Cancelling Two Stage LNA ($Z_{in} = 50\Omega$)

One way to address the limited noise factor issue is to break the dependance between the impedance matching network and the noise factor. In [98], the authors proposed a noise cancelling technique that can achieve impedance matching and low noise figure at the same time. To understand the noise cancelling technique, let us revisit the circuit shown in Fig. 6.5 (c) for noise analysis. The equivalent circuit is shown in Fig. 6.6 (a). The equivalent circuit is redrawn with noise sources of the MOSFET, as shown in Fig. 6.6 (b). Without losing generality, $1/f$ noise is modeled by a gate voltage source $V_{1/f}$, and thermal noise is modeled by a channel current source i_d. Note that only the first order equivalent circuit of the MOSFET, without r_{ds}, is used in this analysis.

With only $V_{1/f}$ being effective, the noise voltage on the IN node is:

$$V_{n,IN,1/f} = \frac{V_{1/f}g_mR_s}{1 + g_mR_s} \tag{6.20}$$

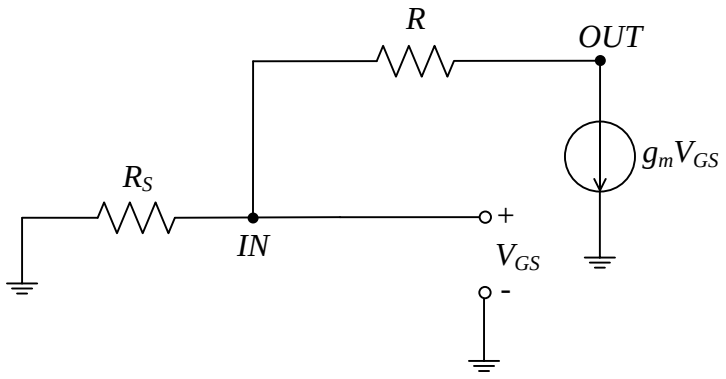

(a) Without noise sources

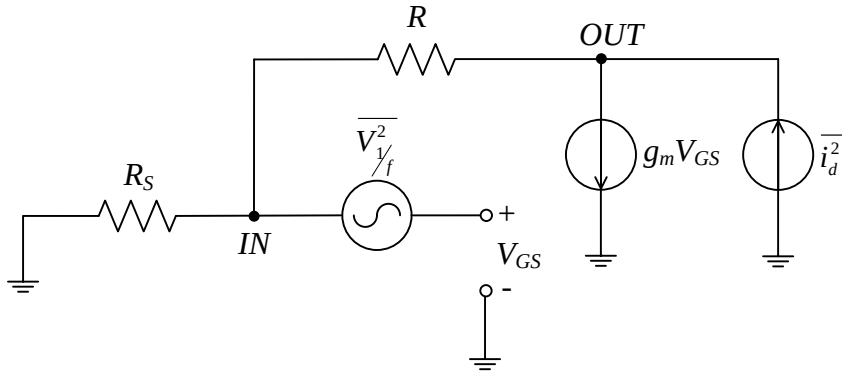

(b) With noise sources

Figure 6.6: Equivalent circuit of Fig. 6.5 (c) with and without noise sources of the MOSFET

The noise voltage on the OUT node is:

$$V_{n,OUT,1/f} = \frac{V_{1/f} g_m (R + R_s)}{1 + g_m R_s} \tag{6.21}$$

With only i_d being effective, the noise voltage on the IN node is:

$$V_{n,IN,id} = \frac{i_d R_s}{1 + g_m R_s} \tag{6.22}$$

The noise voltage on the OUT node is:

$$V_{n,OUT,id} = \frac{i_d(R + R_s)}{1 + g_m R_s} \tag{6.23}$$

Comparing Eq. (6.20) to Eq. (6.21), and Eq. (6.22) to Eq. (6.23), the noise voltages on these two nodes are in the same polarity. The ratio of $V_{n,OUT}$ to $V_{n,IN}$ is

$$\frac{V_{n,OUT}}{V_{n,IN}} = \frac{R + R_s}{R_s} = 1 + \frac{R}{R_s} \tag{6.24}$$

Meanwhile, in Fig. 6.5 (c), the voltage on the IN node resulting from the source signal V_s is

$$V_{s,IN} = \frac{V_s \cdot 1/g_m}{R_s + 1/g_m} \tag{6.25}$$

The output voltage resulting from $V_{s,OUT}$ is:

$$V_{s,OUT} = \frac{1 - g_m R}{1 + g_m R_s} V_s \tag{6.26}$$

When the input impedance of the LNA $1/g_m$ is matched to R_s, $V_{s,IN} = V_s/2$ and $V_{s,OUT} = (1 - g_m R) \cdot V_s/2$. As long as $g_m R > 1$, $V_{s,IN}$ and $V_{s,OUT}$ have different signs, whereas $V_{n,IN}$ and $V_{n,OUT}$ have the same sign. The noise cancelling technique is exactly using this polarity difference between V_s and V_n on IN and OUT nodes.

As shown in Fig. 6.7, another negative gain stage $-A$ is inserted to flip the sign and scale the amplitude of the voltage on the IN node V_{IN}, where $V_{IN} = V_{n,IN} + V_{s,IN}$. Then, the scaled V_{IN} is added to V_{OUT}. With an optimal gain $A = A_o = 1 + R/R_s$, the noise portions will be cancelled whereas signal portions will add up coherently. Consequently, the noise contribution from the MOSFET will be entirely cancelled.

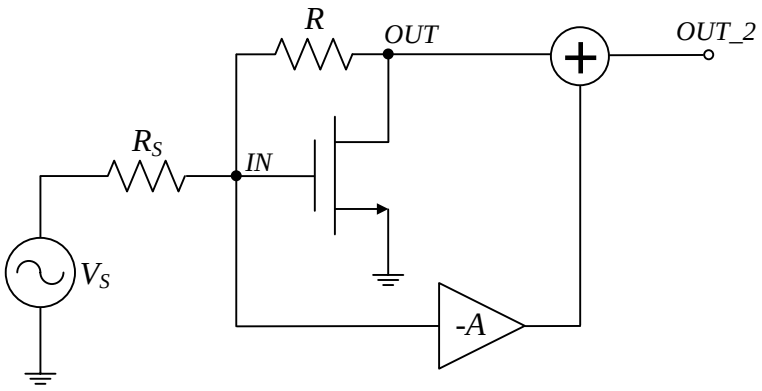

Figure 6.7: The noise cancelling technique.

For the input signal, the total voltage gain A_{total} is the ratio of V_{s,OUT_2} to $V_{s,IN}$:

$$A_{total} = \frac{V_{s,OUT_2}}{V_{s,IN}} = \frac{V_{s,OUT} + (-A)V_{s,IN}}{V_{s,IN}} = 1 - g_m R - A \tag{6.27}$$

With $A = A_o$ and $R_s = 1/g_m$, The optimal total voltage again $A_{total,o}$ is:

$$A_{total,o} = 1 - R/R_s - 1 - R/R_s = -2R/R_s \tag{6.28}$$

It should be noted that R and the $-A$ gain stage also introduce noise power. Based on the equivalent circuit shown in Fig. 6.8, the output referred noise power introduced by R and $-A$, $V_{n,OUT_2,R}$ and $V_{n,OUT_2,-A}$ respectively, are:

$$V_{n,OUT_2,R} = V_{n,R} \tag{6.29}$$

$$V_{n,OUT_2,-A} = A \cdot V_{n,-A} \tag{6.30}$$

In turn, the input referred noise power for R and $-A$, $V_{n,IN,R}$ and $V_{n,IN,-A}$, are:

$$V_{n,IN,R} = \frac{V_{n,OUT_2,R}}{A_{total}} = \frac{V_{n,R}}{A_{total}} \tag{6.31}$$

$$V_{n,IN,-A} = \frac{V_{n,OUT_2,-A}}{A_{total}} = \frac{A}{1 - g_m R - A} V_{n,-A} \tag{6.32}$$

From Eq. (6.31), it can seen that the noise power contributed by R is attenuated by A_{total} when referred back to the input. Similarly, the input referred noise power contributed $-A$ gain stage is attenuated by $\frac{A}{1-g_m R-A}$.

The overall noise factor of the noise cancelling two stage LNA can be derived as:

$$\begin{aligned} F_{total} &= \frac{total\ output\ noise\ power}{output\ noise\ power\ due\ to\ input\ noise} \\ &= \frac{A_{total}^2 \cdot \overline{V_{n,R_s}^2} + \overline{(A \cdot V_{n,IN} + V_{n,OUT})^2} + \overline{V_{n,R}^2} + A^2 \cdot \overline{V_{n,-A}^2}}{A_{total}^2 \cdot \overline{V_{n,R_s}^2}} \end{aligned} \tag{6.33}$$

If $A = A_o = 1 + R/R_s$, the noise factor becomes:

$$\begin{aligned} F_{total,o} &= 1 + \frac{4kTR}{4kTR_s \cdot 4R^2/R_s^2} + \frac{(1 + R/R_s)^2 \cdot \overline{V_{n,-A}^2}}{4kTR_s \cdot 4R^2/R_s^2} \\ &= 1 + \frac{R_s}{4R} + \frac{(1 + R_s/R)^2 \cdot \overline{V_{n,-A}^2}}{16kTR_s} \end{aligned} \tag{6.34}$$

From Eq. (6.34), several features can be concluded for this noise cancelling technique:

1) With an optimized $-A$, g_m will have no impact on $F_{total,o}$. Ideally, The noise contributed by the matching device can be entirely cancelled.

2) The noise contribution from R can not be cancelled. However, its impact can be attenuated by A_{total}.

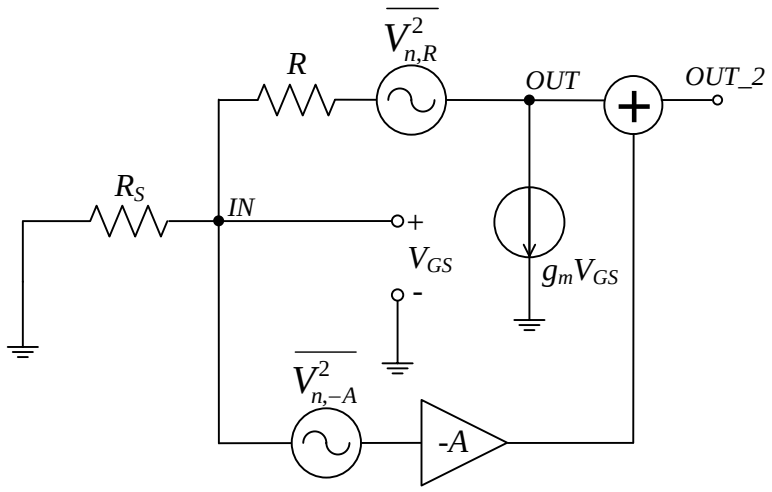

Figure 6.8: The equivalent circuit of Fig. 6.7 with noise sources of R and $-A$

3) With $A = A_o = 1 + R/R_s$, R should be maximized for minimizing F_{total}. The gain of LNA can also be increased with larger R value. However, increasing R will cause linearity degradation. Therefore, R should be optimized for different R_s.

4) $F_{total,o}$ is lower bounded by $min(F_{total,o}) = 1 + R_s/4R$ when $\overline{V_{n,-A}^2} = 0$. Compared to the conventional single stage LNA, the noise factor of the LNA circuit can be designed lower than 2.

5) The LNA can achieve a moderate gain and a wide impedance matching bandwidth at the same time. As the LNA essentially uses the resistive impedance matching method, the impedance matching bandwidth is not limited by capacitive or inductive components. Moreover, the gain of the LNA is the linear summation of the matching stage and the $-A$ stage, which is usually higher than general single stage LNAs.

The circuit implementation of the noise cancelling LNA is shown in Fig. 6.9. $M1$ and $M2$ are the matching devices. For input impedance matching, $g_{m1} \parallel g_{m2}$ is adjusted to be equal

to $1/R_s$. R_1 is the feedback resistor R. $M3$ and $M4$ forms the noise cancelling network which fulfill the $-A$ gain stage and perform the addition of the two signals (Fig. 6.8). Obviously, the gain of $-A$ amplifier is equal to g_{m4}/g_{m3}. As mentioned before, R needs to be maximized to improve F_{total}. Therefore, in order to achieve $A = A_o = 1 + R/R_s$, g_{m3} should be much smaller than g_{m4}. However, with the same bias I_d, smaller g_{m3} leads to a larger overdrive voltage on $M3$, by which the V_{ds} of $M4$ will be pushed too low and the linearity of the LNA will therefore degrade. To address this problem, a PMOS $M5$ is added to bypass some portion of I_{d4} such that the required value of g_{m3} can be reached without sacrificing linearity performance.

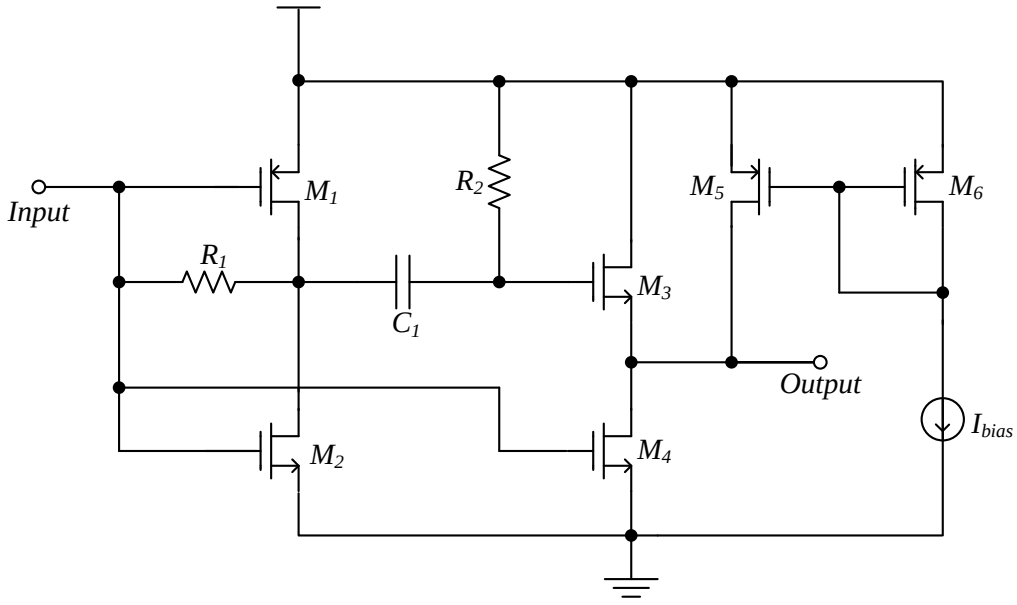

Figure 6.9: The wideband LNA.

6.1.4 Pre-amplifier

Each of the LNAs is followed by an open loop pre-amplifier (pre-amp) that has a $30dB$ fixed gain and fairly low additive noise to further guarantee the noise factor of the whole system.

This pre-amp has the full differential configuration. The circuit structure is the same as the LNA shown in Fig. 6.3, but with a shrunk size and reduced power consumption, because the noise performance of pre-amps is not as critical as LNAs. Since the 50Ω LNA has a single-ended structure, another function of the pre-amp for this type of LNAs is to convert the single-ended signal into differential signals for downstream signal processing.

6.2 VGA Design

In this design, the VGA circuit is realized by an opamp-based close loop amplifier. As well known, close loop amplifiers have high linearity and accurate controllable gain. Four stages of the VGA are cascaded. Each stage has two gain control bits that tune the gain between 0 to $18dB$ ($Gain = 0 \sim 8$). The simplified schematic for each stage is shown in Fig. 6.10. The gain can be tuned by changing R_{fb}.

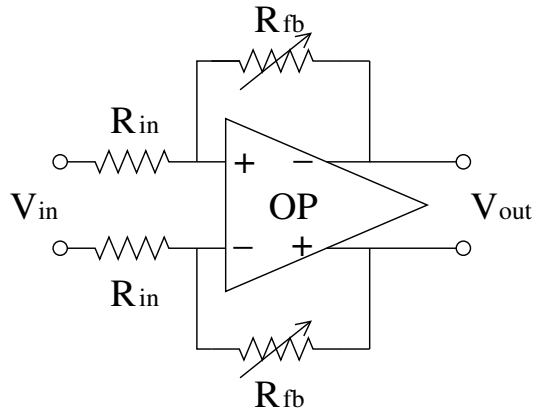

Figure 6.10: The VGA

6.3 LNA Experiment Results

6.3.1 The 50Ω LNA

This LNA is designed to achieve $30dB$ gain and less than $3dB$ noise figure through $500kHz$ to $6MHz$. It should be noted that the noise figure is computed with the source resistance, $R_s = 50\Omega$. Meanwhile, the input impedance is 50Ω to match the NQR and RFI probe output impedance. The simulation result is shown in Fig. 6.11. When the input signal frequency is $4MHz$, the gain of the LNA is $30.2dB$; and the noise figure can reach as low as $1.922dB$.

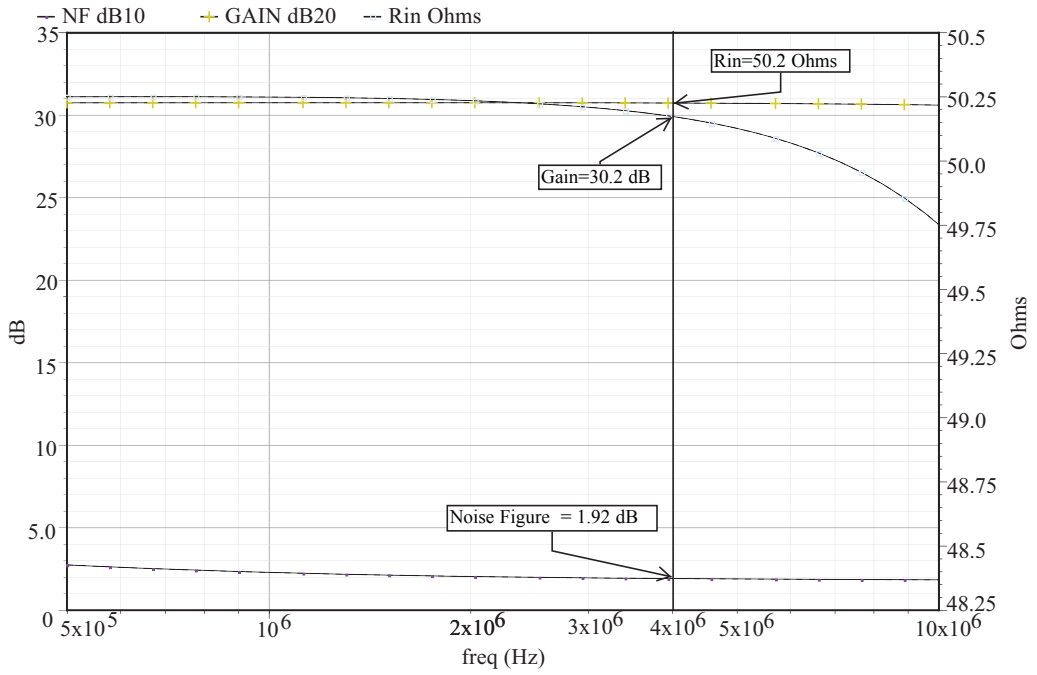

Figure 6.11: The noise figure and gain of the NQR and RFI LNAs

In order to compare the absolute noise contribution between the 50Ω LNA and infinite impedance LNA, the input referred noise is simulated. The result is shown in Fig. 6.12. We can see that this LNA circuit configuration has very low input referred noise, which is lower

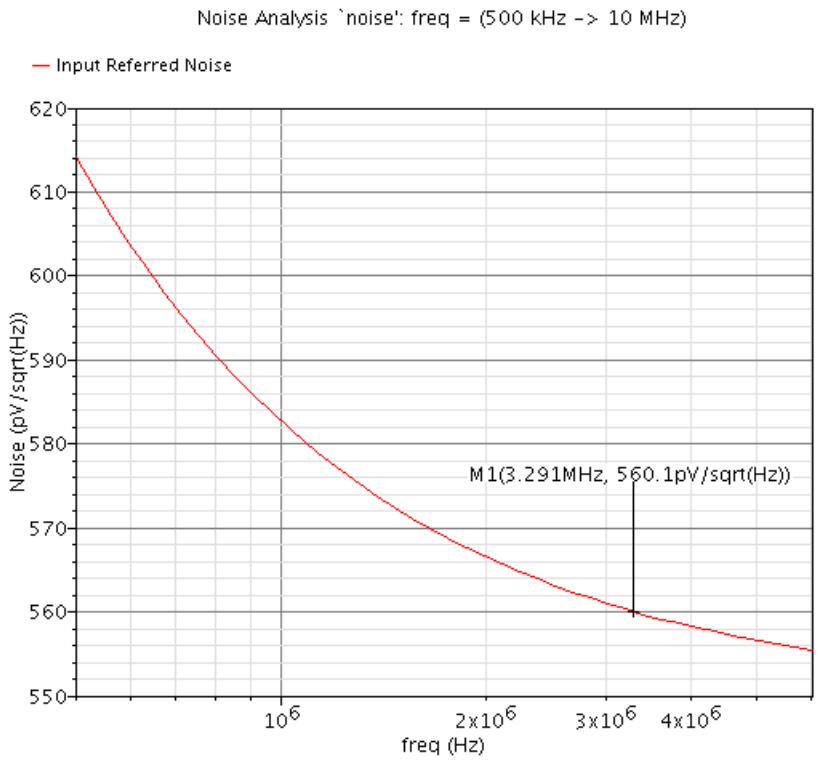

Figure 6.12: Input referred noise of the 50Ω LNA

than 620 $pV/\sqrt{Hz}$ from $500kHz$ to $6MHz$.

For the measurement on the real circuit, the LNA is evaluated together with the pre-amplifier. The simulation shows that the total gain of the LNA and pre-amplifier together should be $60dB$. The measured gain is around $46dB$. The reason is that both of the LNA and pre-amplifier are open loop gain stages. In general, due to the process variation, the gain of open loop amplifiers may vary a lot. This gain degradation is acceptable for the system as some margin is already reserved during the design phase.

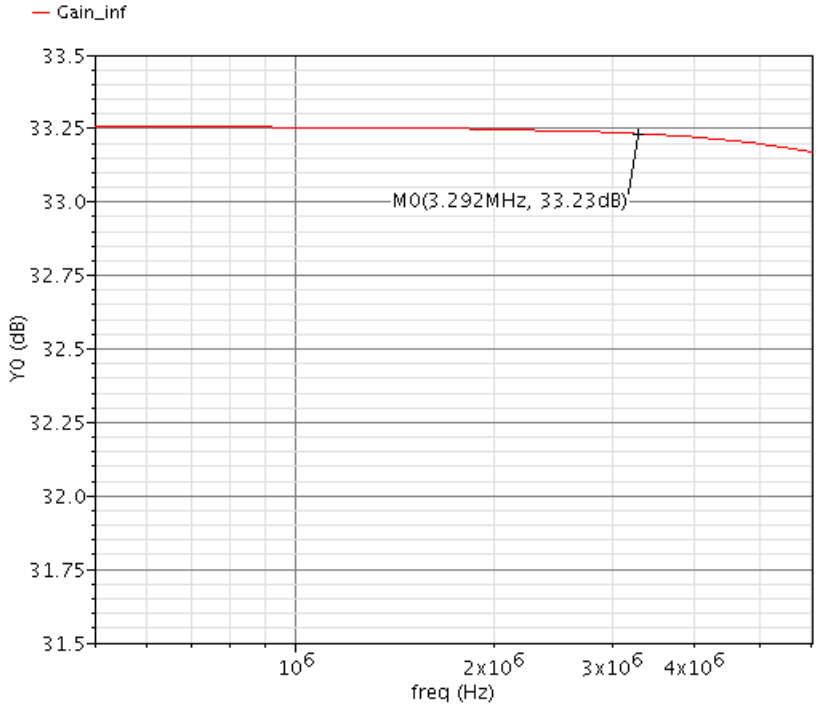

Figure 6.13: Gain of the infinite impedance LNA

6.3.2 The Infinite Impedance LNA

The simulated gain of the infinite impedance LNA is shown in Fig. 6.13. In the NQR signal frequency range, $500kHz$ to $6MHz$, this LNA is designed to have $33dB$ gain. With additional 30dB provided by the pre-amplifier, the total gain is designed to be 63dB. However, same with the 50Ω LNA, due to the process variation, the measured gain of the infinite impedance LNA and its following pre-amplifier is $50.3dB$.

Fig. 6.14 shows the input referred noise of the infinite impedance LNA. Comparing this LNA to the 50Ω LNA without the power matching network, noise contribution of this LNA is relatively larger.

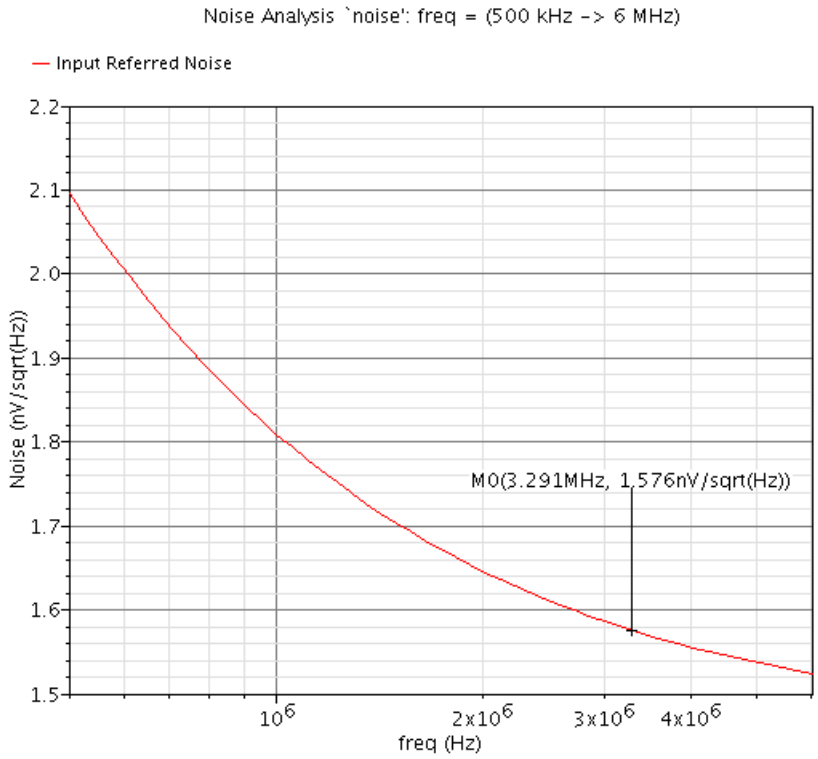

Figure 6.14: Input referred noise of the infinite impedance LNA

6.3.3 Noise Performance Comparison between Two Power Matching Schemes

A simulation experiment is designed in order to evaluate the noise performance difference between two power matching schemes. Each LNA is connected to an NQR probe with the corresponding power matching network. The NQR coil is identical for both NQR probes. It has the inductance $L = 2.63\mu H$ and the series resistance $R = 0.607\Omega$. For both power matching networks, the resonant frequency $f_o = 3.3MHz$ is used for the evaluation. $3.3MHz$ is the NQR frequency of HMT. For the 50Ω LNA, the 50Ω matching network shown in Fig. 5.1 (a) is used wherein $C_1 = 8.7nF$ and $C_2 = 0.98nF$. For the infinite impedance LNA, the

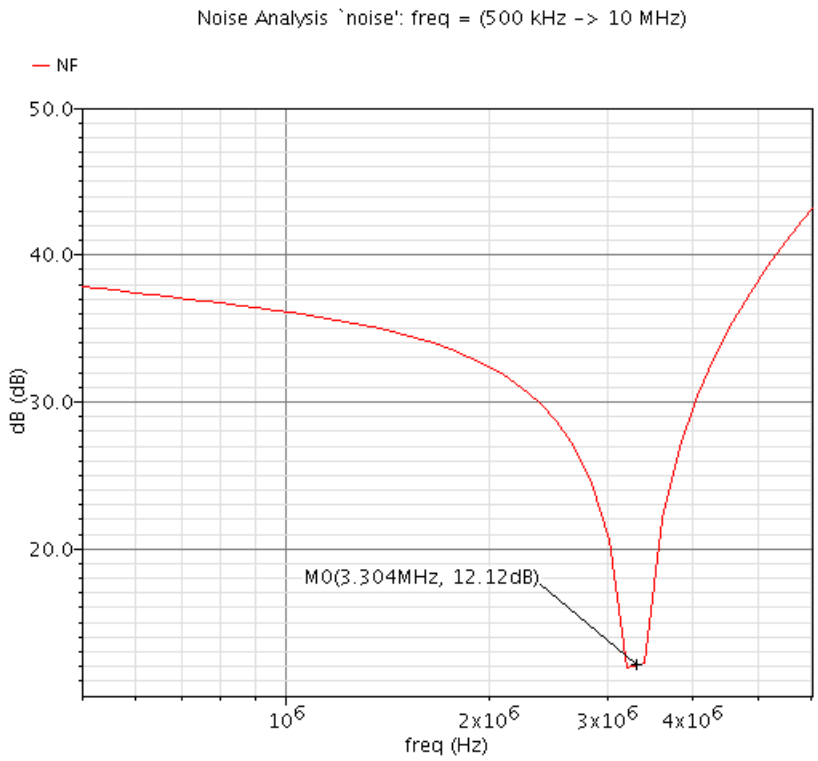

Figure 6.15: The noise figure of the 50Ω LNA with the power matching network

matching network shown in Fig. 5.1 (b) is used wherein the resonance capacitor C is equal to $883pF$.

In this experiment, the noise power of the LNA is referred back to the NQR coil, and compared with noise contribution of the coil's series resistance to compute the noise figure. The noise figure of the 50Ω LNA with its corresponding matching network is shown in Fig. 6.15. The noise figure of the infinite impedance LNA with its corresponding matching network is shown in Fig. 6.16. At the resonant frequency of the NQR probe, the noise figure is around $12dB$ for the 50Ω LNA with its corresponding power matching network. On the contrary, the infinite impedance LNA can achieve around $0.4dB$ noise figure even though this LNA itself has relatively larger noise contribution than the 50Ω LNA. Comparing the noise

figure results of the two power matching schemes, it can be seen that infinite impedance power matching scheme has much better noise performance than the 50Ω power matching scheme.

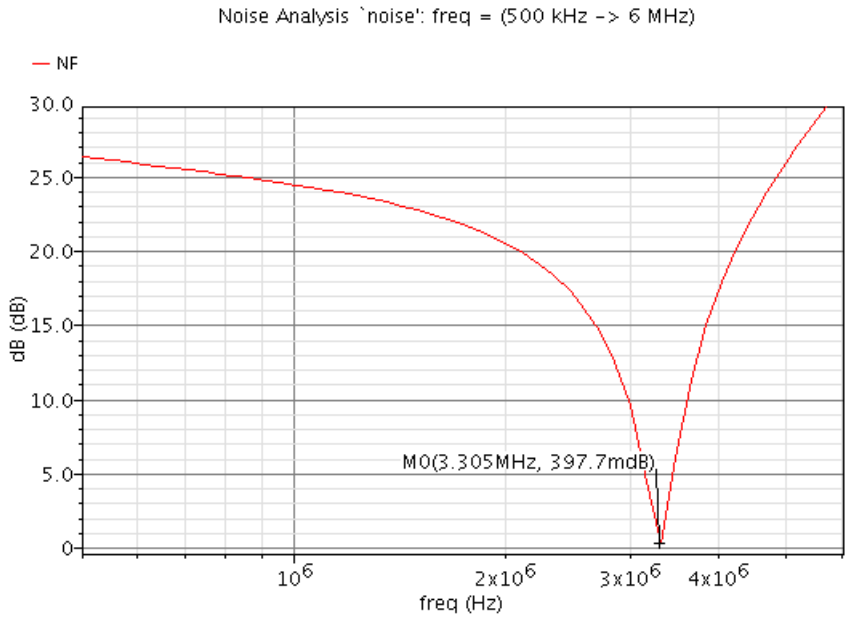

Figure 6.16: Noise Figure of infinite impedance LNA with the power matching network

6.4 Conclusion

In this chapter, the amplification circuit designs, including LNAs and VGA, of the receiver section are presented. In particular, both of the 50Ω input impedance LNA and infinite input impedance LNA circuits are discussed. The detailed noise analysis and corresponding circuit implementation considerations are described. With the adopted circuit configuration, the LNAs can achieve a low noise figure that is required for NQR detection systems.

Some measurement issues are found during the real circuit tests. First, measured gains of the LNAs have a large deficit from the designed value due to the process variation. Although a margin is reserved for the gains of the LNAs during the design phase, the robustness of the circuit design needs to be enhanced. The second issue is that the noise performance of the LNAs cannot be accurately measured with the given equipment.

Chapter 7

Receiver Hardware Configuration II: Analog Adaptive Filter for RFI Mitigation

According to United States frequency allocation chart, the NQR signal frequency range for explosives, $500kHz$ to $6MHz$, overlaps the commercial AM radio broadcasting range from $500kHz$ to $1600kHz$, and some mobile communication bands from $1600kHz$ to $6MHz$. As a result, RFI from these radio stations becomes the largest corruption source for NQR signal detection. Precautions are required to be taken to mitigate the impact from RFI. As mentioned before, for the lab equipment and the stationary detection systems, shielding is a good method to isolate the NQR probe from RFI. For field applications where shielding the probe with a metal case is infeasible, some noise cancelling techniques should be adopted to electronically suppress the RFI that is picked up by the NQR probe. One common method to that end is to use an auxiliary probe, which is kept away from the detection scene and the NQR probe, to only pick up the RFI signal, and subtract it from the NQR probe signal with a certain transformation. Obviously, the requirement to make this method work is

that the RFI signal captured by the RFI probe has to correlate with the RFI signal on the NQR probe. As depicted in Chapter 3.1, RFI can be characterized by far-field and near-field signal models. In both models, the RFI signals on the RFI and NQR probes have the spacial correlation.

In this work, an analog adaptive filter is employed to achieve the RFI mitigation. Some novel circuit design ideas are proposed and implemented in the adaptive filter circuit: 1) a new continuous-time weight-updating circuit topology with cascaded auto-zeroing DC offset cancellation for both the multiplier and the integrator is proposed to improve the filter circuit's immunity to the component mismatches; 2) a multiplier with a novel auto-zeroing DC offset cancellation circuit is proposed, which can also be applied in other continuous-time signal processing applications. A 6-tap LMS adaptive filter using the proposed structure is integrated on the customized IC.

In this chapter, we will discuss the circuit configuration in detail. First, the background knowledge related to adaptive filters is reviewed. Next, the mathematical derivation for the RFI cancellation performance of the continuous-time LMS algorithm is presented. Also, the impact of DC offsets in the weight updating circuit on the interference cancellation performance is explained. Then, the circuit implementation is presented. Finally, some notes and conclusions regarding this adaptive filter is made to finish this chapter.

7.1 Background

Adaptive filters are a type of signal filtering systems which can tune themselves adaptively to transform the input signal into a desired shape. As adaptive filters are initially invented for digital signal processing applications, without loss of generality, the digital adaptive filters are used for the discussion at this stage. An adaptive filter usually has two input signals, $d[n]$ and $\mathbf{X}[n]$. $d[n]$ is called the desired signal which is used as a reference signal. $\mathbf{X}[n]$ is

the input signal to be reformed for closely matching $d[n]$. An adaptive filter consists of two main function modules, a filter and a adaptation block. The filtering part of the adaptive filter transforms $\mathbf{X}[n]$. The adaptation part, on the other hand, adaptively optimizes the filtering part such that the transformed $\mathbf{X}[n]$ is tuned to match $d[n]$. Based on the shape of the input signal $\mathbf{X}[n]$, the adaptive filters are roughly categorized into two types: the filters with a transversal delayed signal set, as shown in Fig. 7.1, and the filters with a spacial distributed signal set, as shown in Fig. 7.2. The transversal ones basically have a tapped delay line with m stages to produce a delayed signal set with a length equal to $m+1$, $\mathbf{X}[n] = x[n], x[n-1], \ldots, x[n-m]$. The spacial ones have a vector $\mathbf{X}[n]$ which contains $l+1$ elements, $\mathbf{X}[n] = x_0[n], x_1[n], \ldots, x_l[n]$.

In both types of filters, the weights of the filters, $\mathbf{W}[n] = w[n], w[n-1], \ldots$ are tuned by the adaptation part with a certain adaptive algorithm such that the accumulated output

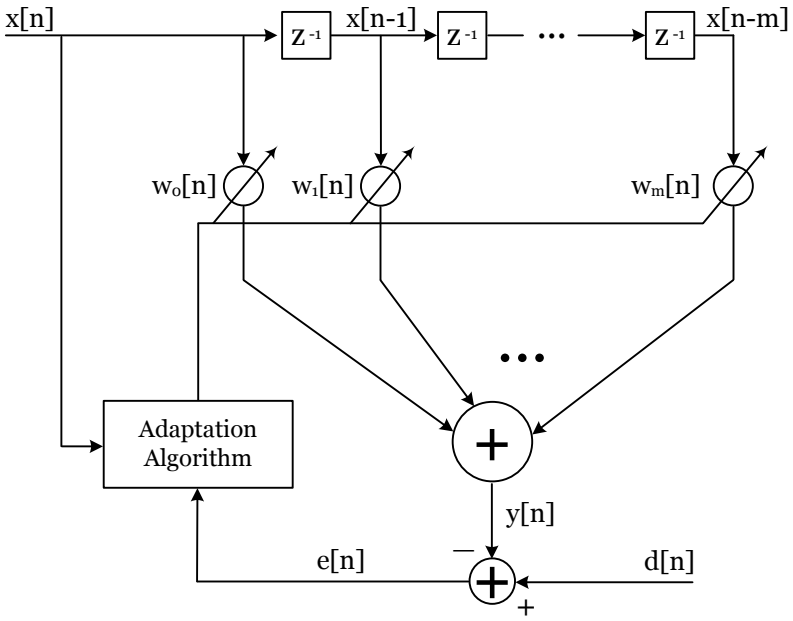

Figure 7.1: The adaptive transversal filter

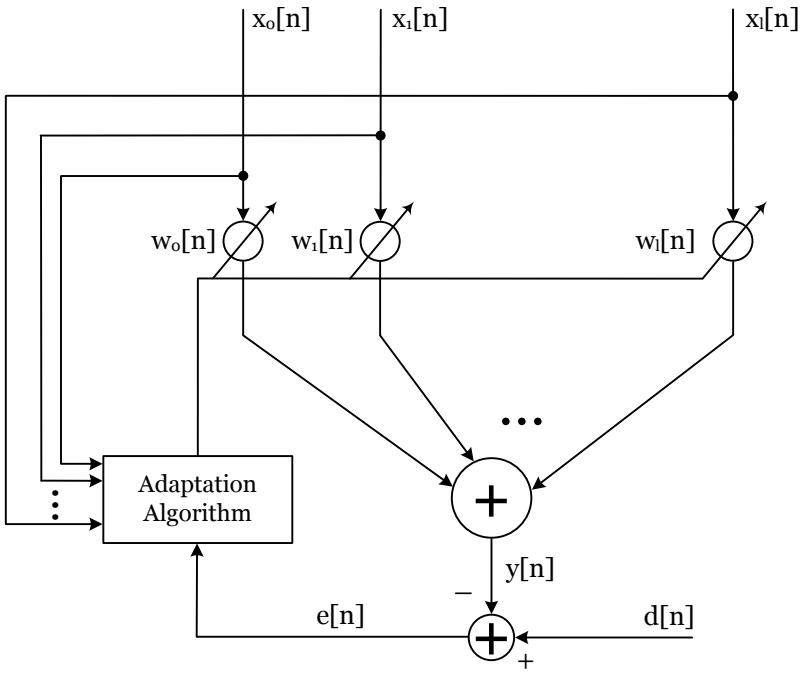

Figure 7.2: The adaptive spacial filter

signal $y[n]$ will approximate to $d[n]$. The accumulated output signal $y[n]$ can be calculated by

$$y[n] = \mathbf{W}[n] \cdot \mathbf{X}[n] = \sum_{i=0}^{m(orl)} x_i[n] w_i[n] \tag{7.1}$$

As a result, the Mean Square Error (MSE) between $y[n]$ and $d[n]$ should be minimized. By definition, MSE is equal to the expected power ξ of the error signal:

$$\xi = E[e^2[n]] = \frac{1}{N} \sum_{i=0}^{N} e^2[n] = \frac{1}{N} \sum_{i=0}^{N} (d[n] - y[n])^2 \tag{7.2}$$

where $e[n] = d[n] - y[n]$ is the error signal.

In late 1950's, Widrow and Hoff proposed an adaptive algorithm named Least Mean Square (LMS) [101]. The simplicity and efficiency of LMS make it the most popular mechanism for the adaptive filters. LMS is essentially a steepest-descent recursion algorithm [102].

The steepest-descent recursive method for updating the weights $\mathbf{W}[n]$ is to change them towards the fastest direction by which ξ descents. The updating function is:

$$\mathbf{W}[n+1] = \mathbf{W}[n] - \mu \nabla_{\mathbf{W[n]}} \xi. \tag{7.3}$$

In LMS, ξ is replaced by the instant evaluation function $\widehat{\xi} = e^2[n]$. Therefore, the weight updating function in Eq. (7.3) becomes:

$$\begin{aligned}
\mathbf{W}[n+1] &= \mathbf{W}[n] - \mu \nabla_{\mathbf{W}[n]} e^2[n] \\
&= \mathbf{W}[n] - 2\mu e[n] \nabla_{\mathbf{W}[n]} e[n] \\
&= \mathbf{W}[n] - 2\mu e[n] \nabla_{\mathbf{W}[n]} (d[n] - \mathbf{W}[n] \cdot \mathbf{X}[n]) \\
&= \mathbf{W}[n] + 2\mu e[n] \mathbf{X}[n]
\end{aligned} \tag{7.4}$$

Adaptive filters have been widely used in communication systems and sensor systems to fulfill channel equalization [100], noise and interference cancellation, system identification and the like. Basically, for the adaptive filter to work, a certain correlation between $x[n]$ and $d[n]$ should exist, and can be approximated by a linear system $H(z)$. The characteristic of the linear system is often unknown, and may vary from time to time. The adaptive filter adjusts the weights to approximately produce an inverse linear system $G(z) \approx H^{-1}(z)$ such that the MSE is minimized. Note that since adaptation is essentially a recursive process, time for convergence is required for the adaptive filter to settle. Hence, the changing speed of $H(z)$ must be considerably slower than the convergence speed of the adaptive filter.

In Fig. 7.3, an example is given to demonstrate the interference cancellation application of adaptive filters. $I_1[n]$ and $I_2[n]$ are the two RFI signals picked up by the signal receiving antenna and the RFI receiving antenna, respectively. The correlation between $I_1[n]$ and $I_2[n]$

is approximated by a transfer function $H(z)$. With $H(z)$, we have

$$\mathbf{I_2}(z) = H(z)\mathbf{I_1}(z). \tag{7.5}$$

where $\mathbf{I_2}(z)$ and $\mathbf{I_1}(z)$ are counterparts of $I_1[n]$ and $I_2[n]$ in the frequency domain, respectively. Besides $I_1[n]$, the signal receiving antenna also picks up the interested signal $s[n]$. The total received signal, $I_1[n] + s[n]$ is used as $d[n]$ in the adaptive filter. And $I_2[n]$ is used as $x[n]$. Then, the adaptive filter will produce a transfer function $G(z) \approx H^{-1}(z)$, and $y[n]$ in the frequency domain becomes

$$Y(z) = \mathbf{I_2}(z) \cdot G(z) \tag{7.6}$$

If substituting Eq. (7.5) in (7.6), we will have

$$Y(z) = \mathbf{I_2}(z) \cdot G(z) \approx H(z)\mathbf{I_1}(z)H^{-1}(z) = \mathbf{I_1}(z) \tag{7.7}$$

Hence, subtracting $y[n]$ from $d[n]$ results in the error signal $e[n] \approx s[n]$. As a result, the RFI is suppressed.

For low frequency signals, digital adaptive filtering performs nicely because of its convenient implementation and programmable nature. Alternatively, discrete-time analog adaptive filtering is also an attractive option because it does not need an ADC, and is power efficient compared to its digital counterpart. Many variant algorithms of LMS digital and discrete-time analog adaptive filters, such as variable-step LMS, normalized LMS and signed LMS, have been proposed to improve the adaptive filtering performance. However, due to the sampling speed limitation, digital and discrete-time analog adaptive filters are infeasible for high frequency applications. Thus, continuous-time analog adaptive filters become the solution for this requirement [103].

7.2 Continuous-time LMS Algorithm and Effects of DC Offsets

In the past few decades, a wealth of research effort has been devoted to the study of continuous-time LMS (CTLMS) adaptive filters. First, in order to carry the input signal information more efficiently, [104] and [105] proposed several filter structures to generate input vectors in a transversal filter. Then, in [106], the authors investigated the factors that affect the performance of CTLMS, and claimed that the performance of CTLMS is mostly restricted by the DC offsets from the weight-updating multiplier and integrator. To address this problem, [107] proposed to use a MOSFET-C integrator with a auto-zeroing mechanism to cancel the DC offsets from the multiplier and integrator. However, when this concept is to be implemented in the sub-micron CMOS process with a low power supply, the residual DC offsets after auto-zeroing cancelling become noticeable, and then compromise the filtering

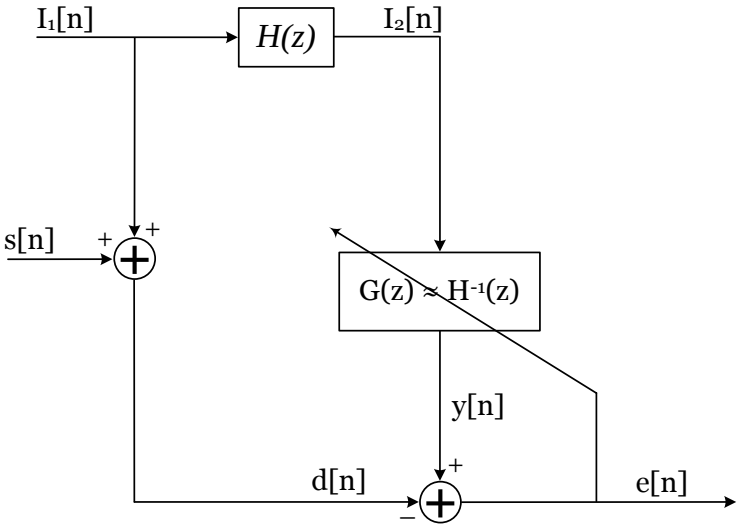

Figure 7.3: Interference cancellation with an adaptive filter

performance.

First, the derivation of CTLMS is discussed. It is similar to that of its digital counterpart. A tapped delay transversal continuous-time analog LMS adaptive filter, which is configured as an interference canceller is shown as Fig. 7.4. All signals in Fig. 7.4 are real-valued continuous signals. $d(t)$ is the desired signal that consists of an interference signal and an interested signal. $x(t)$ is called the reference signal which contains the transformed interference. It should be noted that the interference signals in $d(t)$ and $x(t)$ remain correlated such that the adaptive filter can suppress the interference signal without comprising the interested signal. First, $x(t)$ is fed into a delay line to generate $\mathbf{X}(t)$. The resulting $\mathbf{X}(t)$ is

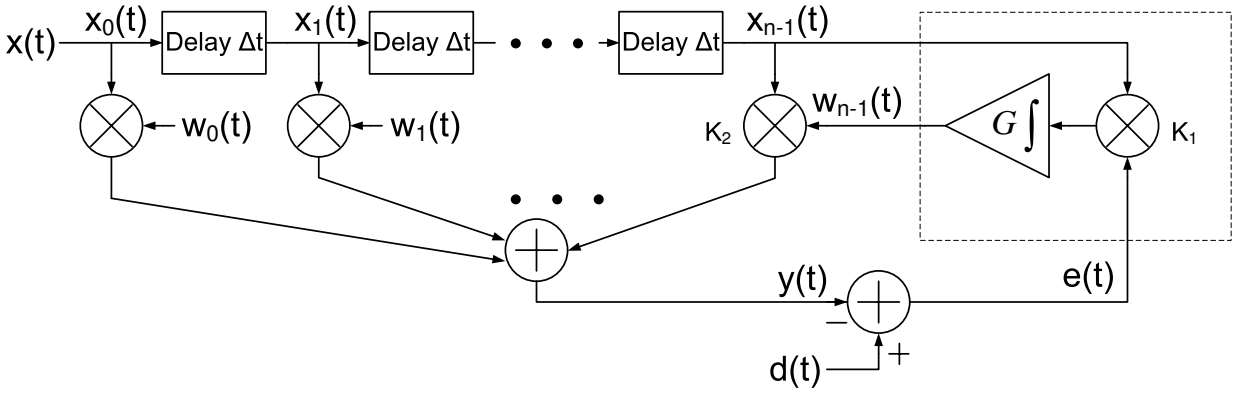

Figure 7.4: The tapped delay CTLMS filter.

$$\mathbf{X}(t) = [x_0(t), x_1(t), \cdots, x_{n-1}(t)]^T \tag{7.8}$$

where $x_i(t) = x(t - i \cdot \Delta t)$. Δt is the delay time of each delay unit. Note that $\mathbf{X}(t)$ does not have to be generated by a tapped delay line. As long as $\mathbf{X}(t)$ carries sufficient information of the reference signal, it can be generated in many ways. For instance, by putting $x(t)$

through a quadrature hybrid circuit, an in-phase component and a quadrature component form the reference signal vector $\mathbf{X}(t) = \left[x(t), Real\left\{x(t)e^{j\frac{\pi}{2}}\right\}\right]$ [103]. The tapped delay-line can also be replaced by a set of Laguerre filters [105].

The filtered signal $y(t)$ is

$$y(t) = \mathbf{W}^T(t)\mathbf{X}(t) \tag{7.9}$$

where $\mathbf{W}(t)$ is the weight vector of the adaptive filter:

$$\mathbf{W}(t) = K_2 \cdot [w_0(t), w_1(t), \cdots, w_{n-1}(t)]^T \tag{7.10}$$

The superscript T indicates the transposition of a vector. K_2 is the gain of the weight-times-reference multiplier, which will be referred to as K_2 multiplier in the rest of this chapter.

The error signal, $e(t) = d(t) - y(t)$, is the resulting signal of the interference canceller. The performance of the adaptive filter is evaluated by MSE, ξ, which is [108]:

$$\begin{aligned} \xi &= E\left[e^2(t)\right] \\ &= E\left[d^2(t)\right] - 2\mathbf{P}^T(t)\mathbf{W}(t) + \mathbf{W}^T(t)\mathbf{R}(t)\mathbf{W}(t) \end{aligned} \tag{7.11}$$

where $\mathbf{P}(t) = E\left[d(t)\mathbf{X}(t)\right]$ and $\mathbf{R}(t) = E\left[\mathbf{X}(t)\mathbf{X}^T(t)\right]$. Hence, the corresponding optimal Wiener solution of the weights, which leads to the minimum MSE, can be obtained by letting $\bigtriangledown_{W(t)}\xi = 0$. Thus,

$$\mathbf{W}_{opt} = \mathbf{R}^{-1}(t)\mathbf{P}(t). \tag{7.12}$$

In order to make $\mathbf{W}(t)$ converge to $\mathbf{W}_{opt}$, The LMS adaptive algorithm is employed to update the weights:

$$\frac{d\mathbf{W}(t)}{dt} = -\frac{\mu}{2} \bigtriangledown_{\mathbf{W}(t)} e^2(t) \tag{7.13}$$

which leads to

$$\mathbf{W}(t) = \mu \int_{-\infty}^{t} e(\tau)\mathbf{X}(\tau)d\tau \tag{7.14}$$

$\mathbf{W}(t)$ is approaching $\mathbf{W}_{opt}$ at a rate that is controlled by μ for a given input autocorrelation matrix [108]. Based on the configuration in Fig. 7.4, Eq. (7.14) can be rewritten as

$$\mathbf{W}(t) = K_2 G K_1 \int_{-\infty}^{t} e(\tau)\mathbf{X}(\tau)d\tau \tag{7.15}$$

where K_1 is the gain of the error-times-reference multiplier, which will be referred to as K_1 multiplier in the rest of this chapter. G is the gain of the integrator. Therefore, the total loop gain is $\mu = K_2 G K_1$. When $\mathbf{W}(t)$ converges to $\mathbf{W}_{opt}$ and oscillates around this optimal value, assuming it occurs at $t = t_o$, the adaptive filter is in the steady state. In this situation,

$$E\left[\triangle\mathbf{W}(t)\right] = E\left[\mathbf{W}(t) - \mathbf{W}_{opt}\right] = \frac{1}{t - t_o} K_2 G K_1 \int_{t_o}^{t} e_{opt}(\tau)\mathbf{X}(\tau)d\tau = 0, \quad t \to \infty \tag{7.16}$$

MSE reaches the minimum value,

$$E[e_{opt}^2(t)] = \xi_o = E\left[\left(d(t) - \mathbf{W}_{opt}^T \mathbf{X}(t)\right)^2\right] \tag{7.17}$$

While the LMS algorithm is implemented in circuits with CMOS technologies, the most serious design issue is how the DC offsets on the K_1 multiplier and the integrator are suppressed to maintain the ideal operation of the adaptive filter. These DC offsets are mainly caused by the input transistor mismatch. If the input DC offset from K_1 multiplier of the i^{th} stage is denoted as $M_{i,in}$, and the input DC offset of the integrator is denoted as $I_{i,in}$, the new weight-updating function can be written as

$$w_i(t) = G K_2 \int_{-\infty}^{t} \left(K_1 e(\tau) x_i(\tau) + K_1 M_{i,in} + I_{i,in}\right) d\tau. \tag{7.18}$$

Similarly, when the adaptive filter reaches the steady state,

$$E\left[\triangle w_i(t)\right] = E\left[w_i(t) - w_{i,opt\_off}\right]$$
$$= \frac{1}{t-t_o} GK_2 \int_{t_o}^{t} \left(K_1 e_{opt\_off}(\tau) x_i(\tau) + \phi_i\right) d\tau = 0, \quad t \to \infty \tag{7.19}$$

where w_{i,opt_off} is the i_{th} element of the optimal weight vector $\mathbf{W}_{opt\_off}$, with the presence of the DC offset $\phi_i = K_1 M_{i,in} + I_{i,in}$ on the i^{th} weight-updating stage. e_{opt_off} is the steady state error signal with the presence of the DC offset. As ϕ_i is constant, Eq. (7.19) can be written as:

$$E[e_{opt\_off}(t) x_i(t)] = \frac{1}{t-t_o} \int_{t_o}^{t} e_{opt\_off}(\tau) x_i(\tau) d\tau$$
$$= -\frac{\phi_i}{K_1} \tag{7.20}$$

It can be rewritten with vector calculation:

$$E[e_{opt\_off}(t)\mathbf{X}(t)] = E\left[(d(t) - \mathbf{W}_{opt\_off}\mathbf{X}(t))\mathbf{X}(t)\right]$$
$$= -\frac{\mathbf{\Phi}}{K_1} \tag{7.21}$$

where $\mathbf{\Phi} = [\phi_0(t), \phi_1(t), \cdots, \phi_{n-1}(t)]^T$. Meanwhile, assuming that the difference, $\Delta\mathbf{W}_{opt}$, between $\mathbf{W}_{opt\_off}$ and $\mathbf{W}_{opt}$ due to the DC offset is much smaller than $\mathbf{W}_{opt}$ and independent of t. A linear approximation of $\mathbf{W}_{opt\_off}$ is:

$$\mathbf{W}_{opt\_off} = \mathbf{W}_{opt} + \Delta\mathbf{W}_{opt} \tag{7.22}$$

Bringing Eq. (7.22) back to Eq. (7.21), we will have

$$E\left[\left(d(t)-\mathbf{W}_{opt}^{T}\mathbf{X}(t)-\Delta\mathbf{W}_{opt}^{T}\mathbf{X}(t)\right)\mathbf{X}(t)\right]=-\frac{\mathbf{\Phi}}{K_1}$$

$$\underbrace{E\left[\left(d(t)-\mathbf{W}_{opt}^{T}\mathbf{X}(t)\right)\mathbf{X}(t)\right]}_{=0,\ according\ to\ Eq.\ (7.16)}-\underbrace{E\left[\mathbf{X}(t)\mathbf{X}^{T}(t)\right]}_{=\mathbf{R}}\Delta\mathbf{W}_{opt}=-\frac{\mathbf{\Phi}}{K_1}$$

$$\Delta\mathbf{W}_{opt}=\frac{\mathbf{R}^{-1}\mathbf{\Phi}}{K_1} \tag{7.23}$$

Then, the MSE ξ_{off} with DC offset is:

$$\begin{aligned}\xi_{off}&=E[e^2(t)]\\&=E[(\underbrace{d(t)-\mathbf{W}_{opt}^{T}\mathbf{X}(t)}_{e_{opt}(t)}-\Delta\mathbf{W}_{opt}^{T}\mathbf{X}(t))^2]\\&=E\left[e_{opt}^2(t)\right]-\underbrace{2\Delta\mathbf{W}_{opt}^{T}E\left[e_{opt}(t)\mathbf{X}(t)\right]}_{=0,\ according\ to\ Eq.\ (7.16)}+\Delta\mathbf{W}_{opt}^{T}\underbrace{E[\mathbf{X}(t)\mathbf{X}^{T}(t)]}_{=\mathbf{R}}\Delta\mathbf{W}_{opt}\\&=\xi_o+\frac{1}{K_1^2}\mathbf{\Phi}^{T}\mathbf{R}^{T}\mathbf{\Phi}\end{aligned} \tag{7.24}$$

Therefore, the excess MSE introduced by DC offset of the weight-updating circuit is:

$$\xi_{excess}=\xi_{off}-\xi_o=\frac{1}{K_1^2}\mathbf{\Phi}^{T}\mathbf{R}^{T}\mathbf{\Phi} \tag{7.25}$$

According to Eq. (7.25), we can see that ξ_{excess} depends on not only the DC offset $\mathbf{\Phi}$ but also the signal correlation matrix $\mathbf{R}$. That can be seen from the perspective of circuit design. If the input signal $\mathbf{X}(t)$ has higher amplitude, which leads to bigger $\mathbf{R}$, the signal swing at the input of the integrator is larger such that the impact of DC offset is attenuated.

In addition, with bringing $\mathbf{\Phi} = K_1\mathbf{M}_{in} + \mathbf{I}_{in}$ into Eq. (7.25), it can be rewritten as:

$$\xi_{excess} = \frac{1}{K_1^2}\mathbf{\Phi}^T\mathbf{R}^T\mathbf{\Phi} = \mathbf{M}_{in}^T\mathbf{R}^T\mathbf{M}_{in} + \frac{1}{K_1^2}\mathbf{I}_{in}^T\mathbf{R}^T\mathbf{I}_{in} \tag{7.26}$$

Eq. (7.26) implies that the effect of $\mathbf{I}_{in}$ can be reduced by increasing K_1. On the contrary, the input referred offset of K_1 multiplier, $\mathbf{M}_{in}$, will directly incur performance degradation to the adaptive filter. Therefore, a DC offset cancellation scheme is required for the weight-updating circuit.

7.3 Circuit Design

To implement the continuous-time LMS adaptive algorithm, several circuit modules need to be designed. From Fig. 7.4, we can see that these modules include a delay unit circuit, a weight-updating circuit and a summation circuit. In particular, the weight-updating circuit needs to have the DC-offset cancellation function to improve the adaptive filter's performance.

7.3.1 Delay Unit Circuit

The tapped delay unit in the filter is realized by an all-pass filter with fixed group delay. The first order all-pass filter can be characterized as:

$$H(j\omega) = \frac{1 - j\omega/\omega_o}{1 + j\omega/\omega_o} \tag{7.27}$$

The group delay of the all-pass filter is:

$$t_g = \frac{d\angle H(j\omega)}{d\omega} = \frac{2/\omega_o}{1 + (\omega/\omega_o)^2} \tag{7.28}$$

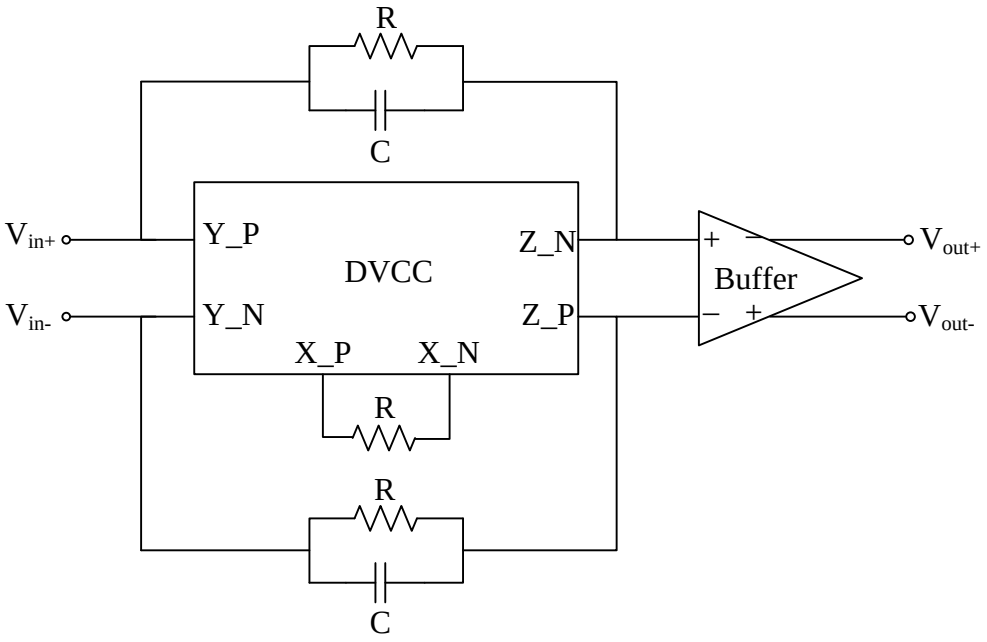

Figure 7.5: The tapped delay unit

When $(\omega/\omega_o)^2 \ll 1$, the group delay is approximately a fixed value, which is $t_g = 2/\omega_o$. Note that the group delay must not be greater than the period of the highest frequency component. Otherwise, if the RFI signal has a period equal to the group delay, the adaptive filter can not be optimized to mitigate the RFI. In this design, a Differential Voltage Current Conveyor (DVCC) based first order all-pass filter [110] is used as the tapped delay unit. The simplified circuit of the all-pass filter is illustrated as Fig. 7.5. The terminal characteristics of a DVCC are described as:

$$\begin{aligned} V_{Y\_P} - V_{Y\_N} &= V_{X\_P} - V_{X\_N} \\ I_Y &= 0 \\ I_X &= I_Z \end{aligned} \tag{7.29}$$

With the structure shown in Fig. 7.5, the transfer function of the filter is:

$$H(j\omega) = \frac{V_{out}}{V_{in}} = \frac{1 - j\omega CR}{1 + j\omega CR} \tag{7.30}$$

Therefore, when $(\omega RC)^2 \ll 1$, the group delay, in other words, the time delay is $t_{delay} = 2RC$.

Fig. 7.6 shows the simplified circuit of DVCC. $M1$, $M2$, $M3$ and $M4$ form a feedback loop to guarantee that $V_X = V_Y$. R_{fb} and C_{fb} is the Miller feedback network to stabilize the loop. $M1$ and $M7$ form a pair of current mirror through which I_X is duplicated over to generate I_Z.

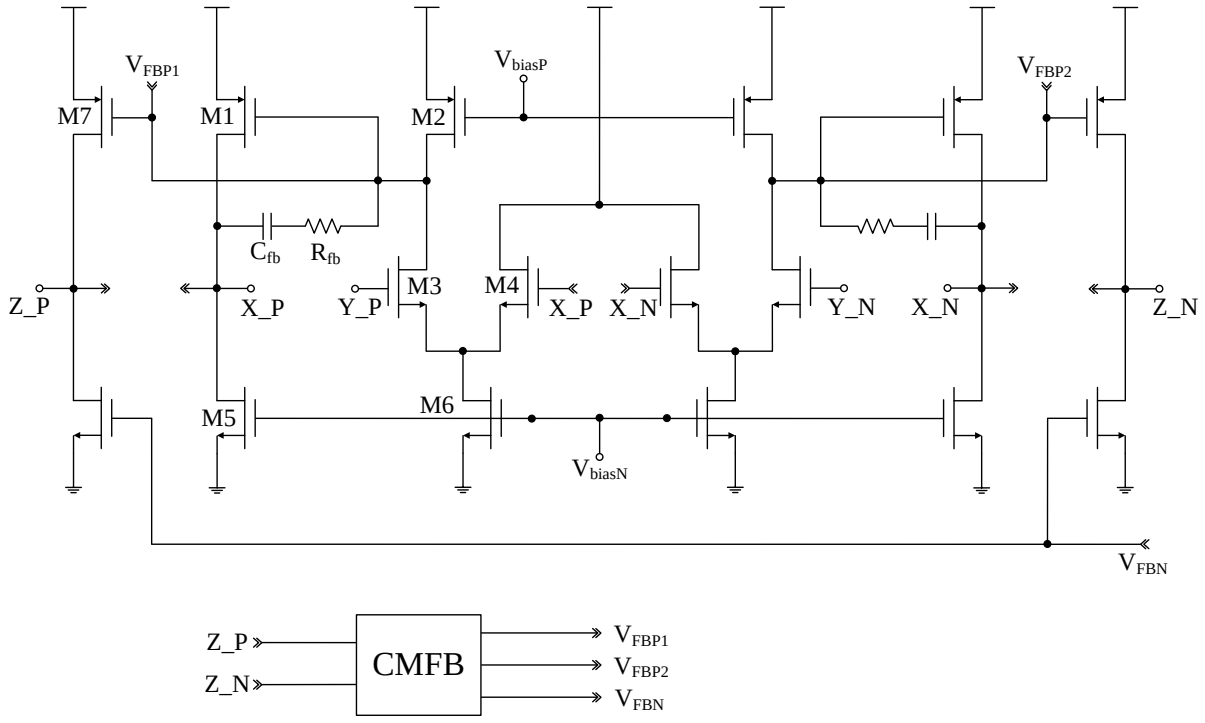

Figure 7.6: The differential voltage current conveyor (DVCC)

7.3.2 CMOS Weight-Updating Circuit

The proposed weight-updating circuit is shown in Fig. 7.7. This circuit employs a fully differential structure to eliminate the common-mode noise corruption. It consists of two main modules, a V_{GS}^2 based multiplier and a MOSFET-C integrator. Both of them have auto-zeroing circuits to cancel the input referred DC offsets.

During the normal weight-updating operation, ϕ_1 switches select the error signal V_e and the reference signal V_{xi} as the inputs of the multiplier. The feedback capacitors C_5 and C_6, where $C_5 = C_6 = C$, are connected with the OPAMP to form the MOSFET-C integrator. Meanwhile, ϕ_2 and ϕ_3 switches are open. MOSFETs $M1$ and $M2$ have small W/L ratios with long channel lengths. They work in the deep triode region as high-valued resistors R_{ds}, whose values are controlled by the gate voltage V_{CNTL}. The gain of the integrator, G in Fig. 7.4, is equal to $1/(R_{ds} \cdot C)$.

When the circuit operates in the auto-zeroing mode, first, ϕ_1 switches connect all inputs of the multiplier to the reference voltage V_{REF}. Also, the feedback capacitors of the integrator are disconnected. The integrator is working in the open loop mode. Since the inputs are zeroed, the differential output signal of the multiplier is only the output offset. Then, ϕ_3 switches are closed. The offset is amplified by the error amplifier and corrected by storing a voltage difference in capacitors C_1 and C_2. Note that after the DC offset cancellation of the multiplier, some residual offset, due to the finite gain of the error amplifier, will appear at the input of the integrator. Now, ϕ_3 switches are opened, and ϕ_2 switches are closed. The total output DC offset of the integrator, which results from the inherent DC offset of the integrator and the aforementioned residual offset from the multiplier, is corrected by storing a voltage difference in capacitors C_3 and C_4.

The frequency of repeating the auto-zeroing operation is mostly restricted by the charge leaking speed of capacitors C_1, C_2, C_3 and C_4. For most of the current CMOS technologies,

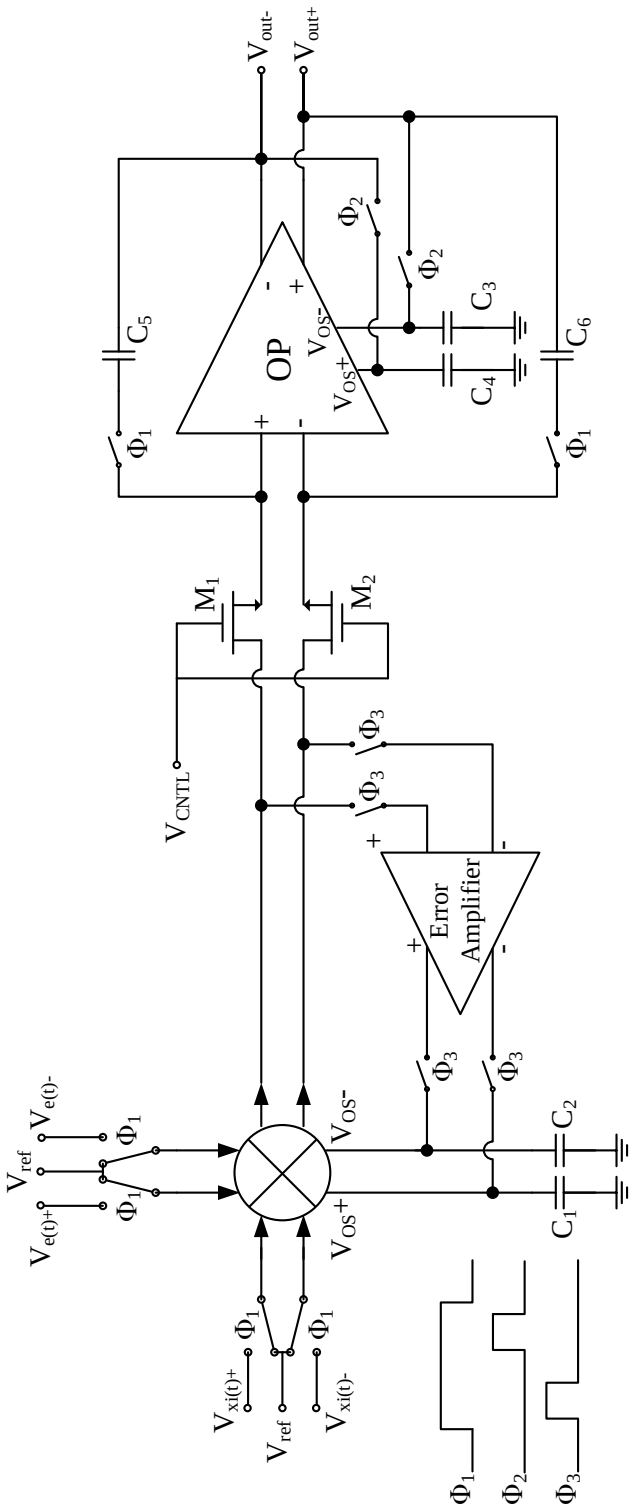

Figure 7.7: The auto-zeroed weight-updating circuit

the capacitors can hold the charge for several hundred milliseconds. The auto-zeroing operation can be accomplished in several microseconds. Thus, the frequency of the auto-zeroing operation can be tens of Hz with a duty circle less than 1%. This is acceptable for most applications. The cascaded DC offset cancellation circuit for both the multiplier and integrator is one of the main contributions in this work.

7.3.2.1 V_{GS}^2 Multiplier for Auto-zeroing Offset Cancellation

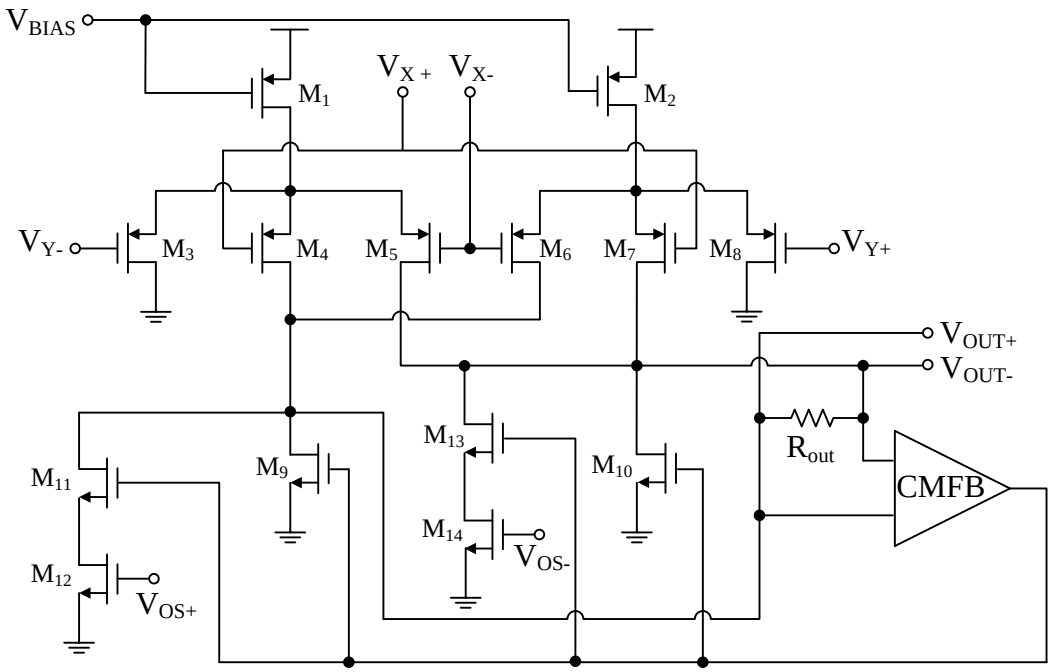

Figure 7.8: The V_{GS}^2 multiplier ($K1$ multiplier) for auto-zeroing offset cancellation

Fig. 7.8 is the schematic of the multiplier employed in this design. Transistors $M1$–$M8$ construct a voltage-to-current quadruple V_{GS}^2 multiplier, which is well known by its wide dynamic input range and good linearity [109]. $M1$ and $M2$ provide the bias current. $M3$ and $M8$ work as source followers to ensure the source voltage of $M4$–$M7$ follows the change

on V_{Y-} and V_{Y+}. Then, the output voltages and currents are

$$\begin{aligned} V_{OUT+} &= I_{OUT+} \cdot \frac{1}{2} \cdot R_{OUT} \\ I_{OUT+} &= K(V_{X+} - V_{Y-})^2 + K(V_{X-} - V_{Y+})^2 \\ &= KV_{X+}^2 + KV_{X-}^2 + KV_{Y+}^2 + KV_{Y-}^2 - 2KV_{X+}V_{Y-} - 2KV_{X-}V_{Y+} \end{aligned} \tag{7.31}$$

and

$$\begin{aligned} V_{OUT-} &= I_{OUT-} \cdot \frac{1}{2} \cdot R_{OUT} \\ I_{OUT-} &= KV_{X+}^2 + KV_{X-}^2 + KV_{Y+}^2 + KV_{Y-}^2 - 2KV_{X-}V_{Y-} - 2KV_{X+}V_{Y+} \end{aligned} \tag{7.32}$$

where $K = \mu_0 C_{ox} \frac{W}{L}$. W and L are the width and length of $M4$–$M7$. Note that all the squared terms are common signals. It indicates that these common terms can be cancelled with a decent common-mode feedback circuit (CMFB). In addition, $V_{X+} = -V_{X-}$ and $V_{Y+} = -V_{Y-}$. Thus, the differential output voltage of the multiplier with CMFB is

$$V_{OUT+} - V_{OUT-} = 4KR_{OUT}(V_{X+} - V_{X-})(V_{Y+} - V_{Y-}). \tag{7.33}$$

Like other multipliers, the one employed in this design also suffers from the DC offset problem. The mismatch between the differential MOSFET pairs, especially the mismatch between $M9$ and $M10$, will result in a differential DC offset current at the output. This offset current flows through R_{OUT}, and leads to a DC offset voltage. This indicates that a smaller R_{OUT} value can reduce the multiplier's sensitivity for the component mismatch. On the other hand, in order to achieve good linearity for a wide input signal amplitude region, the gain of the multiplier must be relatively low. From Eq. (7.33), we can see that the gain of the multiplier is proportional to R_{OUT}. A smaller R_{OUT} is therefore preferred for

satisfying both requirements. In addition, according to Eq. (7.33), the gain can also be adjusted by changing the W/L ratios of $M4$–$M7$. Although a smaller R_{OUT} reduces the DC offset voltage generated by the component mismatch, if we only use the aforementioned auto-zeroed integrator to cancel the multiplier's offset [107], this big voltage difference can still drive the OPAMP input stage out of its linear operation region, and bring more non-ideality to the adaptation circuit. Therefore, the offset cancellation for the multiplier is required.

Unlike the auto-zeroed integrator discussed before, the offset of the multiplier can not be cancelled at the input stage, because if the V_Y inputs are zeroed, mathematically, the gain for V_X inputs is zero. This is the reason why the offset is rectified at $M12$ and $M14$. In Fig. 7.7, considering the charge ejection effect of ϕ_3 switches, which leads to a voltage change on C_1 and C_2 at the moment of shutting off ϕ_3, the gain from the gates of $M12$ and $M14$ to the output can not be very large. In this design, the gain is designed around $0dB$. Thus, they are both biased in the deep triode region by the error amplifier. The error amplifier with a high gain, $60dB$ in this case, provides a sufficient gain to settle the rectifying voltage difference on C_1 and C_2. This novel auto-zeroed V_{GS}^2 based multiplier circuit is another main contribution in this work.

7.3.2.2 Folded-cascode OPAMP for Auto-zeroed Integrator

The schematic of the OPAMP designed for the auto-zeroed integrator is shown in Fig. 7.9. The folded-cascode structure is employed to realize the OPAMP, which is constructed of two input stages — the main input stage and DC offset cancelling input stage. The main input stage is formed by the transistors $M1$, $M2$ and $M3$ for normal-mode operation. The DC gain achieved by this input stage is 60 dB. The DC offset cancelling input stage is formed by $M4$, $M5$ and $M6$, which does not require a large gain (normally 1/5 of the main input stage gain, 46 dB in this design). Thus, smaller sized transistors and less bias currents are used to reduce the quiescent power consumption. Note that the input referred offset on the main

input stage will lead to a current difference between I_{dM2} and I_{dM3}. This current difference can be rectified by applying an opposite voltage difference $\triangle V$ on the DC offset cancelling input stage. During DC offset cancelling operation, with ϕ_2 closed (Fig. 7.7), the OPAMP with the DC offset cancelling input stage forms a unit gain buffer. Then, $\triangle V$ is obtained and stored on C_3 and C_4.

7.3.3 Summation Circuit

The summation circuit includes two functions. First, the weights $\mathbf{W}(t)$ multiply with the RFI signal $\mathbf{X}(t)$ to produce $y(t)$, $y(t) = K_2\mathbf{W}^T(t)\mathbf{X}(t)$, which are fulfilled by K_2 multipliers. Second, the error signal $e(t)$ is generated by subtracting $y(t)$ from $d(t)$. From the perspective of circuit simplicity, in this design, summation of signals is preferably achieved by using

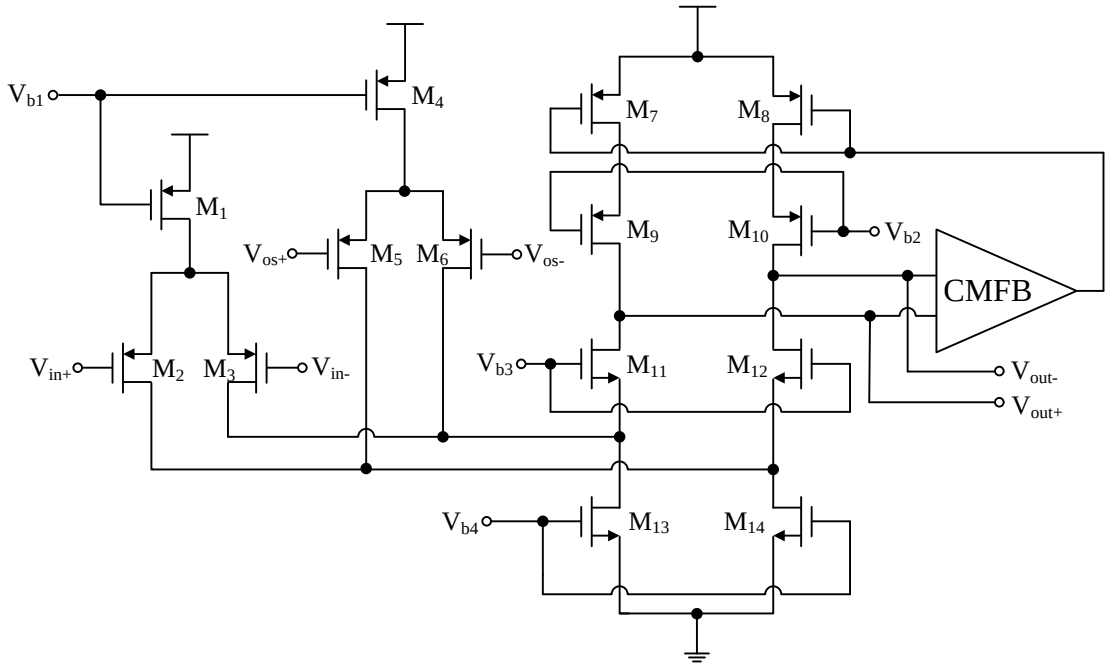

Figure 7.9: The folded-cascode OPAMP for auto-zeroed integrator

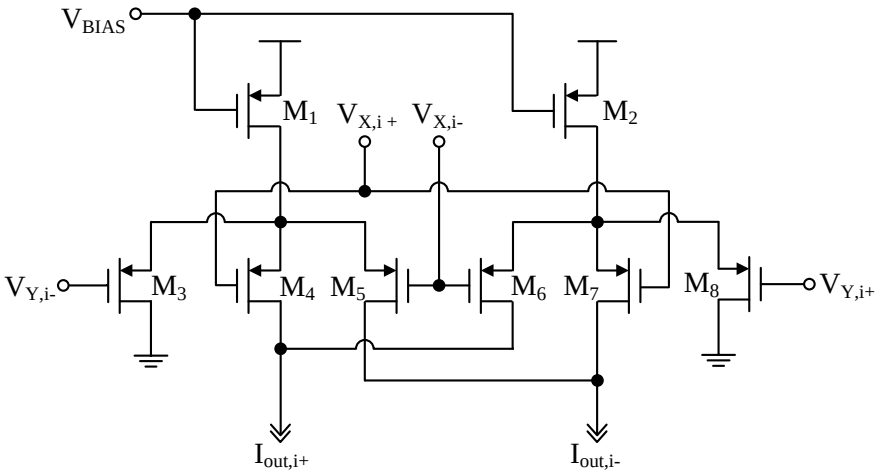

Figure 7.10: The K_2 multiplier

currents, because the results of the multiplication $\mathbf{W}^T(t)\mathbf{X}(t)$ are current signals. Therefore, the K_2 multiplier can use the same circuit structure as K_1 but without the current-to-voltage converter. The schematic of the K_2 multiplier is shown in Fig. 7.10.

All the current outputs $\mathbf{W}^T(t)\mathbf{X}(t)$ from $K2$ multipliers are connected together and delivered as the input current I_{sum} of the summation circuit, whose simplified schematic is shown in Fig. 7.11. $M1$, $M2$, $M3$ and $M4$ in Fig. 7.11 form a voltage-to-current converter circuit to transform the signal $d(t)$ from the voltage domain to the current domain, to fulfill $d(t) - y(t)$. R_{gm} is a source degeneration resistor to improve the linearity of the voltage-to-current converter. Then, $e(t)$ is generated as a voltage signal, $V_{out} = (I_{d(t)} - I_{sum})R_{out}$. Note that a CMFB circuit is still needed to cancel the common mode signal generated by K_2 multipliers.

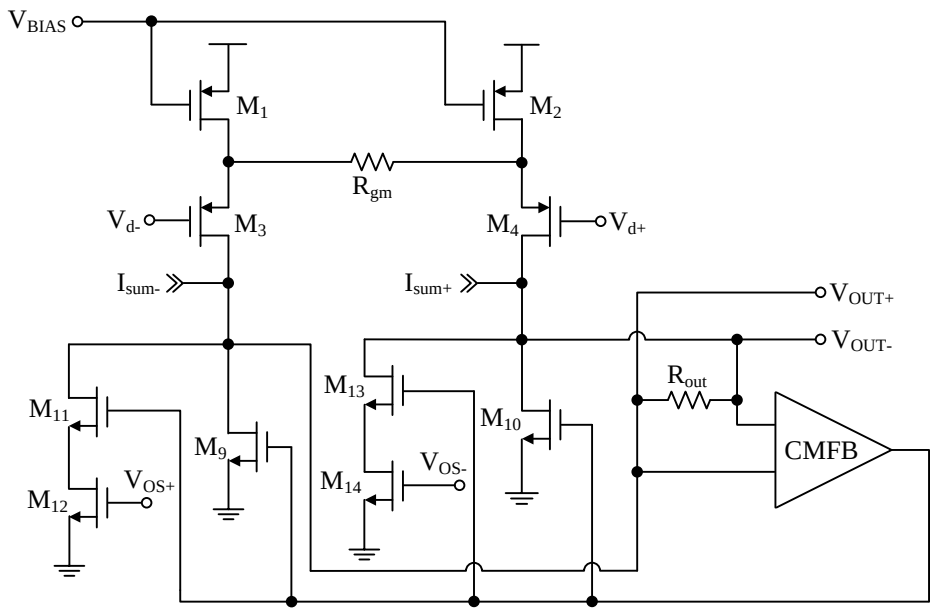

Figure 7.11: The current summation circuit

7.4 Customized IC and Experiment Results

The die photo of the customized IC is shown in Fig. 7.12. The total die area is 6.55 mm^2, in which the NQR front-end circuit occupies 0.45 mm^2. The layout of the NQR front-end circuit is shown in Fig. 7.13. This design consists of three LNAs, two pre-VGAs, a 6-tap analog adaptive filter and another VGA.

7.4.1 Continuous Time Analog Adaptive Filter

A 6-tap CTLMS adaptive filter using the proposed circuit structure is integrated in the customized IC as a part of receiver front-end circuit. The power consumption for the adaptive filter is 18 mW with 1.8 V power supply.

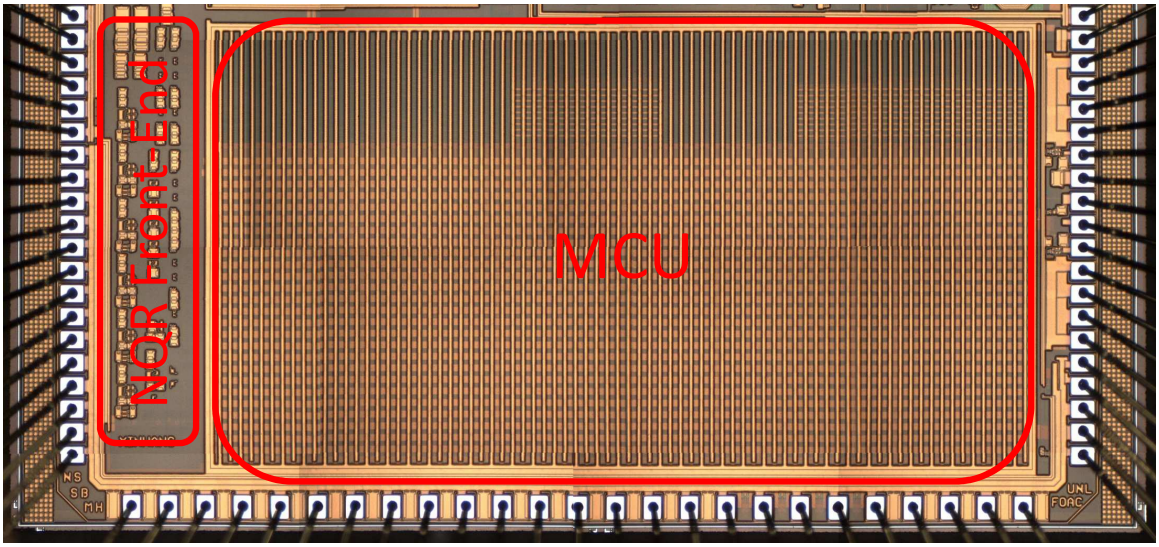

Figure 7.12: Die photo of the customized IC

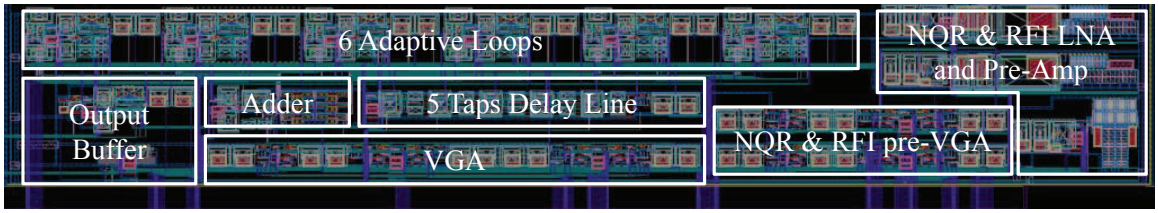

Figure 7.13: Layout of the NQR front-end circuit

7.4.1.1 Tapped Delay Unit

Fig. 7.14 shows the simulation results of the tapped delay unit. The phase delay approximately changes linearly with the signal frequency, which means a fixed group delay ($30ns$) is achieved. The gain varies from $-1.5dB$ to $-1.51dB$ in the frequency range of $500kHz$ to $6MHz$.

For the circuit level test, the NQR signal path with the 50Ω LNA is used. The input

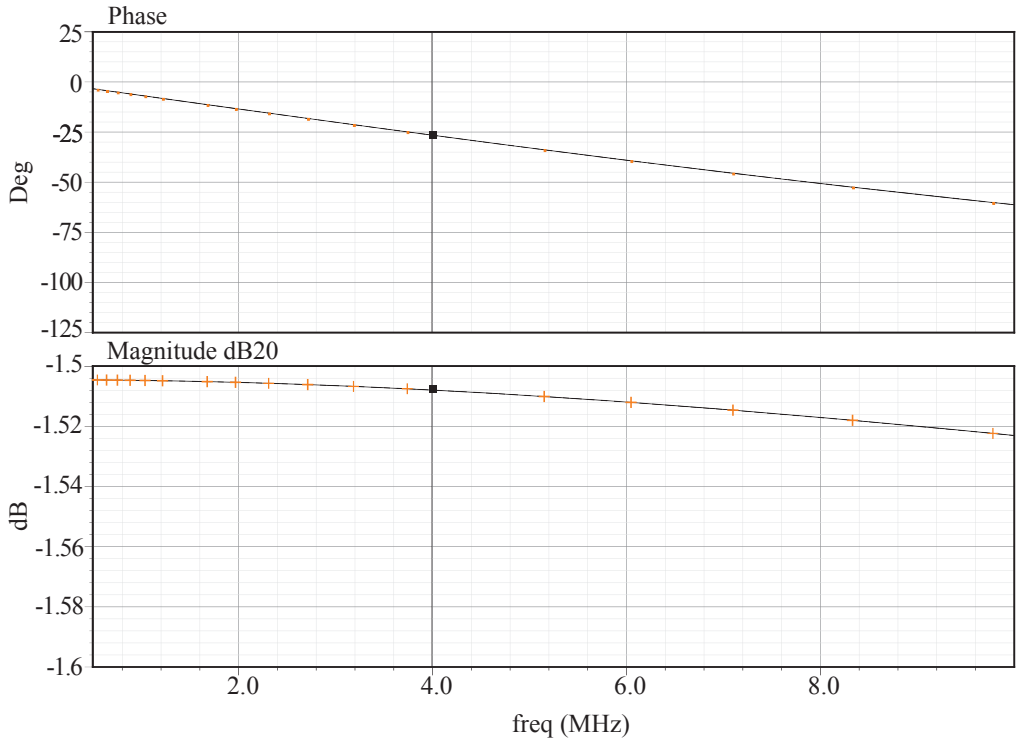

Figure 7.14: Phase and gain of the tapped delay unit

signal, which is used as the reference signal, is first attenuated by $60dB$ and connected to the LNA circuit. Then, the signals at the input and output of the delay unit circuit are compared to measure the gain and time delay. Signals with two frequencies are used for the measurements, $4MHz$ and $3.3MHz$. For $4MHz$, the measured time delay is $30ns$. The gain is around $-1.5dB$. For $3.3MHz$, the measured time delay is $28ns$. The gain is also around $-1.5dB$. Considering measurement errors due to weak input signals, the measured time delay values are fairly close to the designed values.

7.4.1.2 Auto-zeroing Weight-updating Circuit

A simulation experiment is designed to demonstrate the robustness of the proposed auto-zeroing weight-updating circuit. Fig. 7.15 shows the $d(t)$ signal in the frequency domain.

The wanted signal is a sinusoid signal with a frequency equal to $3MHz$. The interference signal's frequency is $4MHz$. The signal to interference ratio (SIR) is $-40dB$.

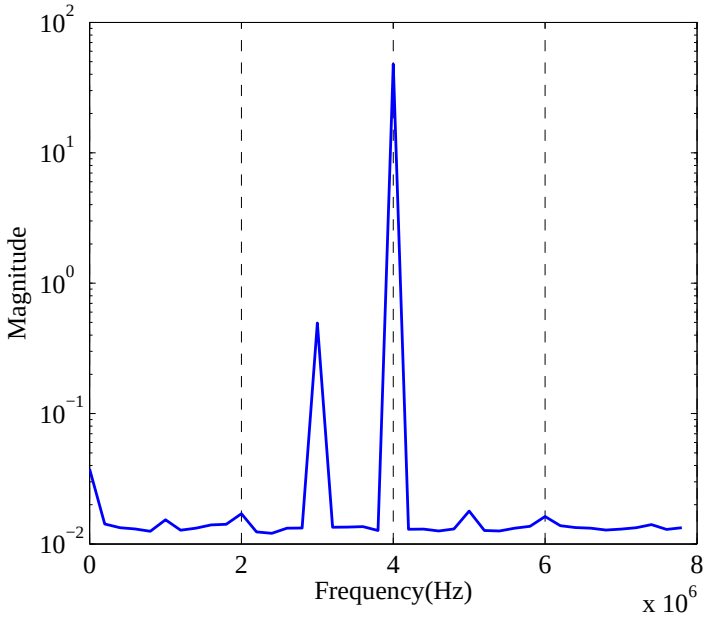

Figure 7.15: $d(t)$ in the frequency domain

In order to simulate the components mismatches, integrators' DC offset (Id) is modeled by a V_T shift on the input device ($M3$ in Fig. 7.9). Multipliers' DC offset (Md) is characterized by a V_T shift on $M10$ in Fig. 7.8.

The resulted SIR is shown in Fig. 7.16. With a constant $Id = 1mV$, Md is changed to investigate two DC offset cancelling schemes: 1) DC offset cancellation only for integrators (Only ϕ_2 on); 2) DC offset cancellation for both multipliers and integrators (ϕ_2 and ϕ_3 both on). In Fig. 7.16, we can see that the interference is suppressed by the adaptive filter. As DC offsets become larger, The performance of both schemes is affected. As Md values are small, 1 mV to 4 mV, the performance of the first scheme is slightly better. On the other hand, when Md is larger than $5mV$, the second scheme outstrips the first scheme with a big

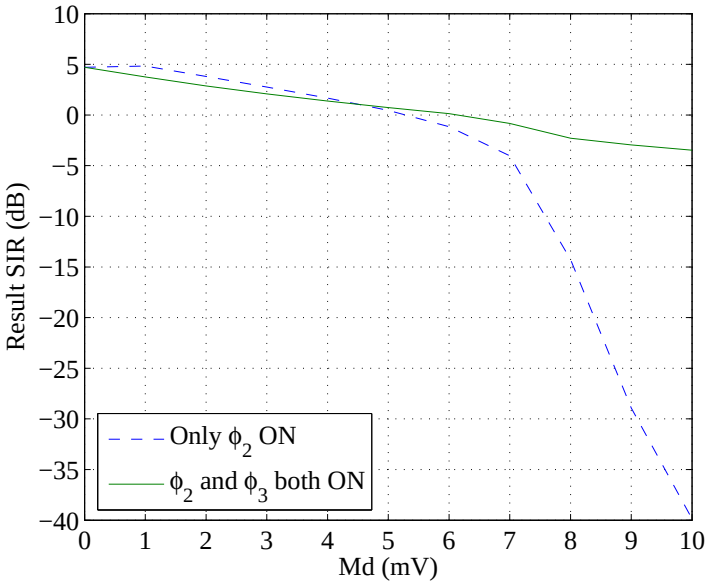

Figure 7.16: Resulted SIR for the two schemes

improvement on the resulted SIR. Especially, when Md value is big enough (Md=10 mV) to drive integrators out of the linear range, the adaptive filter with the first scheme fails to converge. But the adaptive filter with the second scheme can still fulfill the interference mitigation. Therefore, this auto-zeroing scheme is proven to have superior robustness against DC offset non-ideality of the realistic weight-updating circuit.

Fig. 7.17 shows the output and weight signals in the time domain when $Md = 10\ mV$, ϕ_2 and ϕ_3 are both on. Note that the $5\mu s$ at the beginning is the DC offset cancelling period.

7.4.2 NQR Front-end Circuit

For the simulation of the whole receiver circuit, the LNAs, pre-VGAs, and adaptive filter are all enabled. The RFI is $-80\ dBm$, and the NQR signal is $-140\ dBm$. The RFI mitigation and corresponding weight convergence process are shown in Fig. 7.18 and Fig. 7.19. The

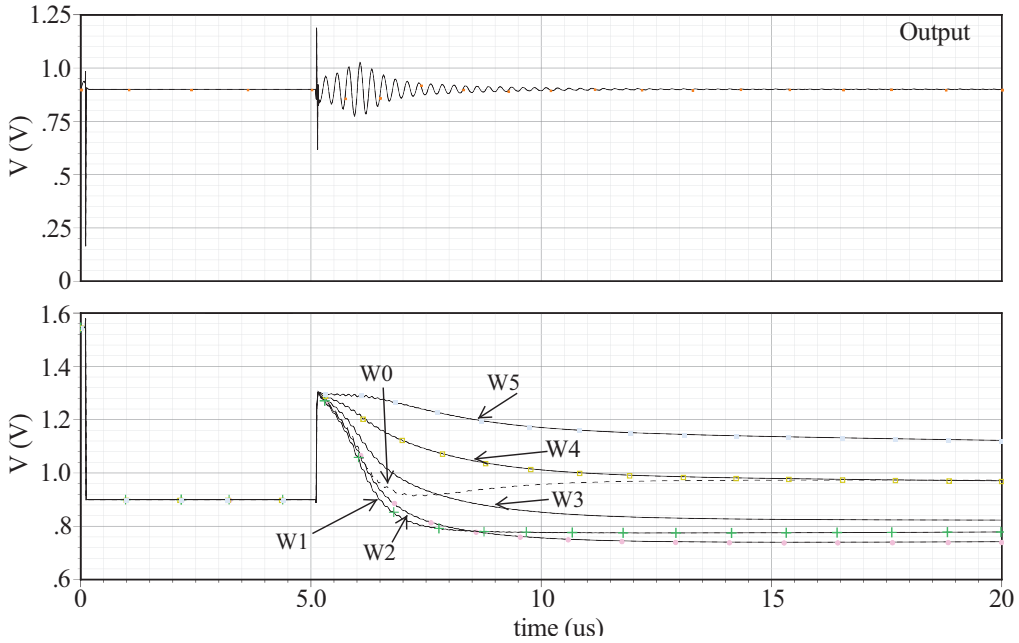

Figure 7.17: The output and weight signals with $Md = 10mV$ and both ϕ_2 and ϕ_3 on

convergence time is about $7\mu s$.

However, during the circuit test for the analog adaptive filter, a circuit design defect is found. The bias circuit for the weight-updating circuit is accidentally designed to be disabled during the DC offset cancelling phase. But it is required for the DC offset cancelling circuit to work. As a result, the analog adaptive filter fails to function properly.

7.5 Conclusion

The analog adaptive filter circuit that is used for RFI mitigation is presented. A novel weight-updating circuit topology with a robust DC offsets cancellation scheme is proposed. In this weight-updating circuit, each of the multiplier and the integrator has its own auto-zeroing DC offsets cancelling circuit to achieve good performance of the adaptive filter. The

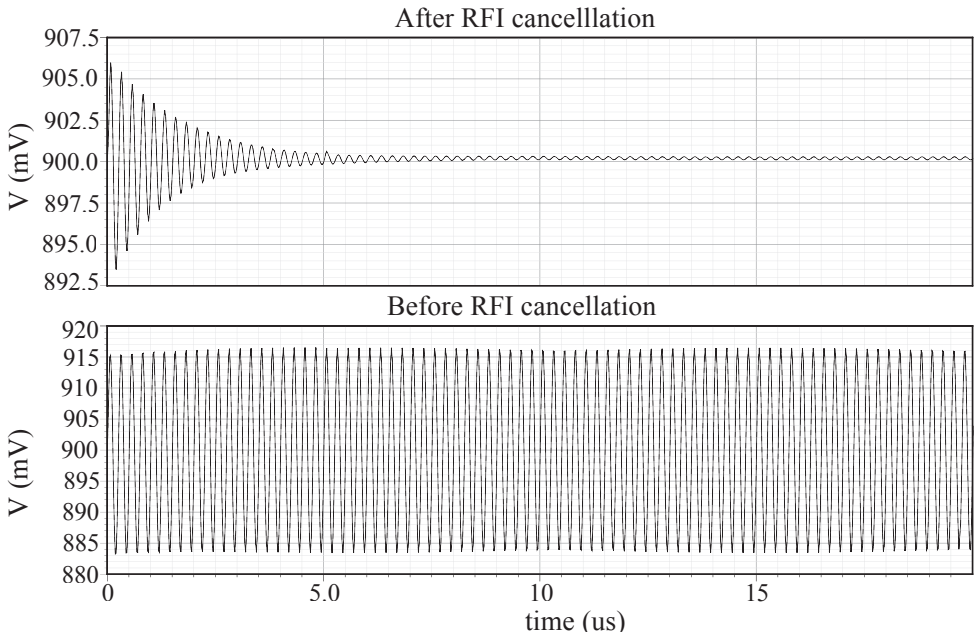

Figure 7.18: RFI mitigation

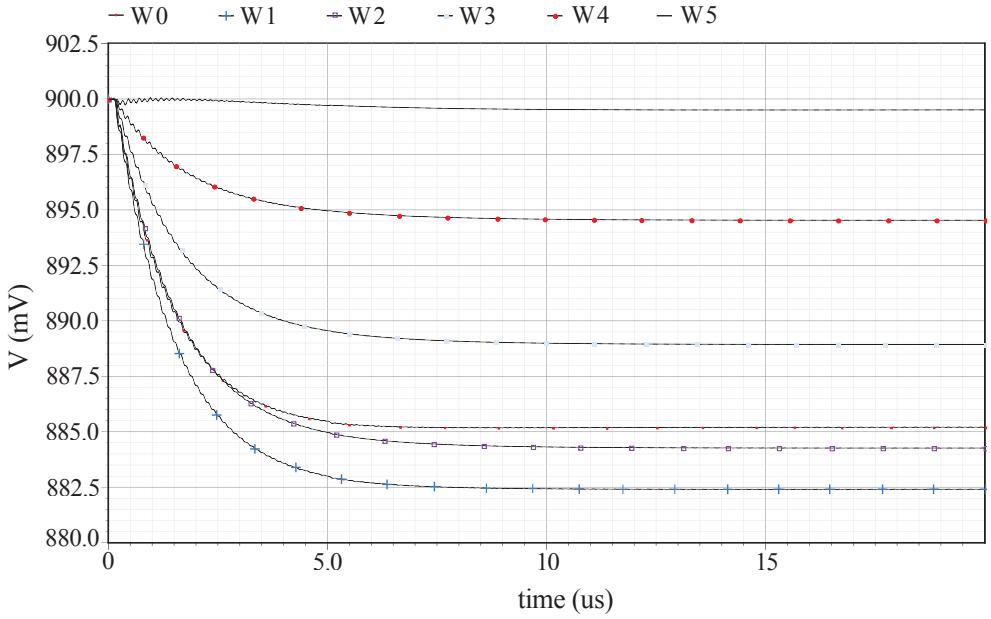

Figure 7.19: The weight convergence

design considerations of circuit modules has also been discussed. The simulated results show that the proposed analog adaptive filter can achieve good RFI mitigation performance and fast convergence rate at the same time. However, due to a design defect, the implemented adaptive filter on the customized IC fails to function properly.

Chapter 8

Software Configuration

The software design for the NQR detection system mainly include two parts: the DSP-based NQR signal collecting and processing, and the MCU-based logic control of the whole system. In this chapter, the design ideas and considerations of programming these two modules are discussed in detail.

8.1 DSP-based NQR Signal Collecting and Processing

After sufficient amplification and RFI mitigation provided by the analog processing chain, NQR signals are digitized by the ADC for further processing. In traditional NQR detection systems, a PC is often used to perform NQR signal processing. PCs can provide versatile programmability and powerful computation capability. These benefits are preferred for designing a detection system. However, it also has some drawbacks. First, a PC has a large size, and high power consumption. Also, a general PC usually does not have a dedicated high speed data transferring interface to collect NQR signal data. As a result, in addition to a PC, a special designed interface circuit after the ADC is required to transfer the high bit-rate NQR signal data into the PC memory. The extra hardware thus incurs extra cost

to the system. All of these drawbacks prevent it from being applied to a portable detection system.

On the contrary, a DSP is a computation unit specifically designed for digital signal processing applications. In addition to its compact size, power consumption of DSPs is far much lower compared to that of PCs. For computation capability, DSPs have the operating frequencies up to a few hundred of MHz which is fast enough for NQR signal processing. Moreover, DSPs are integrated with a dedicated computation unit for the so-called multiply-accumulation (MA) operation, which helps to expedite digital signal processing significantly. In general, the MA operation can be depicted by

$$M(z) = \sum_i x(i)y(z,i) \tag{8.1}$$

Normally, NQR signal processing algorithms are performed in the frequency domain. As well known, Fast Fourier Transform (FFT) is often employed to transform the time-domain signals to frequency-domain signals, which largely involves MA operations. Regarding the high bit-rate data transferring, some state-of-the-art DSPs, such as $TMS320C6xxx$ series DSPs from Texas Instrument (TI) Incorporated [111] and $ADSP-21xx$ series DSPs from Analog Devices Incorporated [112], have high speed serial and parallel interface ports that are able to directly communicate with ADCs. For data storing, current DSPs can easily support 32-bit memory address (up to $4GB$ memory space). In short, compared to PCs, DSPs can also provide sufficient processing power as well as enough memory space support for NQR signal processing, while maintain low power consumption and considerably smaller sizes.

8.1.1 The TMS320C6748 DSP Platform

In this design, a $TMS320C6748$ ($C6748$) DSP from TI is utilized to demonstrate the feasibility of using a DSP as the data processing platform. Some key features of $C6748$ differentiate it from other candidates [111].

First, the $C6748$ DSP belongs to the $C6000$ series DSPs that are based on an advanced very-long-instruction-word (VLIW) architecture equipped with an instruction set suitable for signal processing tasks. With up to a $450MHz$ operating frequency, it can provide powerful computation capability that is required for performing various detection algorithms. On top of that, a pipeline parallel processing technique is implemented in the $C6748$ to further improve the operating speed. The idea of this technique is to simultaneously execute different portions of multiple instructions at the same time to increase the processing speed. The discussion of the pipeline parallel processing technique is beyond the scope of this work. Detailed information about this feature can be found in [113]. In addition to its high performance, the $C6748$ is well known for its low power consumption which is an important benefit for the proposed system. Under typical working conditions, it consumes $426mW$ according to [114].

Second, the $C6748$ has a high speed memory controller that supports 16-bit DDR2 SDRAM with maximum $512MB$ address space. The large memory space satisfies the requirement of NQR data collection, especially the multi-pulse sequence detection. For instance, the sampling frequency of an ADC is usually set to a value larger than $12MHz$, since the maximum NQR signal frequency is $6MHz$. Suppose that $40MHz$ sampling rate is used, $50ms$ sampling time is needed, 2 bytes is occupied by one sample, and 100 RF pulses are generated in one detection cycle. In this case, total memory needed for restoring the raw data is $400MB$. $512MB$ is sufficient for holding the raw data from one detection cycle.

Third, the $C6748$ is integrated with a universal parallel port (UPP) through which the

$C6748$ is able to directly communicate with a high sample rate ADC. The UPP is a high speed parallel interface with 16-bit data width. It is dedicated to data transferring between the DSP and external high sample rate ADCs, DACs or field-programmable gate arrays (FPGA) based parallel interface circuits. The aforementioned sampling example also shows that the UPP is the most desirable feature of the $C6748$ for NQR data collection. In addition to the UPP, the $C6748$ also has a direct memory access (DMA) module that can transfer the data in a block manner between different memory modules and interfaces without involving CPU instructions during the transfer process. As a result, the computation process for one segment data can be executed by the CPU in parallel with the data collection for the next segment. The total detection time is therefore reduced.

8.1.2 Dataflow from Frond-end to DSP

The data collecting flow is depicted in Fig. 8.1. The analog NQR signal from the front-end is first digitalized by an ADC. In this design, a 12-bit ADC with a $80MHz$ maximum sampling frequency is employed for the digitization. On the DSP side, the UPP is connected to the ADC for data transferring. Generally, the data sync clock for a parallel port is given by the data output end, an ADC in this case. In a $C6748$ DSP, the data sync clock can be as high as 1/4 of the main clock (MCLK) frequency. In the default MCLK mode where $f_{MCLK} = 300MHz$, the data rate can be $75MHz$ with 16-bit data width, which is adequate for NQR signals. In this design, the ADC clock is set to $f_{sampling} = 40MHz < 75MHz$ to leave headroom for the UPP to sync the data correctly.

While the data are being received by the UPP, the DMA is used for conveying data to the memory. After the CPU enables the DMA, no CPU instructions are needed for the following data transferring process. Thus, the DMA can be considered as a self-conducting data bus. With a source address and a target address provided, the DMA conveys data in

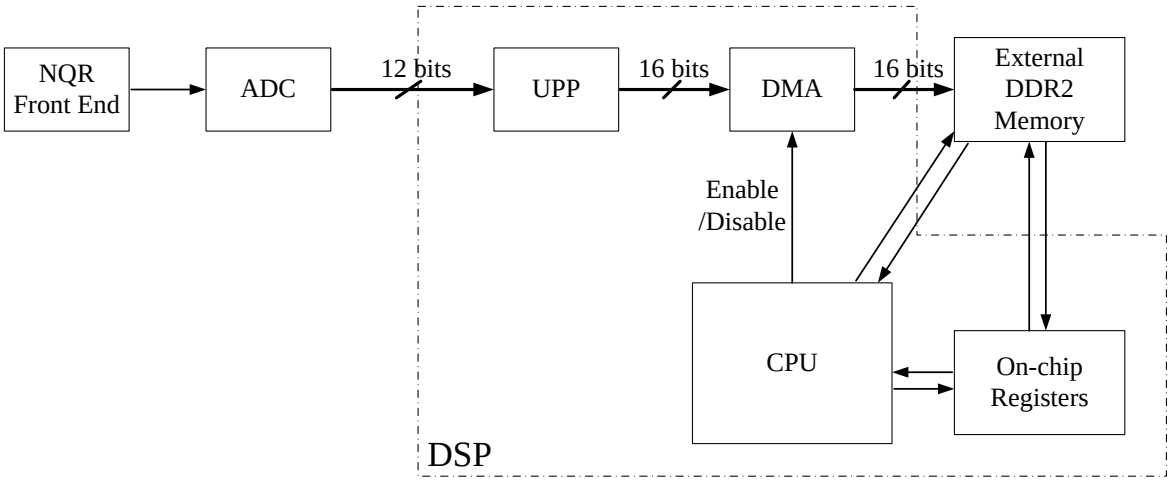

Figure 8.1: The data flow from the NQR frond-end to the DSP

blocks with a given block size. The source address is defined as the address of the UPP. The target address is the address of the variable defined for raw data. Due to the large data capacity requirement, this variable is often allocated on the external DDR memory. The UPP is always enabled to ensure the data from the ADC is received immediately. The DMA needs to be disabled by the CPU every time the transferring of the current segment is finished. The block size of the DMA is defined as the time needed for gathering one segment multiplying the sampling frequency. When data transferring of one segment is finished, CPU can load it to the registers for processing.

8.1.3 DSP Software Design

The design of DSP software is illustrated by the flowchart shown in Fig. 8.2. The program starts with an initiation step in the DSP. In the initiation step, the DSP is first powered up in a pre-defined sequence. Then the needed interfaces are configured, including the UPP, DMA, Serial Peripheral Interface (SPI) and DDR2 interface. As explained above, the UPP

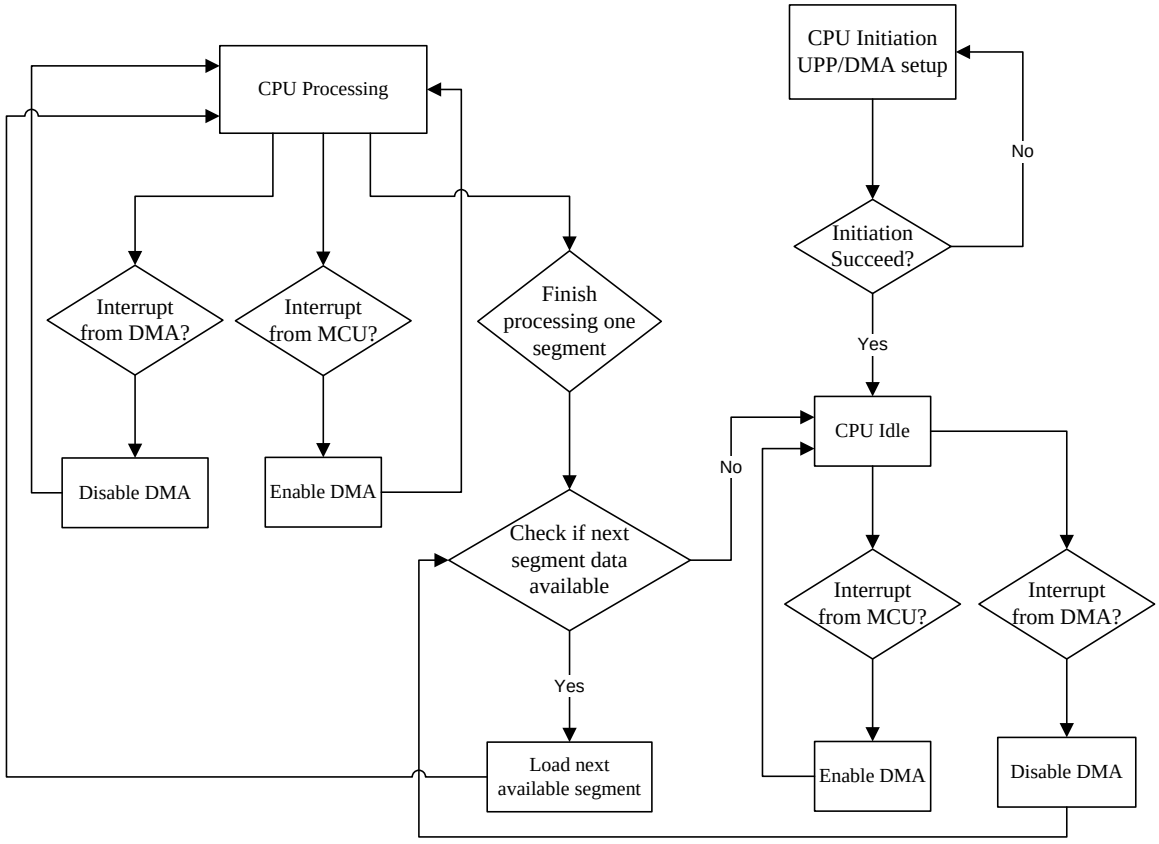

Figure 8.2: The flowchart of DSP software design

and DMA are used for data collecting. The SPI is responsible for the communication between the DSP and MCU. It is mainly used for sending the gain control signal of the VGA from the DSP to the customized IC. As the NQR raw data may occupy large memory space, the DDR2 interface is initiated to utilize the external large-size memory. The address of the variable for storing raw data needs to be assigned in the external memory when the program is being executed.

When the initiation step is finished successfully, the CPU enters the idle mode waiting for the interrupt signal from the MCU which indicates that data start to arrive. Once getting this interrupt, the DMA controller is enabled by the CPU to transfer data to the memory.

When the DMA operation is finished, it sends another interrupt to the CPU. Then the CPU disables the DMA and starts to process this signal segment. Depending on the design of the excitation RF pulse sequence and detection algorithm, CPU processing time for one signal segment can be either longer than the interval between RF pulses (for instance, the pulse train for echo signal detection), or shorter than the interval (multi-pulse detection for FID signals). If the CPU processing time is longer, CPU processing may be interrupted either to enable the DMA for receiving new segment data, or to disable the DMA when the receiving is finished. After handling the interrupts, the CPU resumes the processing task from where it stops. When the processing for one signal segment is finished, the CPU will check if the data of next segment is ready. If yes, it moves on to process it. If the CPU processing time is shorter, which means when the CPU finishes one signal segment, the next segment is not ready yet, the CPU will enter the idle mode again. The above process is repeated until all the segments are processed. As the CPU processes data in parallel with NQR data collection, the total detection time of the system is greatly reduced.

8.2 Logic Control of the Proposed System

Same as other NQR detection systems, the proposed system needs to have a "brain" to coordinate different parts of circuits to work together in a right sequence. The "brain" in this design is realized by an MCU that is integrated on the customized IC. This core features 16-bit Reduced Instruction Set Computing (RISC). As the MCU is dedicated to timing generation and sequence control, its design is greatly simplified. Only a small instruction set consisting of 28 instructions has been implemented. Communication interfaces, such as SPI, Universal asynchronous receiver/transmitter (UART) and Inter-Integrated Circuit (I^2C), are included on the MCU to facilitate the communication between the MCU, ADC and DSP, as well as the programming in each module. Timing control for the system is

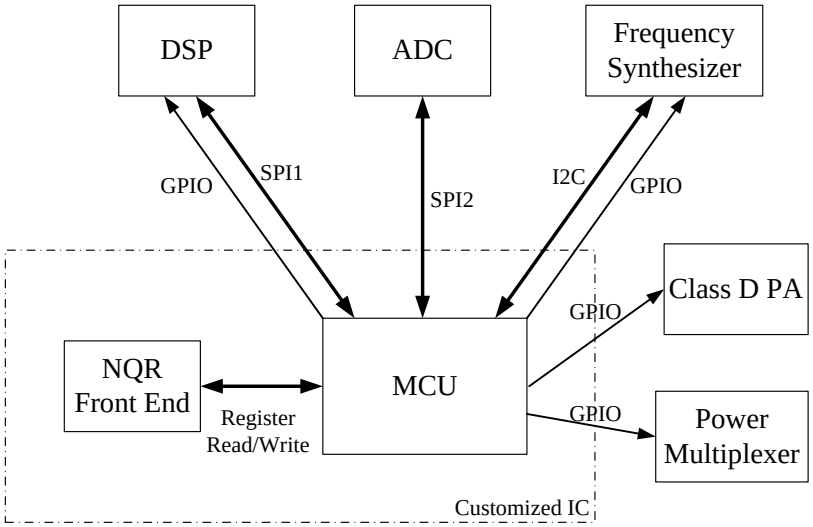

Figure 8.3: Control and communication protocol of the MCU to the circuit modules

mostly achieved by four hardware timers integrated in the MCU. The operating frequency of the core can reach as high as $60MHz$. All the instructions can be executed in a few clock cycles. Therefore, it is powerful enough to handle the control tasks for the proposed system. The design details of the MCU can be found in [115].

From the discussion starting from Chapter 3 until Chapter 7, the logic control is required for almost every circuit block, including the Class-D PA, PIN diode power multiplexer, adaptive filter, VGA, ADC, and DSP. Based on the previous descriptions, the logic control and communication between the MCU to other functional blocks in the system are summarized and illustrated in Fig. 8.3. The protocol mainly contains the following control functions:

1) The Class-D PA control. It involves enabling and disabling the PA, and the control of fast-start and fast-stop functions. This part of control functions are fulfilled through general purpose input/output (GPIO) ports of the MCU.

2) Power multiplexing control. It includes turning on and off the PIN diode switch for receiving and transmitting period. A GPIO port is again used to realize this control function.

3) Control of the NQR front end, including DC offset cancellation for the adaptive filter, and gain control for the VGA. As the NQR front end and the MCU are on the same chip, several registers are designed for this part of configuration. The MCU can directly write and read these registers for certain control tasks.

4) Programming and configuring the ADC. An SPI interface is utilized for the communication between the MCU and the ADC for this purpose.

5) Controlling and programming the frequency synthesizer, which generates the NQR frequency clock signal for the Class-D PA and the sampling clock signal for the ADC. An I^2C port on the MCU is used for this task. Actually, the NQR frequency clock signal should be disabled during receiving period to avoid interfering the collection of the returning NQR signal. Also, the sampling clock signal for the ADC should be disabled during the transmitting period to reduce power consumption. These enabling and disabling functions are realized though GPIO ports.

6) Communication between the MCU and the DSP, which include two functions. One function is to create an interrupt by the MCU to the DSP when one segment data are ready to start transferring. This interrupt is sent through GPIO connection between the MCU and DSP. The other function is to send the gain control signal from the DSP to the VGA. The gain control signal is conveyed via a SPI port as mentioned in Section 8.1.

Obviously, the logic control does not only guarantee the working sequence of different functional units, but also, more importantly, adjust the timing between control events. Tim-

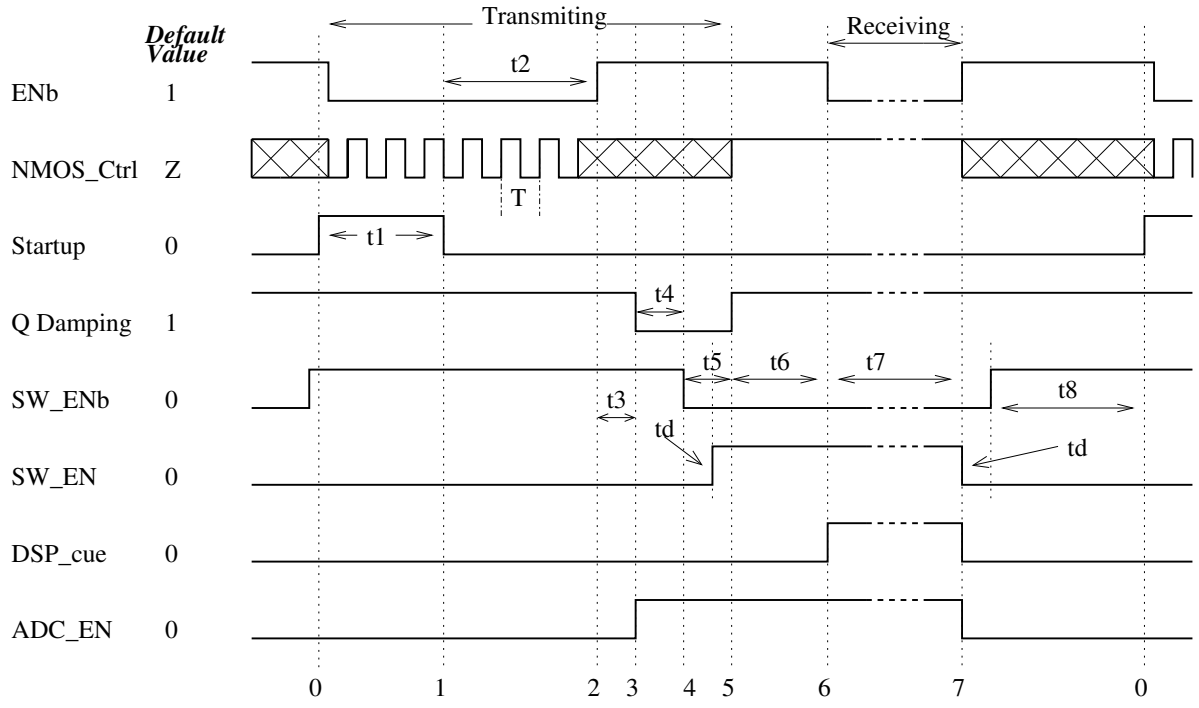

Figure 8.4: Simplified control logic waveforms

ing generation for control events is performed by one of the four hardware timers. The timer has a clock selector and prescaler, a 16-bit counter, three compare units, and two capture units. In order to guarantee timing accuracy and to improve immunity to environment temperature variation, the hardware is configured to employ a $16MHz$ clock directly from a crystal oscillator. In another word, the finest adjustable timing step is:

$$\triangle t = \frac{1}{16 \times 10^6} = 62.5\ ns \tag{8.2}$$

In the proposed NQR system control scheme, fast-start and fast-stop control for the class-D PA usually constrains the timing accuracy demand, which requires $\triangle t < 200ns$. It can be seen that the timer circuit can easily satisfy this requirement.

The simplified logic control sequence for the whole NQR system is illustrated by Fig. 8.4. For each cycle which consists of a receiving period and a transmitting period, the process can be roughly divided into 8 timing events. For multiple RF pulse sequence detection, these 8 events are repeated for each RF pulse in the sequence. In Fig. 8.4, ENb and $NMOS\_ctrl$ are the control signals for the Class-D PA switching power stage. When ENb is low, the NMOS in the power stage is driven by $NMOS\_ctrl$, and the PMOS is driven by the inverted version of $NMOS\_ctrl$. *Startup* is the control signal to switch the power supply for the Class-D PA to realize fast-start function. *Q Damping* turns on the Q damping circuit for fast-stop function. SW_ENb and SW_EN turn on and off the PIN diode switch. td, the dead time between the transitions of SW_ENb and SW_EN is introduced to prevent the shoot through in the PIN diode driver circuit. ADC_EN is the enable signal for the ADC. DSP_cue is the signal for the DSP indicating that the receiving period starts. The ADC is enabled on time 3, before the DSP starts collecting data, to make sure the initiation process of the ADC is finished. $t2$ is the pulse width of the NQR stimulus pulse that controls the flip angle of the nuclei, as explained in Chapter 2. $t6$ and $t7$ can be changed for capturing different portions of NQR signals: FIDs or echos. The summation of $t5$, $t6$, $t7$ and $t8$ is the time interval between two adjacent RF pulses, which is $t_{gap,i}$ depicted in Fig. 2.9. It can be individually programmed to different values for multiple RF pulse sequence detection applications.

8.3 Conclusion

In this chapter, the software design considerations and implementations are presented. In the proposed system, we employ a state-of-the-art DSP platform for data processing, and integrate an MCU on the customized IC for logic control.

The DSP is TMS320C6748 from Texas Instruments, which features the pipeline parallel

processing technique to improve the processing speed and a UPP port to facilitate data transferring between the DSP and external data converters. By utilizing the UPP and DMA, the DSP is able to receive data and process the received data in parallel, which improves detection time significantly.

The integrated MCU has a 16-bit customized and minimized instruction set. The logic control of the whole system is performed by the MCU, which guarantees the working sequence of difference functional modules and adjusts the timing accurately between control events.

Chapter 9

NQR Detection System Hardware Implementation and Detection Experiment Results

In this chapter, the hardware implementation of the proposed portable NQR based explosive detection system solution is described. In addition, experimental detection results with actual explosive samples are presented to prove the effectiveness of the proposed system. As this system is for portable applications, a power consumption analysis is conducted with break-down details for each circuit section. Finally, the discussion is concluded in the last section.

9.1 Hardware Implementation

The proposed portable NQR based explosive detection system is implemented in a board level design. Fig. 9.1 shows the photo of the prototype system. The system consists of three boards: the receiving (RX) board, transmitting (TX) board and DSP evaluation board. RX

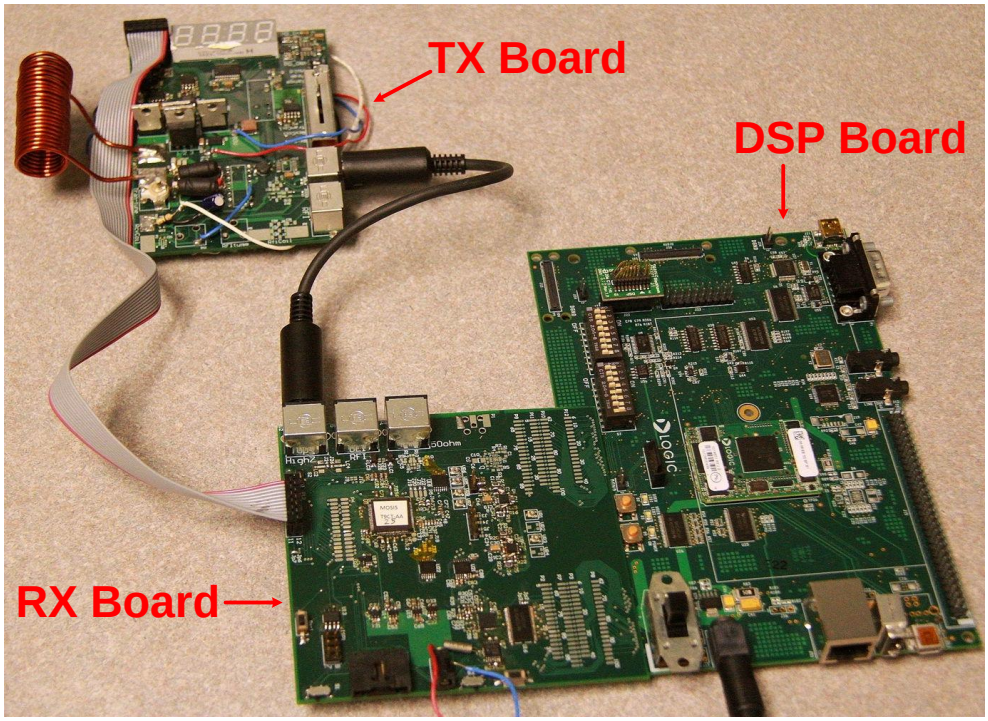

Figure 9.1: Photo of the prototype system.

board and TX board contain the circuit modules that are described in the previous chapters. The purpose of implementing the RX section and TX section on two separate boards is to improve noise isolation and coupling blockage. The $TMS320C6748$ DSP evaluation board that is adopted in this system is a commercial off-the-shelf evaluation kit from LogicPD Inc. [116].

The TX board is shown in Fig. 9.2 (a). The size of the TX board is $10.6cm \times 7.6cm$. It contains the Class-D PA circuit, PIN diode based RF switch, and power matching circuit for the NQR probe coil. The NQR probe is supposed to be connected to the TX board so that it is close to the matching network. A shielded differential cable is used to conduct NQR signals from the TX board to the RX board.

The RX board is shown in Fig. 9.2 (b). Its size is $10.2cm \times 10.7cm$. The proposed

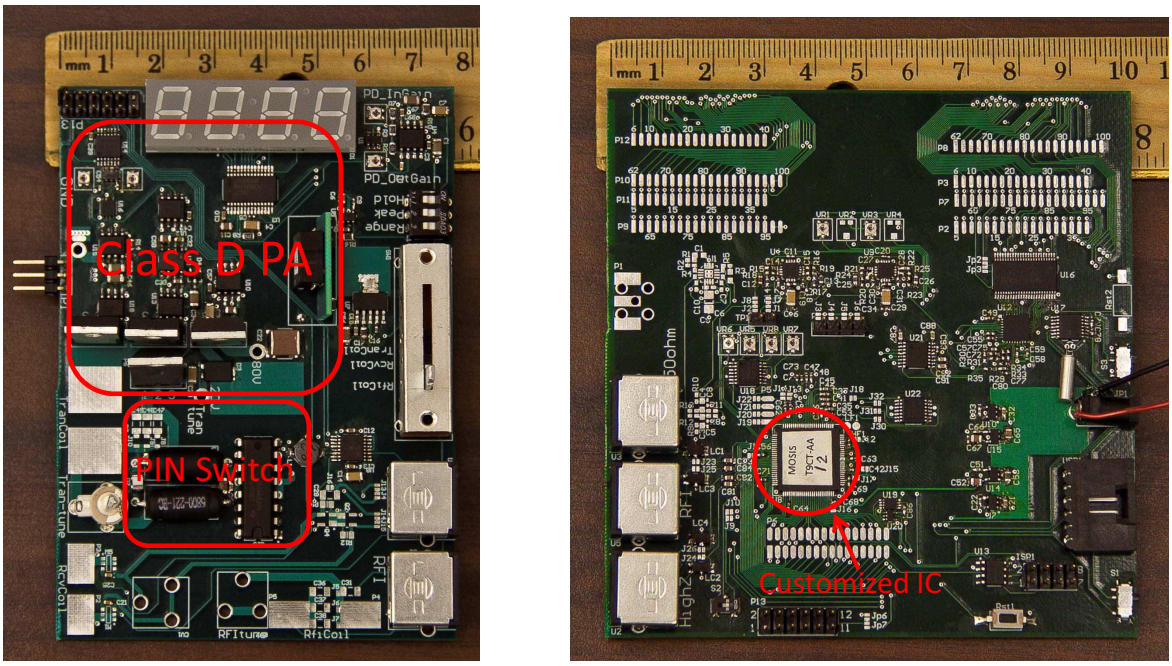

(a) The TX board (b) The RX board

Figure 9.2: The TX and RX boards

customized IC resides on the RX board with necessary supporting circuits. Other circuits that are required for the NQR signal RX front-end are also integrated on the RX board, such as the ADC, the pre-filter for the ADC, frequency synthesizer, interface circuit between ADC and DSP, etc. Control signals for the TX section are provided by the MCU on the customized IC from the RX board. A ribbon cable is used to deliver the control signals to the TX board. For communication between the RX board and DSP board, board-to-board connectors are used to provide the connection.

9.2 Prototype System Detection Experiment Results

The prototype system is tested with two kinds of samples for NQR signal collection, hexamethylenetetramine (HMT) and Urea. The results are presented and discussed in the following

sections.

For each detection cycle, the RX board consumes averagely $572mW$ during the receiving period and $228mW$ during the transmitting and idle period. On the TX board, by using $\eta = 60\%$, the class-D PA consumes averagely $16W$ during the transmitting period and $50mW$ during the receiving period and idle period. The PIN switch consumes $1.5W$ during the receiving period and less than $3mW$ during the transmitting and idle period. In total, the average power consumption of the prototype system for this test setup is $287mW$, calculated using Eq.(9.1) in section 9.3.

9.2.1 HMT test result

As HMT is more stable compared to other explosives, it is often adopted for NQR equipment testing in the laboratory. In addition, its NQR signal frequency is $3.309MHz$ at room temperature, which approximately falls at the central point of explosive NQR signal bandwidth, $500kHz$ to $6MHz$.

A solenoid coil is employed as the probe for HMT NQR signal measurement. The solenoid coil is made of magnet wire that has a diameter equal to $1.6mm$. The length of the coil is $44mm$ with 23 turns, $N = 23$. The diameter of the coil is $16mm$. The measured inductance of the coil is $L = 2.6318\mu H$, and the series resistance is $R_s = 0.607\Omega$. At the HMT NQR frequency $3.309MHz$, the quality factor of the coil is $Q = 90$. Given the physical size of the coil, the estimated magnetic flux density inside the coil can be derived as $B = \mu Ni/L = 6.72 \times 10^{-4} \cdot i\ T$, where i denotes the AC current driven into the coil. Theoretically, the intensity of NQR signals reaches the maximum value when the flip angle is equal to 119° [53]. Based on Eq. (2.3), the estimated pulse width which yields 119° flip angle is: $\tau = 159/i\ \mu s$. In this experiment, the Root Mean Square (RMS) value of the stimulus AC current is adjusted to be around $4A$, which leads to $\tau \approx 40\mu s$.

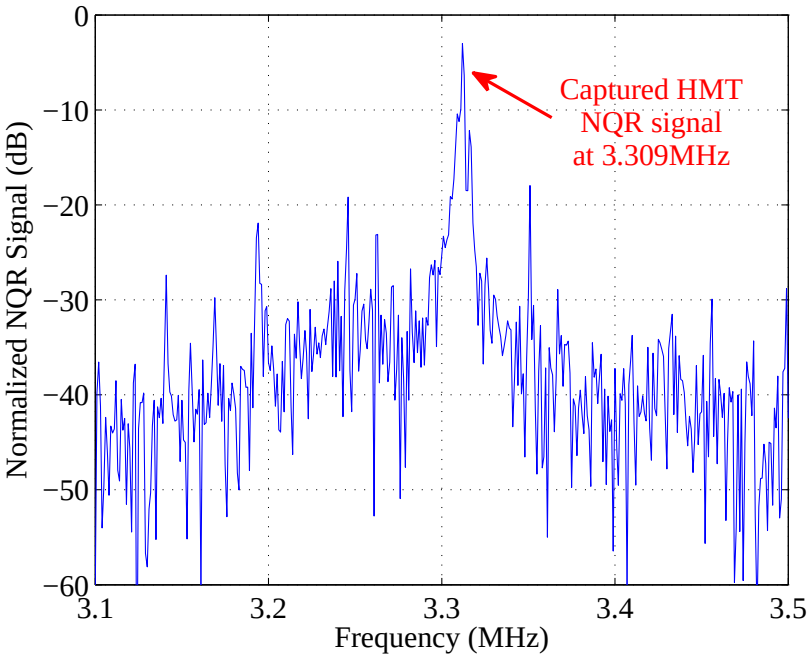

(a) With HMT sample presented

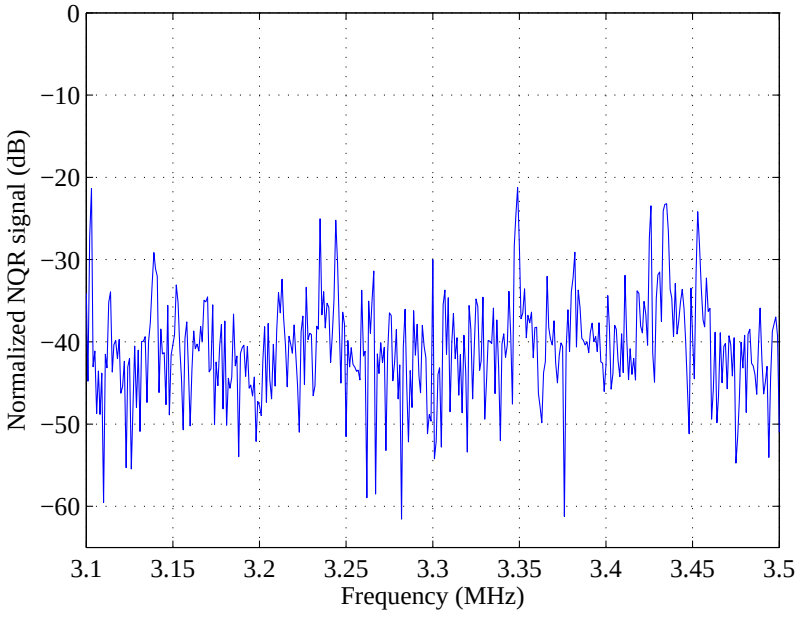

(b) Without HMT sample presented

Figure 9.3: HMT NQR signal test results

In the real sample test, $5g$ of HMT sample is placed inside the solenoid coil. With $i_{rms} = 4.12A$ and $\tau = 30\mu s$, the maximum NQR signal level can be captured. The sampling frequency is set to $40MHz$. The NQR signal is recorded $50\mu s$ after the stimulus pulse ends. For each stimulus pulse, the receiver records 3 ms of NQR signal from the NQR probe. The interval between two stimulus pulses, t_{gap}, is $1s$. The detection cycle is repeated 100 times. The NQR signal segments of 100 receiving cycles are averaged to increase signal to noise ratio (SNR). The spectrum of the detected HMT NQR signal is shown as Fig. 9.3 (a). To demonstrate the detection behavior of the prototype system, the detected signal spectrum with the identical settings but without HMT sample present is shown as Fig. 9.3 (b). Comparing Fig. 9.3 (a) and (b), the prototype system can provide around $40dB$ SNR with the current setup. The detection function is proven effective.

9.2.2 Urea test result

Urea (CON_2H_4) has an NQR signal frequency located at $2.87MHz$ at room temperature. It is another sample that is often adopted for NQR experimental studies [117, 118]. Although Urea is not an explosive material, as its frequency falls into the frequency range for which this detection system is designed, we use Urea as the second sample to test the detection effectiveness of the prototype system.

The same coil used for HMT sample test is adopted for Urea NQR test. The resonant cap is adjusted so that the resonant frequency of the probe is set to $2.87MHz$. The same power setting, $i_{rms} = 4.12A$, is used to search for the pulse width which yields 119° flip angle. The experiment shows that $\tau = 40\mu s$ leads to the maximum NQR signal level. The sampling frequency is set to $40MHz$. The NQR signal is recorded $50\mu s$ after the stimulus pulse ends. For each stimulus pulse, the receiver records 1 ms of NQR signal from the NQR probe. The interval between two stimulus pulses, t_{gap}, is set to $5s$ because Urea holds long T_1, around $2s$.

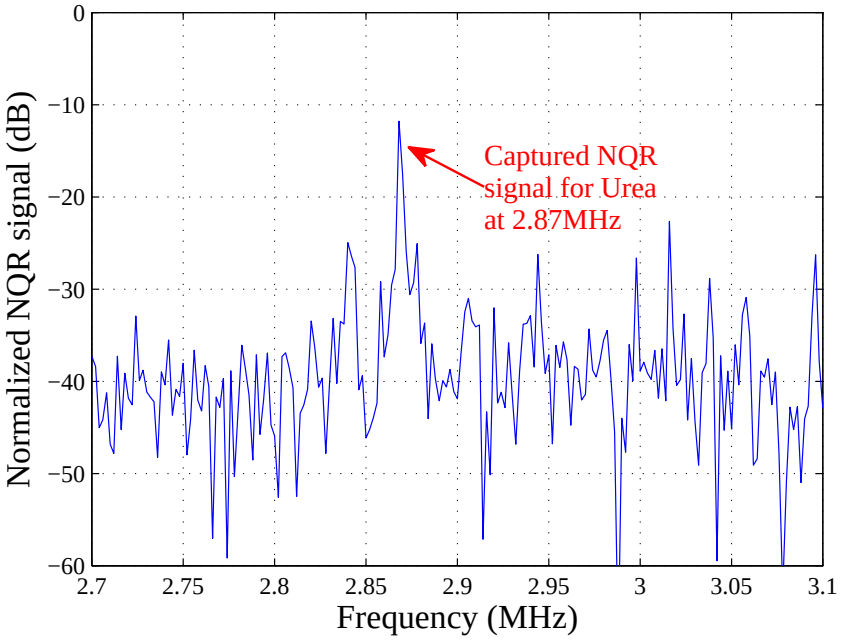

(a) With Urea sample presented

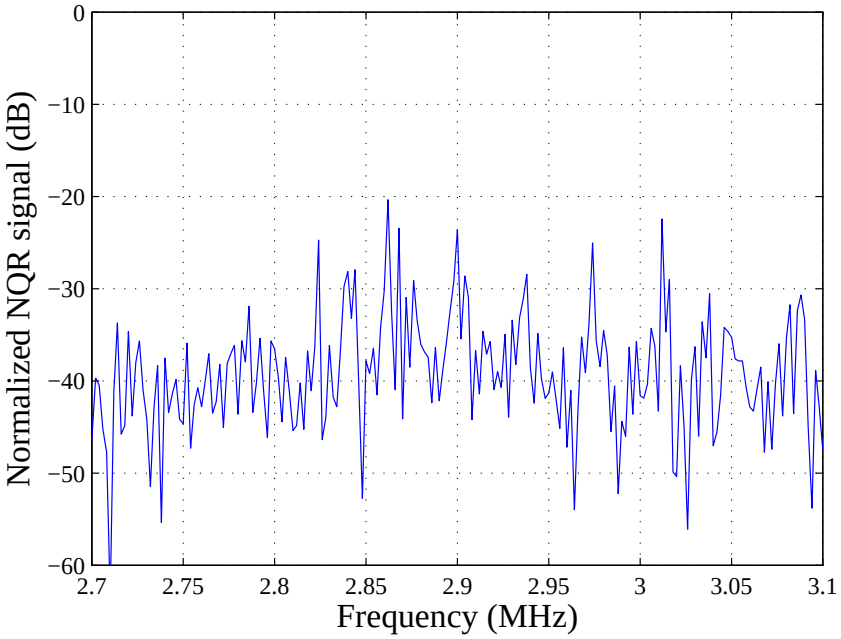

(b) Without Urea sample presented

Figure 9.4: Urea NQR signal test results

The detection cycle is repeated 100 times. The NQR signal segments of 100 receiving cycles are averaged to increase SNR. The spectrum of the detected Urea NQR signal is shown in Fig. 9.4 (a). For comparison, same as HMT results, the spectrum for a test with identical settings but without Urea sample in the probe is shown Fig. 9.4 (b). Comparing Fig. 9.4 (a) and (b), the NQR signal tone appears at the frequency $2.87MHz$. The detection function is proven effective.

However, the Urea test result shown in Fig. 9.4 (a) manifests smaller signal amplitude than HMT. This is due to the fact that the HMT material used for NQR tests is crystalized sample whereas Urea NQR test uses a powder sample.

9.3 Power Consumption Analysis

Other than the compact size, power consumption is also an important aspect as far as systems designed for portable applications concern. Therefore, a power consumption analysis is performed in this section. Referring to Fig. 8.4, one cycle of the detection action, denoted as T, can be divided into three time sections for power consumption analysis: the transmitting state($t_1 + t_2$ in Fig. 8.4), receiving state(t_7 in Fig. 8.4) and idle state (t_8 in Fig. 8.4). In the transmitting state, most power is dedicated to generating NQR stimulus signals. The Class-D PA is in the operation mode. The MCU provides logic control to the Class-D PA. In the prototype system, to guarantee accuracy and low noise of the NQR clock frequency, a stand-alone synthesizer is employed to generate the clock signal for the Class-D PA. The ADC is set to the low-power mode. The PIN diode switch is in off-mode which only has a negligible reverse leakage current, measured less than $10\mu A$. During the receiving period, The Class-D PA is turned off. The NQR frond-end is enabled to provide amplification on NQR signals. The ADC is enabled and the DSP is in normal operation mode. Meanwhile, The PIN switch is turned on with forward biasing the PIN diode. To minimize additive noise and

insertion loss of the PIN switch, the forward biasing DC current should be maximized, but bounded by the current limit of the PIN diode. In the idle period, which is the time interval between receiving and transmitting, every unit is disabled except the MCU. The detailed power consumption characterization is listed in Table 9.1. The total power consumption of the system for each detection cycle P_{system} is:

$$P_{system} = \frac{P_R \cdot t_7 + P_T \cdot (t_1 + t_2) + P_T \cdot t_8}{T} \tag{9.1}$$

Table 9.1: Power consumption for each function module

Function Module		$\mathbf{P_R}$ (mW)	$\mathbf{P_T}$ (mW)	$\mathbf{P_I}$ (mW)
RX Board	NQR Front-End	67	1	1
	ADC	308	30	30
	MCU	9	9	9
	Supporting Circuit	188	188	188
	Total	572	228	228
Class D PA		50	P_{out}/η	50
PIN Switch		1500	3	3
Total		2122	$P_{out}/\eta + 231$	281

P_R is the power consumption in the receiving state.
P_T is the power consumption in the transmitting state.
P_I is the power consumption in the idle state.
P_{out} is the output power that is driven to the NQR probe during transmitting period.

9.4 Conclusion

A prototype system is built up by implementing the proposed portable NQR based explosive detection system solution. The board level design demonstrates a small total volume of the whole detection system . The test results with two sample materials, i.e. HMT and Urea,

prove the feasibility and effectiveness of the proposed system solution. Moreover, a detailed power consumption breakdown is presented to verify its low power performance.

Chapter 10

Conclusion and Future Work

This work presents an NQR based explosive detection system solution towards the portable applications. It is required that the system solution features a compact size as well as low power consumption while maintains high detection performance. All the novel circuit solutions and detailed design considerations are described in this dissertation.

In the TX section, a new Class-D type switching voltage power amplifier is proposed to provide high power efficiency during the transmitting period. More importantly, the proposed Class-D power amplifier has very low standby power consumption during the receiving period, which is proven to be the most significant power saving advantage compared to traditional Class-AB power amplifiers. A novel power multiplexing method that includes an infinity impedance power matching scheme for the RX section is specifically designed to cooperate with the Class-D power amplifier. By using this power multiplexing mechanism, the NQR probe can also be simplified to be the NQR coil and one single resonant capacitor. This eases the tuning process of the probe and reduces the cost.

In the RX section, an LNA design based on the aforementioned infinity impedance power matching scheme is presented. It can achieve a very low noise figure that improves the detection performance. In addition, a new NQR RX front-end circuit configuration with an

analog adaptive filter is proposed to mitigate the impact from RFI. All the front-end circuits, including LNA, pre-amplifier, analog adaptive filter and VGA are integrated on a customized IC with an MCU circuit. The MCU is used for the whole system work coordination and timing sequence control. This customized IC adopts state-of-the-art SOC design concepts to achieve low power consumption and high integration.

For the NQR signal processing, a DSP based data processing platform is employed in the proposed system. Today's DSP technologies provide not only powerful and versatile signal processing capability, but also low volume and low power consumption.

The proposed system solution is implemented in a board level design. The experimental results with real chemical samples have proved the feasibility and effectiveness of the solution.

Future Work

During the design and testing phases of this work, some design deficiencies and issues were discovered. Meanwhile, there are still many aspects of the system can be optimized to improve the integration and to reduce the cost and power consumption even further. All of these findings and thoughts are listed as below.

1) The noise factor of the LNA needs to be evaluated with a certain testing method. As the NQR frequency is from $500kHz$ to $6MHz$, the normal noise factor evaluation methods for typical RF systems do not work for this low frequency range. Therefore, an advanced test method needs to be designed for accurately testing the noise performance of the LNA.

2) The weight-updating circuit of the analog adaptive filter has a design issue. The bias generation circuit for the weight-updating circuit is turned off during the DC offset

cancelling phase. As a result, the DC offset cancellation circuit could not work, which leads to the malfunction of the weight-updating circuit.

3) The PIN diode RF switch requires a very high reverse-biased voltage to provide high isolation in off-state. Although it does not consume currents in off-state as the PIN diode is reversely biased, this high voltage may sabotage hardware reliability. Moreover, it consumes relatively high power in its on-state, which is not preferable for portable systems. Therefore, despite of its compact size, a better alternative RF switch is desired to replace the PIN diode based RF switch.

4) As of now, the NQR probe in this system is being manually tuned. That is to monitor the on-going amplitude of the oscillation inside the NQR probe and to adjust the value of the resonant capacitor so that the maximum amplitude can be reached. In other words, it is indicating that the NQR probe is tuned to a resonant network when the maximum amplitude is reached. If an automatic tuning circuit is designed for the NQR probe, the efforts for manually and iteratively tuning can be greatly reduced. Also, the resonant network tuning will be executed more accurately.

5) To further reduce the cost, size and power consumption of the system, the integration of the receiver chain needs to be further improved. Specifically, the ADC can be integrated on the customized IC.

6) The prototype system is designed based on the assumption that the power management network is available. It is supported by external DC power supplies. For real portable systems, as they are normally battery-powered, a high efficiency power management circuit is required. Developing power management circuits is another important research area that needs to be explored.

Bibliography

[1] Human Rights Watch, *Landmine Monitor Report 2003: Toward a Mine-free World*, Human Rights Watch, 2003.

[2] M. Marshall and J. C. Oxley, *Aspects of Explosives Detection*, Elsevier, 2011.

[3] K. Langer, "A guide to sensor design for land mine detection," *Proceedings of EUREL International Conference on the Detection of Abandoned Land Mines: A Humanitarian Imperative Seeking a Technical Solution*, pp. 30–32, 1996.

[4] National Research Council, *Existing and Potential Standoff Explosives Detection Techniques*, National Academies Press, 2004.

[5] L. V. Haley and J. M. Romeskie, "Development of an explosives detection system using fast gc-ims technology," *Proceedings of International Carnahan Conference on Security Technology*, pp. 59–64, 1998.

[6] A. Staubs and M. Matyjaszczyk, "Novel trace chemical detection technologies for homeland security," *Proceedings of IEEE Conference on Technologies for Homeland Security*, pp. 199–204, 2008.

[7] C. Dass, *Fundamentals of Contemporary Mass Spectrometry*, Wiley-Interscience, 2007.

[8] S.-H. Lee, D. Stubbs, W. Hunt, and P. Edmonson, "Vapor phase detection of plastic explosives using a saw resonator immunosensor array," *Proceedings of IEEE Sensors 2005*, pp. 468–471, 2005.

[9] G. Watson and E. Staples, "SAW resonators as vapor sensors," *Proceedings of Ultrasonics Symposium*, vol. 1, pp. 311–314, 1990.

[10] A. T. Nimala, U. Mittala, M. Singha, M. Khanejaa, G. K. Kannanb, J. C. Kapoorb, V. Dubeyc, P. K. Gutchc, G. Lalc, K. D. Vyasc and D. C. Guptac, "Development of handheld saw vapor sensors for explosives and cw agents," *Sensors and Actuators B: Chemical*, vol. 135, pp. 399–410, 2009.

[11] J. Reboun, A. Hamacek, T. Dzugan, and M. Kroupa, "Sensorial characteristics of conductive polymers," *International Spring Seminar on Electronics Technology*, pp. 1–5, 2009.

[12] J. A. Covington, S. L. Tan, J. W. Gardner, A. Hamilton, T. Koickal, and T. Pearce, "Combined smart chemfet/resistive sensor array," *Proceedings of IEEE Sensors 2003*, vol. 2, pp. 1120–1123, 2003.

[13] D. Rairigh, A. Mason, P. Rowe, and E.T. Zellers, "Baseline resistance cancellation circuit for high resolution thiolate-monolayer-protected gold nanoparticle vapor sensor arrays," *Proceedings of IEEE International Symposium on Circuits and Systems*, pp. 2002–2005, 2008.

[14] C. Lintao, A. Kovalev and T. S. Mayer, "Conducting polymer nanofibers for gas sensor," *Proceedings of International Conference on Information Technology and Applications in Biomedicine*, pp. 196–198, 2008.

[15] E. Bentes, H.L.Gomes, P. Stallinga, and L. Moura, "Detection of explosive vapors using organic thin-film transistors," *Proceedings of IEEE Sensors 2004*, vol. 2, pp. 766–769, 2004.

[16] R. S. Dudhe, S. P. Tiwari, H. N. Raval, M. A. Khaderbad, R. Singh, J. Sinha, M. Yedukondalu, M. Ravikanth, A. Kumar, and V. R. Rao, "Explosive vapor sensor using poly (3-hexylthiophene) and Cu^{II} tetraphenylporphyrin composite based organic field effect transistors," *APPLIED PHYSICS LETTERS*, vol. 93, 263306, 2008.

[17] R. S. Dudhe, V. Seena, S. Mukherji, A. Kumar and R. Rao, "Organic sensors for explosive detection," *Proceedings of International Conference on Computers and Devices for Communication*, pp. 1–6, 2009.

[18] N. E. Jacobsen, *NMR Spectroscopy Explained: Simplified Theory, Applications and Examples for Organic Chemistry and Structural Biology*, John Wiley & Sons, 2007.

[19] J.-S. Yang and T. M. Swager, "Fluorescent porous polymer films as tnt chemosensors: Electronic and structural effects," *Journal of the American Chemical Society*, vol. 120, no. 46, pp. 11864–11873, 1998.

[20] Q. Zhou and T. M. Swager, "Fluorescent chemosensors based on energy migration in conjugated polymers: The molecular wire approach to increased sensitivity," *Journal of the American Chemical Society*, vol. 117, no.50, pp. 12593–12602, 1995.

[21] G. V. Zyryanov, M. A. Palacios, and P. Anzenbacher, "Simple molecule-based fluorescent sensors for vapor detection of TNT," *ORGANIC LETTERS*, vol. 10, no. 17, pp. 3681–3684, 2008.

[22] C. J. Cumming, C. Aker, M. Fisher, M. Fox, M. J. la Grone, D. Reust, M. G.Rockley, T. M. Swager, E. Towers, and V. Williams, "Using novel fluorescent polymers as sensory

materials for above-ground sensing of chemical signature compounds emanating from buried landmines," *IEEE Transactions on Geoscience AND Remote Sensing*, vol. 39, no. 6, pp. 1119–1128, 2001.

[23] J. W. Gardner and J. Yinon, *Electronic Noses and Sensors for the Detection of Explosives*, Kluwer Academic Publishers, 2004.

[24] R. Hashemi, W. Bradley and C. Lisanti, *MRI: The Basics*, Lippincott Williams & Wilkins, 2010.

[25] J. A. S. Smith, "Nuclear quadrupole resonance spectroscopy. General principles," *Journal of Chemical Education*, vol. 48, no. 1, pp. 39–49, 1971.

[26] A. N. Garroway, M. L. Buess, J. B. Miller, B. H. Suits, A. D. Hibbs, G. A. Barrall, R. Matthews and L. J. Burnett, "Remote sensing by nuclear quadrupole resonance," *IEEE Transactions on Geoscience AND Remote Sensing*, vol. 39, no. 6, pp. 1108–1118, 2001.

[27] L. Theisen, D. W. Hannum, D. W. Murray, and J. E. Parmeter, *Survey of Commercially Available Explosives Detection Technologies and Equipment 2004*, the National Law Enforcement and Correction Technology Center, a Program of the National Institute of Justice, U.S. Department of Justice, 2004.

[28] J. E. Parmeter, "The challenge of standoff explosives detection," *Proceedings of International Carnahan Conference on Security Technology*, pp. 355–358, 2004.

[29] H. G. Dehmelt and H. Kruger, "Pure quadrupole resonance in solids," *Naturwissenschaften*, vol. 37, pp. 111, 1950.

[30] R. V. Pound, "Nuclear electric quadrupole interactions in crystals," *Physical Review*, vol. 79, pp. 685–702, 1950.

[31] W. L. Rollwitz, J.D. King, and G. A. Matzkanin, "Fundamentals of nuclear magnetic resonance for the detection and identification of explosives," *Proceedings of New Concepts Symposium and Workshop on Detection and Identification of Explosives*, 1978.

[32] A. G. Landers, T. B. Brill, and R. A. Marino, "Electronic effects and molecular motion in .beta.-octahydro-1,3,5,7-tetranitro-1,3,5,7-tetrazocine based on nitrogen-14 nuclear quadrupole resonance spectroscopy," *The Journal of Physical Chemistry*, vol. 85, no. 18, pp. 2618–2623, 1981.

[33] J. A. S. Smith, "Nitrogen-14 Quadrupole Resonance Detection of RDX and HMX Based Explosives," *Proceedings of European Convention on Security and Detection*, pp. 288–292, 1995.

[34] M. D. Rowe and J. A. S. Smith, "Mine detection by nuclear quadrupole resonance," *Proceedings of UREL International Conference on the Detection of Abandoned Land Mines: A Humanitarian Imperative Seeking a Technical Solution*, pp. 62–66, 1996.

[35] J. A. S. Smith and N. F. Peirson, "Method of and apparatus for nuclear quadrupole resonance testing a sample," U.S. Patent 6566873 B1, 2003.

[36] V. S. Grechishkin, "NQR device for detecting plastic explosives, mines, and drugs," *Applied Physics A*, vol. 55, no. 6, pp. 505–507, 1992.

[37] T. N. Rudakov, T. J. Rayner, P. A. Hayes and K. L. Russeth, "Detection of Explosives by Quadrupole Resonance method: new aspects for security," *Detection and Disposal of Improvised Explosives*, NATO Security through Science Series, pp. 191–204, 2006.

[38] J. B. Miller, "Nuclear quadrupole resonance detection of explosives: an overview," *Proceedings of SPIE 8017*, Detection and Sensing of Mines, Explosive Objects, and Obscured Targets XVI, 801715, 2011.

[39] B. H. Suits, A. N. Garroway, and J. B. Miller, "Noise-immune coil for unshielded magnetic resonance measurements," *Journal of Magnetic Resonance*, vol. 131, no. 1, pp. 154–158, 1998.

[40] B. H. Suits, A. N. Garroway, and J. B. Miller, "Surface and gradiometer coils near a conducting body: the lift-off effect," *Journal of Magnetic Resonance*, vol. 135, no. 2, pp. 373–379, 1998.

[41] B. H. Suits, A. N. Garroway, "Optimizing surface coils and the self-shielded gradiometer," *Journal of Applied Physics*, vol. 94, no. 6, pp. 4170-4178, 2003.

[42] B. H. Suits, "The noise immunity of gradiometer coils for ^{14}N NQR land mine detection: practical limitations," *Applied Magnetic Resonance*, vol. 25, no. 3–4, pp. 371–382, 2004.

[43] A. D. Hibbs, G. A. Barrall, P. V. Czipott, A. J. Drew, D. M. Gregory, D. K. Lathrop, Y. K. Lee, E. E. Magnuson, R. Matthews, D. C. Skvoretz, S. A. Vierkotter and D. O. Walsh, "Detection of TNT and RDX landmines by stand-off nuclear quadrupole resonance," *Proceedings of SPIE 3710*, Detection and Remediation Technologies for Mines and Minelike Targets IV, 454, 1999.

[44] A. N. Garroway, M. L. Buess, J. B. Miller, K. J. McGrath, J. P. Yesinowski, B. H. Suits and G. R. Miller, "Explosives detection by nuclear quadrupole resonance (NQR)," *Proceedings of 6th International Symposium on the Analysis and Detection of Explosives*, ch. 19, 1998.

[45] J. B. Miller, B. H. Suits, A. N. Garroway and M. A. Hepp, "Interplay among recovery time, signal, and noise: Series- and parallel-tuned circuits are not always the same," *Concepts in Magnetic Resonance*, vol. 12, no. 3, pp. 125–136, 2000.

[46] J. B. Miller, K. L. Sauer, C. A. Klug and M. L. Buess, "Efficient excitation and ringing suppression in nuclear quadrupole resonance," *Explosives Detection Using Magnetic and Nuclear Resonance Techniques*, NATO Science for Peace and Security Series B: Physics and Biophysics, pp. 57–71, 2009.

[47] J. L. Schiano, T. Routhier, A. J. Blauch and M. D. Ginsberg, "Feedback optimization of pulse width in the SORC sequence," *Journal of Magnetic Resonance*, vol. 140, no. 1, pp. 84–90, 1999.

[48] A. J. Blauch, J. L. Schiano, L. Jeffrey and M. D. Ginsberg, "Landmine detection using feedback NQR," *Proceedings of SPIE 3710*, Detection and Remediation Technologies for Mines and Minelike Targets IV, pp. 464–473, 1999.

[49] R. M. Deas, I. A. Burch and D. M. Port, "Detection of RDX and TNT mine-like targets by nuclear quadrupole resonance," *Proceedings of SPIE 4742*, Detection and Remediation Technologies for Mines and Minelike Targets VII, pp. 482–489, 2002.

[50] H. Itozaki, G. Ota, M. Tachiki and D. He, "Development of NQR explosive detector in Japan," *Proceedings of SPIE 6553*, Detection and Remediation Technologies for Mines and Minelike Targets XII, 2007.

[51] H. Itozaki and G. Ota, "Nuclear Quadrupole Resonance for Explosive Detection," *International Journal on Smart Sensing and Intelligent Systems*, vol. 1, no. 3, pp. 705–715, 2008.

[52] D. F. He, M. Tachiki, H. Itozaki, "Detecting the ^{14}N NQR Signal Using a High-Tc SQUID," *IEEE Transactions on Applied Superconductivity*, vol. 17, no. 2, pp. 843–845, 2007.

[53] G. Ota and H. Itozaki, "Nuclear quadrupole resonance echoes from hexamethylenetetramine," *Solid State Nuclear Magnetic Resonance*, vol. 30, no. 3–4, pp. 135–140, 2006.

[54] T. N. Rudakov, V. T. Mikhaltsevitch and J. H. Flexman, "Spin-echoes in nitrogen-14 quadrupolar spin-systemwith axially symmetric electric field gradient tensor," *Solid State Nuclear Magnetic Resonance*, vol. 25, no. 1–3, pp. 112-118, 2004.

[55] S. Tantum, L. Collins, L. Carin, I. Gorodnitsky, A. D. Hibbs, D. O. Walsh, G. A. Barrall, D. M. Gregory, R. Matthews and S. A. Vierkotter, "Signal processing for NQR discrimination of buried landmines," *Proceedings of SPIE 3710*, Detection and Remediation Technologies for Mines and Minelike Targets IV, pp. 474–482, 1999.

[56] Y. Tan, S.L. Tantum and L. M. Collins, "Landmine detection with nuclear quadrupole resonance," *Proceedings of IEEE International Geoscience and Remote Sensing Symposium*, vol. 3, pp. 1575–1578, 2002.

[57] Y. Tan, S.L. Tantum and L. M. Collins, "Kalman filtering for enhanced landmine detection using quadrupole resonance," *IEEE Transactions on Geoscience and Remote Sensing*, vol.43, no.7, pp. 1507–1516, 2005.

[58] Y. Tan, S.L. Tantum and L. M. Collins, "Cramer-Rao lower bound for estimating quadrupole resonance signals in non-Gaussian noise," *IEEE Signal Processing Letters*, vol. 11, no. 5, pp. 490–493, 2004.

[59] Y. Jiang, P. Stoica, J. Li, "Array signal Processing in the known waveform and steering vector case," *Signal Processing, IEEE Transactions on*, vol. 52, no. 1, pp. 23–35, 2004.

[60] G. Liu, Y. Jiang, H. Xiong, J. Li, and G. A. Barrall, "Radio frequency interference suppression for landmine detection by quadrupole resonance," *EURASIP Journal on Applied Signal Processing*, vol. 2006, pp. 1–14, 2006.

[61] H. Xiong, J. Li and G. A. Barrall, "Joint TNT and RDX detection via quadrupole resonance," *IEEE Transactions on Aerospace and Electronic Systems*, vol. 43, no. 4, pp. 1282–1293, 2007.

[62] A. Jakobsson, M. Mossberg, M. Rowe and J. A. S. Smith, "Exploiting temperature dependency in the detection of NQR signals," *IEEE Transactions on Signal Processing*, vol. 54, no. 5, pp. 1610–1616, 2006.

[63] S. D. Somasundaram, A. Jakobsson, J. A. S. Smith, and K. Althoefer, "Exploiting spin echo decay in the detection of nuclear quadrupole resonance signals," *IEEE Transactions on Geoscience and Remote Sensing*, vol. 45, no. 4, pp. 925–933, 2007.

[64] S. D. Somasundaram, A. Jakobsson, M. D. Rowe, J. A. S. Smith, N. R. Butt, and K. Althoefer, "Robust detection of stochastic nuclear quadrupole resonance signals," *IEEE Transactions on Signal Processing*, vol. 56, no. 9, pp. 4221–4229, 2008.

[65] N. R. Butt, A. Jakobsson, S. D. Somasundaram, and J. A. S. Smith, "Robust multichannel detection of mixtures using nuclear quadrupole resonance," *IEEE Transactions on Signal Processing*, vol. 56, no. 10, pp. 5042–5050, 2008.

[66] S. D. Somasundaram, A. Jakobsson, and E. Gudmundson, "Robust nuclear quadrupole resonance signal detection allowing for amplitude uncertainties," *IEEE Transactions on Signal Processing*, vol. 56, no. 3, pp. 887–894, 2008.

[67] S. D. Somasundaram, A. Jakobsson and N. R. Butt, "Countering radio frequency interference in single-sensor quadrupole resonance," *IEEE Geoscience and Remote Sensing Letters*, vol. 6, no. 1, pp.62–66, 2009.

[68] F. Bloch, W. W. Hansen and M. Packard, "Nuclear induction," *Physical Review*, vol. 69, pp. 127, 1946.

[69] D. R. Vij, *Handbook of Applied Solid State Spectroscopy*, Springer, 2010.

[70] M. Levitt, *Spin Dynamics, Basics of Nuclear Magnetic Resonance*, 1st ed., Wiley, 2001.

[71] J. Yinon, *Counterterrorist Detection Techniques of Explosives*, Elsevier Science, pp. 157–198, 2011.

[72] M. Ostafin and B. Nogaj, "^{14}N-NQR based device for detection of explosives in landmines," *Measurement*, vol. 40, no. 1, pp. 43–54, 2007.

[73] X. Li and X. Zhang, "Investigation of concealed explosive detection by 14^N-NQR," *Proceedings of an IAEA Technical Meeting on Combined Devices for Humanitarian Demining and Explosives Detection*, 2006.

[74] R. A. Marino, R. F. Connors and L. Leonard, *Nitrogen-14 NQR study of energetic materials, Final Report*, Block Engineering, Inc., 1982.

[75] J. B. Miller and G. A. Barrall, "Explosives detection with nuclear quadrupole resonance," *American Scientist*, vol. 93, no. 1, pp. 50, 2005.

[76] Wikipedia, *Spin echo*, `http://en.wikipedia.org/wiki/Spin_echo`.

[77] E. L. Hahn, "Spin Echoes," *Physical Review*, vol. 80, pp. 580–594, 1950.

[78] D. B. Laubacher, *Superconducting planar coil in a low power nuclear quadrupole resonance detection system*, US Patent Application Publication, NO. US20040245988-A1, 2004.

[79] C. Wilker, J. D. McCambridge, D. B. Laubacher, R. L. Alvarez, J. S. Guo, C. F. Carter, M. A. Pusateri and J. L. Schiano, "HTS sensors for NQR spectroscopy," *IEEE MTT-S International Microwave Symposium Digest*, vol. 1, pp. 143–146, 2004.

[80] M. Augustinea, D. TonThatb and J. Clarkeb, "SQUID detected NMR and NQR," *Solid State Nuclear Magnetic Resonance*, vol. 11, no. 1–2, pp. 139–156, 1998.

[81] T. N. Rudakov, A. V. Belyakov and V. T. Mikhaltsevich, "A low-frequency instrument for remote nuclear quadrupole resonance experiments," *Measurement Science and Technology*, vol. 8, no. 4, pp. 444–448, 1997.

[82] N. Sun, Y. Liu, H. Lee, R. Weissleder and D. Ham, "CMOS RF biosensor utilizing nuclear magnetic resonance," *IEEE Journal of Solid-State Circuits*, vol. 44, no. 5, pp. 1629–1643, 2009.

[83] X. Zhang, N. Schemm and S. Balkir, "A novel power amplification scheme for nuclear magnetic resonance/nuclear quadrupole resonance systems," *Review of Scientific Instruments*, vol. 82, no. 3, 034707, 2011.

[84] X. Tang, X. Hu, Z. Dai, T. Zhang and W. Liu, "RF power amplifier of NMR system," *Proceedings of International Conference on Bioinformatics and Biomedical Engineering*, pp. 1–4, 2009.

[85] J. Jin, *Electromagnetic Analysis and Design in Magnetic Resonance Image*, 1st ed. CRC Press, 1998.

[86] A. Grebennikov, *RF and Microwave Power Amplifier Design*, McGraw-Hill Professional, 2004.

[87] A. Grebennikov and N. Sokal, *Switchmode RF Power Amplifiers*, Newnes, 2007.

[88] E. Gaalaas, "Class D Audio Amplifiers: What, Why, and How," *Analog Dialogue*, vol. 40, no. 6, pp. 1–7, 2006, available at `http://www.analog.com/analogdialogue`.

[89] M. Kazimierczuk, "Class D voltage-switching MOSFET power amplifier," *IEE Proceedings B of Electric Power Applications*, vol. 138, pp. 285–296, 1991.

[90] I. Bahl, *Fundamentals of RF and Microwave Transistor Amplifiers*, Wiley, 2009.

[91] T. H. Lee, *The Design of CMOS Radio-Frequency Integrated Circuits*, Cambridge University Press, 2004.

[92] L. Maloratsky, *Passive Rf & Microwave Integrated Circuits*, Elsevier/Newnes, 2004.

[93] J. B. Johnson, "Thermal agitation of electricity in conductors," *Physics Reviews*, vol. 32, pp. 97–109, 1928.

[94] H. Nyquist, "Thermal agitation of electric charge in conductors," *Physics Reviews*, vol. 32, pp. 110–113, 1928.

[95] D. Johns and K. Martin, *Analog Integrated Circuit Design*, John Wiley & Sons, 1997.

[96] A. Masaoka, D. Sumino and Y. Omura, "Theory of carrier-density-fluctuation-induced transport noise in metal-oxide-semiconductor field-effect transistors," *Journal of Applied Physics*, vol. 93, no. 9, pp.5359–5368, 2003.

[97] R. J. Baker, *CMOS Circuit Design, Layout, and Simulation*, Wiley, 2011.

[98] F. Bruccoleri, E. A. M. Klumperink and B. Nauta, "Wide-band CMOS low-noise amplifier exploiting thermal noise canceling," *IEEE Journal of Solid-State Circuits*, vol. 39, NO. 2, pp. 275–282, 2004.

[99] National Telecommunications and Information Administration, United States Department of Commerce, *United States Frequency Allocation Chart*, available at `http://www.ntia.doc.gov/page/2011/united-states-frequency-allocation-chart`.

[100] D. Hernandez-Garduno, and J. Silva-Martinez, "A CMOS 1 Gb/s 5-tap fractionally-spaced equalizer," *IEEE Journal of Solid-State Circuits*, vol. 43, no. 11, pp. 2482–2491, 2008.

[101] B. Widrow, J. R. Glover, J. M. McCool, J. Kaunitz, C. S. Williams, R. H. Hearn, J. R. Zeidler, E. Dong and R. C. Goodlin, "Adaptive noise cancelling: principles and applications," *Proceedings of the IEEE*, vol. 63, no. 12, pp. 1692–1716, 1975.

[102] B. Farhang-Boroujeny, *Adaptive Filters Theory and Applications*, John Wiley & Sons, 1998.

[103] D. Neumann, M. W. Hoffman and S. Balkir, "Robust front-end design for ultra wide-band systems," *Proceedings of IEEE International Symposium on Circuits and Systems*, 2006.

[104] A. Carusone and D. A. Johns, "Analogue adaptive filters: past and present," *IEEE Proceedings - Circuits, Devices and Systems*, vol. 147, No. 1, pp. 82–90, 2000.

[105] L. Ortiz-Balbuena, A. Martinez-Gonzalez, H. Perez-Meana, L. Nino de Rivera and J. Ramirez-Angulo, "A continuous-time adaptive filter structure," *Proceedings of International Conference on Acoustics, Speech, and Signal Processing*, vol. 2, pp. 1061–1064, 1995.

[106] D. A. Johns, W. M. Snelgrove and A. S. Sedra, "Continuous-time LMS adaptive recursive filters," *IEEE Transactions on Circuits and Systems*, vol. 38, no. 7, pp. 769–777, 1991.

[107] F. J. Kub and E. W. Justh, "Analog CMOS implementation of high frequency least-mean square error learning circuit," *IEEE Journal of Soild-State Circuits*, vol. 30, No. 12, pp. 1391–1398, 1995.

[108] S. Karni and G. Zeng, "The analysis of the continuous-time LMS algorithm," *IEEE Transactions on Acoustics, Speech and Signal Processing*, vol. 37, no. 4, pp. 595–597, 1989.

[109] G. Han and E. Sanchez-Sinencio, "CMOS transconductance multipliers: a tutorial," *IEEE Transactions on Circuits and SystemsII*, vol. 45, no. 12, pp. 1550–1563, 1998.

[110] M. Ibrahim, S. Minaei and H. Kuntman, "DVCC based differential-mode all-pass and notch filters with high CMRR," *International Journal of Electronics*, vol. 93, no. 4, pp. 231–240, 2006.

[111] Texas Instruments Incorporated, *TMS320C6748 Fixed/Floating-Point DSP*, available at: `http://www.ti.com/lit/ds/symlink/tms320c6748.pdf`.

[112] Analog Devices Incorporated, *Interfacing to DSPs*, available at: `http://www.analog.com/static/imported-files/seminars_webcasts/MixedSignal_Sect8.pdf`.

[113] K. K. Parhi, *VLSI Digital Signal Processing Systems: Design and Implementation*, John Wiley, 1999.

[114] Texas Instruments Incorporated, *C6748/46/42 Power Consumption Summary*, available at `http://processors.wiki.ti.com/index.php/C6748/46/42_Power_Consumption_Summary`.

[115] N. Schemm, S. Balkir and M.W. Hoffman, "A $4-\mu$W CMOS front end for particle detection applications," *IEEE Transactions on Circuits and Systems II: Express Briefs*, vol. 57, no. 2, pp. 100–104, 2010.

[116] Logic PD Incorporated, *Zoom OMAP-L138 EVM Development Kit Product Brief*, available at: `http://support.logicpd.com/downloads/1210/`.

[117] X. Huang, G. Xu and F. Hao, "$^{1}4N$ NQR study of Urea and Thiourea," *Advanced Marerials Research*, vol. 774–776, pp. 757–762, 2013.

[118] A.F. Privalov, D. Kruk, A. Gadke, H. Stork and F. Fujara, "Nuclear quadrupole resonance (NQR) enhancement by polarization transfer and its limitation due to relaxation," *Journal of Physics D: Applied Physics*, vol. 40, no. 23, pp. 7555–7559, 2007.